LIÈGE université Library

https://lib.uliege.be https://matheo.uliege.be

Master Thesis : Photocatalytic coatings for water purification from antibiotic contaminants (including an introduction to research methodology)

Auteur : Do Minh Khoi,
Promoteur(s) : Heinrichs, Benoît
Faculté : Faculté des Sciences appliquées
Diplôme : Master : ingénieur civil en chimie et science des matériaux, à finalité spécialisée en Advanced Materials - Innovative Recycling
Année académique : 2025-2026
URI/URL : http://hdl.handle.net/2268.2/26162

Avertissement à l'attention des usagers :

Tous les documents placés en accès ouvert sur le site le site MatheO sont protégés par le droit d'auteur. Conformément aux principes énoncés par la "Budapest Open Access Initiative"(BOAI, 2002), l'utilisateur du site peut lire, télécharger, copier, transmettre, imprimer, chercher ou faire un lien vers le texte intégral de ces documents, les disséquer pour les indexer, s'en servir de données pour un logiciel, ou s'en servir à toute autre fin légale (ou prévue par la réglementation relative au droit d'auteur). Toute utilisation du document à des fins commerciales est strictement interdite.

Par ailleurs, l'utilisateur s'engage à respecter les droits moraux de l'auteur, principalement le droit à l'intégrité de l'oeuvre et le droit de paternité et ce dans toute utilisation que l'utilisateur entreprend. Ainsi, à titre d'exemple, lorsqu'il reproduira un document par extrait ou dans son intégralité, l'utilisateur citera de manière complète les sources telles que mentionnées ci-dessus. Toute utilisation non explicitement autorisée ci-avant (telle que par exemple, la modification du document ou son résumé) nécessite l'autorisation préalable et expresse des auteurs ou de leurs ayants droit.

UNIVERSITY OF LIÈGE
FACULTY OF APPLIED SCIENCE

Photocatalytic Coatings for Water Purification from Antibiotics Contaminants

Written by

Minh Khoi Do

Thesis presented to obtain the degree of:

Master of Science in Chemical and Materials Science Engineering, professional focus in Advanced Materials-Innovative Recycling

Thesis supervisor:

HEINRICHS Benoît

Academic year: **2025-2026**

Acknowledgements

I would like to express my deepest gratitude to my supervisor, **Professor Benoit Heinrich**, for accepting me into his research group and giving me the opportunity to work on photocatalytic coatings for water treatment, a field in which I initially had limited experience. I sincerely appreciate his trust, guidance, and continuous support throughout this work. He always dedicated time to discuss experimental challenges with me, helped me troubleshoot problems, and encouraged me to independently explore and test different approaches, which greatly contributed to both the success of this thesis and my personal growth as a researcher.

I would also like to sincerely thank **Ms. Anh** and **Ms. Carla** for their constant support over the six months I spent in the laboratory. They patiently guided me through many aspects of the work, particularly in OTC degradation experiments, and taught me the importance of being meticulous and careful in every experimental step. I am especially grateful to Ms. Anh, who provided me with valuable hands-on training and insights, from setting up the UVC experimental system to operating the TOC analysis equipment. Her support and knowledge were instrumental in helping me develop strong experimental skills.

My sincere thanks also go to **Mr. Julien**, who provided essential support at the beginning of my work, particularly in the synthesis of the coatings. He introduced me to key laboratory techniques and equipment, such as dip coating and oven usage, and guided me in understanding the practical aspects of material preparation.

I would also like to thank **Mr. Pierre, Mr. Joachim, Mr. Antoine, Mr. Cyril, and Ms. Marie** for their help with sample measurements and experimental assistance throughout my research. In addition, I am grateful to **Mr. Jérémy** for managing chemical orders and providing clear guidance on laboratory procedures, which greatly facilitated the progress of my work.

Finally, I would like to extend my heartfelt thanks to all the people I have met and worked with during my master's thesis. Their presence, support, and encouragement contributed significantly to the completion of this work and made my research journey a truly valuable and memorable experience.

Summary

This thesis investigates the development of immobilized TiO_2 photocatalytic coatings for the degradation of oxytetracycline (OTC), a persistent antibiotic contaminant commonly detected in aquaculture wastewater in Vietnam. The study focuses on replacing suspended photocatalyst systems with fixed coatings to eliminate the need for post-treatment catalyst separation.

A comparative evaluation of five different photocatalytic coatings, including four sol-gel-based coatings and one colloidal synthesis-based coating using Evonik Aeroxide P25, was conducted. The P25-based colloidal coating was selected for further optimization due to its relatively stable adhesion, higher surface area, and operational feasibility. Key processing parameters, including substrate characteristics, dip-coating cycles, calcination temperature and duration, were systematically investigated. The obtained optimal coating was characterized using SEM-EDX, XRD, and a profilometer.

The optimized configuration was obtained at 18 dip-coating cycles with calcination at 400 °C for 4 hours, resulting in a coating layer with a thickness of approximately 650–800 nm and strong adhesion (4B-5B, ASTM D3359). Photocatalytic tests under UVC irradiation showed that while direct photolysis contributes significantly to OTC degradation, the presence of the TiO_2 coating is necessary for enhanced mineralization, as reflected by TOC removal.

Reusability experiments indicated that the coating maintained structural integrity over repeated cycles, although a gradual decline in activity was observed, likely due to surface fouling by intermediate products. Overall, the optimized TiO_2 coating achieved 92.53% OTC degradation and 53.1% TOC removal, demonstrating performance comparable to suspended P25 systems.

Contents

Acknowledgements i
Summary ii
Contents iii
List of Figures vi
List of Tables viii
Introduction 1
Objective 4
1 State of the art 5
1.1 Antibiotics 5
1.2 Photocatalytic coatings 8
1.3 Substrates 11
1.4 Materials Synthesis Methods 13
1.5 Coating Methods 16
1.6 Materials Characterization Methods 18
1.7 Photocatalytic Performance Evaluation Methods 20
2 Experimental Section 21
2.1 Comparative Study of Photocatalytic Coating Fabrication Methods and Their Degradation Performance 21
2.1.1 Materials and chemicals 21
2.1.2 Experiments of catalyst synthesis 21
2.1.3 Dip-coating 26
2.1.4 Drying and calcination 27
2.1.5 Direct measurement of coating mass 27
2.1.6 The degradation of OTC under UVC light with photocatalytic coating 28
2.1.7 The adhesion of TiO_2 coating on the substrate 28
2.1.8 Characterizations of sol-gel and colloid synthesis-based coatings 30
2.1.9 Evaluation of photocatalytic efficiency of sol-gel and colloid synthesis-based coatings 30
2.2 Process Optimization of Photocatalytic Coating for Enhanced OTC Degradation 31
2.2.1 Effects of TiO_2 powder types on the particle deposition in the solution before dip-coating process 31

2.2.2 Effect of substrate nature on colloidal coating loading....31
2.2.3 Coating layer number on steel substrate....32
2.2.4 Calcination temperature (coated stainless-steel samples)....32
2.2.5 Calcination time (coated stainless-steel samples)....33
2.3 Characterizations of the optimal coating....34
2.3.1 Coating mass....34
2.3.2 Coating thickness....34
2.3.3 Coating morphology....34
2.3.4 Coating crystallinity and phase composition....34
2.4 Leaching test of the optimal coating on stainless-steel substrate....34
2.5 Reusability test....34
2.6 Adsorption Test of P25 coating and powder....35
2.7 Comparison of the Photocatalytic Activity between P25 coating and powder....36
3 Results and Discussions....37
3.1 Results of Comparative Study of Photocatalytic Coating Fabrication Methods and Their Degradation Performance....37
3.1.1 Results of visual characteristics of single-cycle photocatalytic coatings....37
3.1.2 Results of direct measurement of coating mass....38
3.1.3 Characterizations by SEM....39
3.1.4 Characterizations by XRD....42
3.1.5 The result of the coating adherence on substrate....44
3.1.6 Results of OTC degradation with photocatalytic coatings by UV-vis and TOC methods....48
3.2 Results of the Optimization of Photocatalytic Coatings for Enhanced OTC Degradation....57
3.2.1 Result of the effect of TiO_2 powder types on the particle deposition....57
3.2.2 Results of the effect of substrate surface nature on colloidal coating loading....58
3.2.3 Results of the optimization of the number of coating layers....60
3.2.4 Results of calcination temperature optimization....64
3.2.5 Results of calcination time optimization....69
3.3 Results of Characterizations of Optimal Coating....72
3.3.1 Coating mass via a direct measurement....72
3.3.2 Coating thickness via a profilometer method....72
3.3.3 Characterization of optimal coating by SEM-EDX....73

3.3.4 Characterization of optimal coating by XRD patterns 75
3.4 Results of reusability test 76
3.5 Results of adsorption test of P25 coating and powder 78
3.6 Results of photocatalytic activity comparison of P25 coating and powder 78
4 Conclusions and Recommendations 83
4.1 Conclusions 83
4.2 Recommendations 84
References 86
5 Appendices 94
5.1 Procedure of tape test in lab 94
5.2 XRD pattern 94
5.3 Effects of substrate surface nature on sol-gel based coating mass 95
5.4 EDX Mapping 96

List of Figures

Figure 1. Antibiotic classes used for Vietnamese fish producers and shrimp producers [4] 6
Figure 2. Oxytetracycline powder.....7
Figure 3. Structure of oxytetracycline [25].....7
Figure 4. Three main crystalline polymorphs of TiO_2 [34] 9
Figure 5. Photocatalytic Mechanism [29], [39] 11
Figure 6. Composition of Stainless Steel [41] 12
Figure 7. Physical properties of stainless-steel [43] 12
Figure 8. Sol-gel synthesis [47] 14
Figure 9. Colloidal synthesis.....15
Figure 10. Dip-coating process [54] 17
Figure 11. Summary of 2 coating synthesis methods 22
Figure 12. TSA solution.....23
Figure 13. TSAP25 solution 23
Figure 14. TSAP25P solution 24
Figure 15. TSAP solution 24
Figure 16. Functionalized P25 25
Figure 17. P25 solution.....25
Figure 18. Dip-coating machine 27
Figure 19. UVC irradiation setup.....28
Figure 20. Elcometer 99 tape 29
Figure 21. Sample preparation (A) OTC, (B) OTC and P25 powder, (C) OTC and P25 coating.....36
Figure 22. Five synthesized coatings with a single cycle of dip-coating (A) TSA, (B) TSAP25, (C) TSAP25P, (D) TSAP, (E) P25.....37
Figure 23. SEM images of (A) Steel, (B) TSA coating, (C) TSAP25 coating, (D) TSAP25P coating, (E) TSAP coating, (F) P25 coating at 10 kx magnitude.....39
Figure 24. SEM images of (A) Steel, (B) TSA coating, (C) TSAP25 coating, (D) TSAP25P coating, (E) TSAP coating, (F) P25 coating at 100 kx magnitude.....41
Figure 25. XRD patterns of photocatalytic powder calcined at 500 °C in 1 hour (a) P25, (b) TSAP25P, (c) TSAP25, (d) TSAP, (e) TSA 42
Figure 26. Homogeneity of TSA coating surface 44
Figure 27. Tape test of TSA coating (A) before, (B) after 44
Figure 28. Homogeneity of TSAP25 coating surface 45
Figure 29. Tape test of TSAP25 coating (A) before, (B) after.....45
Figure 30. Homogeneity of TSAP25P coating surface 46
Figure 31. Tape test of TSAP25P coating (A) before, (B) after.....46
Figure 32. Homogeneity of TSAP coating surface 47
Figure 33. Tape test of TSAP coating (A) before, (B) after 47
Figure 34. Homogeneity of P25 coating surface 48
Figure 35. Tape test of P25 coating (A) before, (B) after 48
Figure 36. UV-vis spectra of OTC degradation with TSA coating 49

Figure 37. Calibration curve of OTC 49
Figure 38. UV-vis spectra of OTC degradation with TSAP25 coating 51
Figure 39. UV-vis spectra of OTC degradation with TSAP25P coating 52
Figure 40. UV-vis spectra of OTC degradation with TSAP coating 53
Figure 41. UV-vis spectra of OTC degradation with P25 coating 55
Figure 42. Sedimentation behaviour of different TiO_2 powders: left-P25, right-pure TiO_2 57
Figure 43. (A) Reference substrates: glass and aluminium, (B) Roughness level 58
Figure 44. OTC degradation under different coating layers (A) Catalyst and UVC efficiency, (B) Catalyst contribution 61
Figure 45. TOC degradation under different coating layers (A) Catalyst and UVC efficiency, (B) Catalyst contribution 62
Figure 46. Tape test of coating of (A) 6 layers, (B) 9 layers, (C) 12 layers, (D) 15 layers, (E) 18 layers and (F) 21 layers 63
Figure 47. Substrate colours with different calcination temperatures (A) 300 °C, (B) 400 °C, (C) 500 °C and (D) 600 °C 64
Figure 48. OTC degradation under different coating calcination temperature (A) Catalyst and UVC efficiency, (B) Catalyst contribution 65
Figure 49. TOC degradation under different coating calcination temperature (A) Catalyst and UVC efficiency, (B) Catalyst contribution 66
Figure 50. Tape test of coating under calcination temperature of (A) 300 °C, (B) 400 °C, (C) 500 °C and (D) 600 °C 67
Figure 51. OTC degradation under different coating calcination time (A) Catalyst and UVC efficiency, (B) Catalyst contribution 69
Figure 52. TOC degradation under different coating calcination time (A) Catalyst and UVC efficiency, (B) Catalyst contribution 70
Figure 53. Tape test of coating under calcination time of (A) 1h, (B) 2h, (C) 3h and (D) 4h 71
Figure 54. Optimal coating thickness on glass substrate 72
Figure 55. SEM images of (A) optimal coating at 300 kx magnitude, (B) particle size distribution 73
Figure 56. EDX spectrum of the optimal coating 74
Figure 57. XRD patterns of the optimal P25 (400 °C, 4h) and pristine P25 75
Figure 58. OTC degradation on reusability test 76
Figure 59. TOC degradation on reusability test 77
Figure 60. Adsorption test of P25 coating and powder 78
Figure 61. OTC degradation efficiency of P25 coating and powder 79
Figure 62. TOC degradation efficiency of P25 coating and powder 80
Figure 63. Kinetics of OTC degradation 80
Figure 64. Pseudo-first-order kinetics: P25 Coating 82
Figure 65. Pseudo-first-order kinetics: P25 Powder 82
Figure 66. Lab procedure of tape test 94
Figure 67. XRD patterns of P25 powder and functionalized P25 powder 94
Figure 68. EDX mapping of Ti and O elements 96

List of Tables

Table 1. Types of antibiotics used in Vietnam 5
Table 2. Total TiO_2 mass in solution before dip-coating.....26
Table 3. Dip-coating cycles of sol-gel and colloid coatings 26
Table 4. Adherence evaluation based on ASTM D3359 standard [65].....29
Table 5. Sample preparation for characterization methods.....30
Table 6. Sample preparation for photocatalytic efficiency analysis methods.....30
Table 7. Test of coating layers 32
Table 8. Test of calcination temperature 32
Table 9. Test of calcination time 33
Table 10. Procedure of reusability test.....35
Table 11. The mass of sol-gel based coating.....38
Table 12. The mass of colloid based coating 38
Table 13. OTC degradation efficiency in the TSA system 50
Table 14. TOC degradation efficiency in the TSA system.....50
Table 15. OTC degradation efficiency in the TSAP25 system 51
Table 16. TOC degradation efficiency in the TSAP25 system 51
Table 17. OTC degradation efficiency in the TSAP25P system 52
Table 18. TOC degradation efficiency in the TSAP25P system 53
Table 19. OTC degradation efficiency in the TSAP system 54
Table 20. TOC degradation efficiency in the TSAP system 54
Table 21. OTC degradation efficiency in the P25 system.....55
Table 22. TOC degradation efficiency in the P25 system.....55
Table 23. Summary of degradation efficiency and catalyst contribution 56
Table 24. Deposition of colloidal solution.....57
Table 25. The colloid based coating mass on Al substrate.....58
Table 26. The colloid based coating mass on glass substrate 58
Table 27. Degraded OTC concentration with different coating layers 60
Table 28. Degraded TOC concentration with different coating layers 61
Table 29. Summary of results of coating layer test.....63
Table 30. Degraded OTC concentration with different coating calcination temperatures.....64
Table 31. Degraded TOC concentration with different coating layers 66
Table 32. Summary of results of coating calcination temperature test 68
Table 33. Degraded OTC concentration with different coating calcination times.....69
Table 34. Degraded TOC concentration with different coating calcination times.....70
Table 35. Summary of results of coating calcination time test 71
Table 36. Optimal coating mass.....72
Table 37. OTC concentration in P25 coating and P25 powder system over time.....81
Table 38. Corresponding coefficients of determination (R^2) 81
Table 39. The sol-gel based coating mass on Al substrate.....95
Table 40. The sol-gel based coating mass on glass substrate.....95

Introduction

Aquaculture plays a central role in global food security and economic development, and Vietnam is among the world's leading producers and exporters of aquaculture products, particularly shrimp. The Mekong Delta region accounts for most of the Vietnam's shrimp production, contributing significantly to national export revenue [1]. However, the rapid intensification of shrimp farming over the past two decades has resulted in increasing environmental pressures, especially water contamination caused by high stocking densities, excessive feed input, and disease outbreaks. Intensive aquaculture systems generate large volumes of wastewater containing organic matter, nutrients, pathogens, and pharmaceutical residues [2]. Among these contaminants, antibiotics have emerged as one of the most critical environmental concerns [3].

Antibiotics are widely used in shrimp aquaculture in Vietnam for both therapeutic and prophylactic purposes to control bacterial diseases such as vibriosis [3]. Surveys conducted in Vietnamese aquaculture systems report antibiotic application in approximately 20–30% of shrimp farms, with compounds such as oxytetracycline, sulfamethoxazole, enrofloxacin, and ciprofloxacin frequently detected in water and sediment samples [4]. Large-scale monitoring studies in the Mekong Delta have shown that antibiotic residues are present in a high proportion of aquaculture water samples, often with multiple antibiotics co-existing. These findings indicate that aquaculture systems act as reservoirs of antibiotic contaminants, which can be released into surrounding canals and rivers through water exchange practices. Because shrimp farming frequently relies on open or semi-open water systems, untreated discharge contributes directly to environmental dissemination of antibiotic residues [5].

The presence of antibiotics in aquatic environments poses serious ecological and public health risks. Antibiotics are biologically active molecules designed to inhibit or kill bacteria; therefore, their release into natural waters can disrupt microbial communities and ecological balance [6]. More critically, chronic exposure to sub-lethal concentrations of antibiotics promotes the development and proliferation of antimicrobial resistance (AMR) [7], [8]. Aquaculture environments have been identified as hotspots for antibiotic resistance genes (ARGs), which can be transferred between bacteria through horizontal gene transfer mechanisms. The emergence of antimicrobial resistance is recognized globally as one of the most pressing public health challenges of the 21st century. Resistant pathogens originating in aquatic environments may enter the human food chain through seafood consumption or environmental exposure, reducing the effectiveness of clinical antibiotics [9]. Furthermore, antibiotic residues in shrimp products can lead to export rejections, threatening the economic stability of Vietnam's aquaculture sector [10].

Conventional water treatment methods applied in aquaculture, such as sedimentation, filtration, and biological treatment, are generally ineffective for removing dissolved antibiotic molecules due to their chemical stability and complex aromatic structures [11]. Many antibiotics are recalcitrant to biodegradation and may persist in aquatic environments for extended periods. Adsorption-based methods can temporarily remove antibiotics from water; however, they often

transfer contaminants from one phase to another without complete mineralization, requiring further regeneration or disposal steps [12]. These limitations highlight the need for advanced treatment technologies capable of degrading antibiotic molecules into harmless end products.

Advanced Oxidation Processes (AOPs) have gained considerable attention as effective methods for eliminating persistent organic pollutants, including antibiotics, from water systems. AOPs are characterized by the *in-situ* generation of highly reactive species such as hydroxyl radicals (•OH), superoxide radicals ($O_2^{\bullet -}$), and other reactive oxygen species (ROS), which possess high oxidation potentials and can non-selectively attack complex organic molecules [13]. Through oxidative reactions, antibiotics can be transformed into intermediate compounds and eventually mineralized into carbon dioxide, water, and inorganic ions. Various AOP techniques have been investigated for antibiotic degradation, including ozonation, Fenton and photo-Fenton reactions, electrochemical oxidation, UV/H_2O_2 systems, and heterogeneous photocatalysis [14]. Among these, photocatalysis has emerged as a particularly promising approach due to its potential use of solar energy, environmental compatibility, and relatively low chemical input requirements [14].

Photocatalysis involves the excitation of a semiconductor material under light irradiation, leading to the generation of electron–hole pairs. These charge carriers interact with water and dissolved oxygen to produce reactive oxygen species capable of degrading organic pollutants. Titanium dioxide (TiO_2), zinc oxide (ZnO), and other semiconductor materials have been extensively studied for antibiotic degradation, with reported removal efficiencies often exceeding 80–90% under optimized laboratory conditions [15]. Recent studies have demonstrated the successful degradation of antibiotics such as tetracycline, sulfamethoxazole, and ciprofloxacin using modified photocatalysts under UV or visible light irradiation [16]. The advantages of photocatalytic processes include strong oxidation capability, minimal sludge production, and the possibility of complete mineralization rather than mere phase transfer [16].

Despite promising laboratory results, the practical implementation of photocatalytic AOPs in Vietnam's aquaculture systems remains limited. Most shrimp farms rely on traditional water exchange methods rather than integrated treatment technologies. Advanced treatment systems are often considered costly, complex, or unsuitable for decentralized rural aquaculture operations. Additionally, many photocatalytic studies focus on suspended nanoparticle systems, which require post-treatment separation and recovery of catalysts, limiting their practical applicability. Catalyst aggregation, limited stability, and reduced reusability further hinder large-scale deployment. There is therefore a critical need to develop immobilized and durable photocatalytic systems that can operate continuously under realistic aquaculture conditions [17].

Photocatalytic coatings represent a promising technological advancement to address these limitations. By immobilizing photocatalytic materials onto solid substrates, coatings eliminate the need for catalyst recovery while maintaining degradation efficiency. Such systems can be integrated into water circulation channels, pond liners, reactor walls, or filtration units within shrimp farming infrastructure [18]. Immobilized photocatalysts also improve operational stability, enhance reusability, and reduce environmental risks associated with nanoparticle

release [19]. However, challenges remain regarding coating adhesion, light penetration efficiency, long-term stability in saline aquaculture water, and degradation performance under natural sunlight conditions [19]. These technical gaps are particularly relevant in Vietnam, where climatic conditions, water salinity, and farming practices differ significantly from controlled laboratory environments.

Within this context, the REMAOP project aims to develop sustainable and effective solutions for removing antibiotic contaminants from aquaculture water through advanced material innovation. The project focuses on bridging the gap between laboratory-scale photocatalytic research and practical implementation in shrimp farming systems. This thesis contributes to REMAOP by investigating the development, characterization, and performance evaluation of photocatalytic coatings for antibiotic degradation in water. Emphasis is placed on material properties, coating stability, and photocatalytic degradation efficiency under conditions relevant to aquaculture environments. By integrating materials science with environmental engineering, this work seeks to provide a scalable and practical solution for reducing antibiotic contamination in Vietnamese shrimp farming systems.

The remainder of this thesis is structured as follows. After this introductory chapter, a comprehensive literature review examines antibiotic contamination in aquaculture and current advanced oxidation technologies for water treatment. The subsequent chapter describes the materials, synthesis procedures, and characterization techniques used to fabricate and analyse the photocatalytic coatings. Experimental results and performance evaluations are then presented and discussed, including degradation efficiency, influencing parameters, and stability assessments. Finally, conclusions are drawn regarding the feasibility of photocatalytic coatings for aquaculture water purification, and recommendations for future research and large-scale implementation within the REMAOP framework are provided.

Objective

The main objective of this master's thesis is to develop a TiO_2-based photocatalytic coating for the treatment and degradation of oxytetracycline (OTC) used in shrimp pond wastewater.

To achieve this objective, the following specific targets are established:

1. **Comparison and selection of photocatalytic coatings:**

   To synthesize and evaluate TiO_2-based photocatalytic coatings prepared by different methods, namely sol-gel and colloidal synthesis, and to compare their photocatalytic performance, adhesion strength, and coating stability to identify the most suitable coating under the context of the REMAOP project.

2. **Optimization and characterization of the selected coating:**

   To optimize the composition and preparation parameters of the selected photocatalytic coating and comprehensively characterize its physicochemical properties, including morphology, crystal structure, surface characteristics, and adhesion behaviour, with the aim of enhancing its photocatalytic degradation efficiency toward OTC and its by-products.

3. **Performance evaluation of the optimized photocatalytic coating:**
   To evaluate the photocatalytic performance of the optimized TiO_2-based coating through the degradation of oxytetracycline (OTC), mineralization efficiency via total organic carbon (TOC) removal, coating stability through leaching analysis, and durability through reusability tests over multiple photocatalytic cycles. The results will be used to assess the coating's effectiveness, stability, and potential for practical wastewater treatment applications.

1 State of the art

This chapter will present the current state of the art related to the photocatalytic degradation of oxytetracycline (OTC), an emerging environmental pollutant of growing concern due to its persistence and contribution to antibiotic resistance. It reviews existing treatment approaches and highlights the development of photocatalytic materials, with a focus on coating systems that enable practical applications. Attention is given to commonly used photocatalysts, recent material modifications to enhance efficiency, and the performance of these systems under different conditions. The section also identifies existing limitations and research gaps, providing the basis for the present study.

1.1 Antibiotics

1.1.1 Overview of using antibiotics in Mekong Delta

Antibiotics are a broad class of pharmaceutical compounds that persist in aquatic systems because of their chemical stability and low biodegradability. Antibiotics commonly found in aquaculture water in Mekong Delta where the REMAOP was implemented, listed in the below Table 1:

Table 1. Types of antibiotics used in Vietnam

Locations	Type of Antibiotics	Year	References
Can Tho city & An Giang province	Enrofloxacin (Fluoroquinolone), Trimethoprim (Diaminopyrimidine), Sulfamethoxazole/Sulfadiazine (Sulfonamide), Florfenicol (Phenicol), Amoxi cillin/Ampicillin (Penicillin), and Doxycy cline/Oxytetracycline(Tetracycline)	2015	[20]
Soc Trang & Ben Tre provinces	Sulfamethazine/Sulfadiazine/Sulfamethoxazole (Sulfonamide), Trimethoprim (Diaminopyrimidine), Ciprofloxacin/Enrofloxacin (Fluoro quinolone)	2016	[21]
An Giang province	Trimethoprim (Potentiated sulphonamide), Amoxicillin (ß-lactam), Enrofloxacin (Fluoroquinolone), Doxycycline/Oxytetracycline (Tetracycline)	2017	[22]
Dong Thap province	Phenicol (11 %), following by Tetracycline (10 %) and Sulfonamide (7%)	2018	[4]

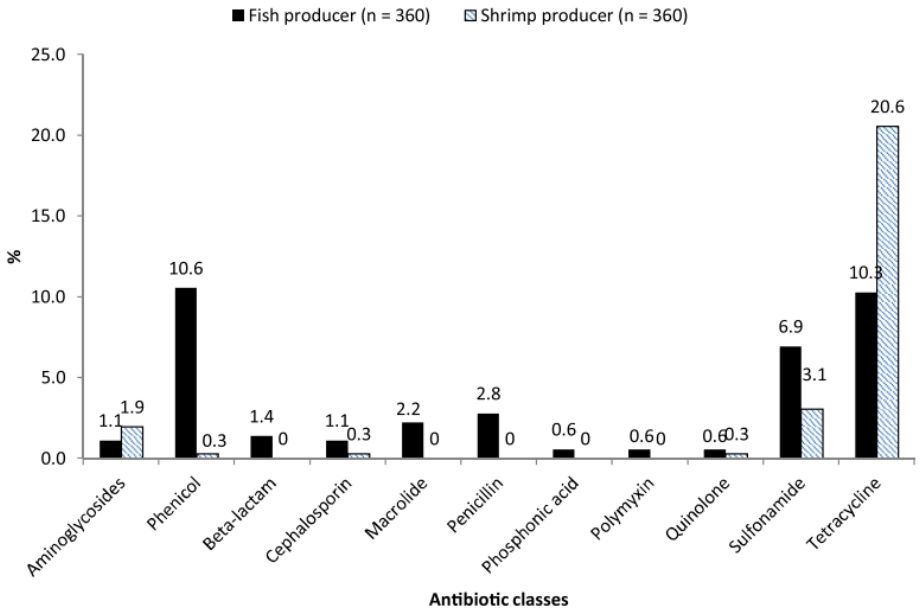

Figure 1. Antibiotic classes used for Vietnamese fish producers and shrimp producers [4]

Figure 1 shows the distribution of antibiotic classes used by Vietnamese fish and shrimp producers. Tetracyclines were the most frequently used antibiotics in both aquaculture sectors, with a particularly high usage among shrimp producers (20.6%) compared to fish producers (10.8%). Fish producers also reported notable use of phenicols (10.6%) and sulfonamides (6.9%), whereas the use of these antibiotic classes was lower among shrimp producers. The results indicate that tetracycline-based antibiotics, especially oxytetracycline, play a dominant role in disease management in Vietnamese aquaculture, highlighting their importance as well as the potential concerns regarding antibiotic residues and antimicrobial resistance in aquatic environments [4]. Based on the data from surveys of the REMAOP project in Vietnam, currently farmers used the concentration of oxytetracycline of about 30 mg/L for their aquaculture.

1.1.2 Properties of Oxytetracycline (OTC)

a) Physical Properties

OTC is typically encountered as a yellow crystalline solid with a molecular formula of $C_{22}H_{24}N_2O_9$ and a molecular weight of 460.43 g/mol. It exhibits high polarity due to the presence of multiple oxygen- and nitrogen-containing functional groups, resulting in significant solubility in water, particularly in its hydrochloride form (typically in the range of several hundred mg/L depending on pH). The compound shows amphoteric behaviours and exists in different ionic forms depending on the pH of the solution, with reported pKa values around 3.3, 7.3, and 9.1. These dissociation constants correspond to the deprotonation of phenolic diketone, tricarbonyl, and dimethylamino groups, respectively [23], [24].

Figure 2. Oxytetracycline powder

The solubility and speciation of OTC strongly influence its environmental mobility. Under acidic conditions, OTC is predominantly cationic, while at neutral pH it exists as a zwitterion, and under alkaline conditions it becomes anionic. This pH-dependent behaviour affects its interaction with surfaces, adsorption processes, and transport in aquatic environments. Furthermore, OTC exhibits relatively low volatility due to its low vapor pressure, meaning that it remains primarily in the aqueous phase rather than partitioning into the atmosphere [24],[25]

b) Chemical Properties

The chemical structure of OTC consists of a four-ring (tetracyclic) naphthacene core with various functional groups, including hydroxyl (–OH), carbonyl (C=O), amide (–CONH–), and dimethylamino ($–N(CH_3)_2$) groups. This structure is highly conjugated, providing resonance stabilization and contributing to its chemical persistence in the environment. The presence of these functional groups also enables strong intermolecular interactions such as hydrogen bonding, which enhances its solubility and affinity for aqueous systems [25].

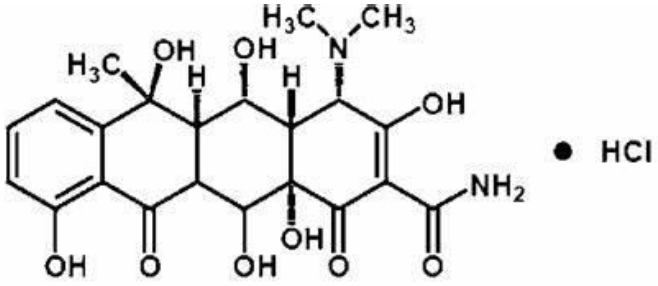

Figure 3. Structure of oxytetracycline [25]

One of the most significant chemical properties of OTC is its strong ability to chelate metal ions such as Ca^{2+}, Mg^{2+}, Fe^{3+}, and Al^{3+}. Chelation occurs through oxygen atoms in the diketone and phenolic groups, forming stable complexes that can alter its reactivity, reduce its bioavailability, and promote its accumulation in sediments. These complexes can also hinder degradation processes, further contributing to persistence [25].

OTC undergoes several transformation processes in aquatic environments, including photolysis, hydrolysis, and oxidation. However, these processes are often slow or incomplete. Photodegradation is influenced by light intensity and pH, while hydrolysis is generally limited under environmental conditions. Importantly, OTC degradation can lead to the formation of

intermediate compounds that may retain antimicrobial activity or exhibit increased toxicity [26]. Additionally, the compound's ability to absorb UV light due to its conjugated structure makes it responsive to photocatalytic degradation, which is the basis for advanced oxidation processes [26].

c) Biological Properties

Biologically, OTC functions by inhibiting bacterial protein synthesis through binding to the 30S ribosomal subunit, preventing the attachment of aminoacyl-tRNA and thus blocking peptide chain elongation. This mechanism gives OTC a broad-spectrum antibacterial activity, making it highly effective in aquaculture applications. However, this same property contributes significantly to environmental concerns when OTC residues are present in water bodies [27].

A key issue is that a large fraction (typically 60–80%) of administered OTC is excreted unmetabolized by aquatic organisms, leading to its direct release into the surrounding environment. Even at low concentrations, OTC can exert selective pressure on microbial communities, promoting the development and form of antibiotic-resistant bacteria and resistance genes. This is considered a major global health concern, as resistance genes can be transferred across species and potentially impact human health [27], [28]

In addition to antimicrobial resistance, OTC can affect non-target aquatic organisms. It has been shown to alter microbial community structures, inhibit beneficial bacteria involved in nutrient cycling, and impact algae and invertebrates. Chronic exposure may lead to ecological imbalances in aquatic systems. Furthermore, due to its ability to bind to biomolecules and accumulate in tissues, OTC can enter the food chain, posing potential risks to higher organisms [27], [28].

1.2 Photocatalytic coatings

1.2.1 Overview of photocatalysts

Photocatalytic coatings have emerged as an effective strategy for the degradation of persistent organic pollutants, including antibiotics such as oxytetracycline (OTC), in water systems. Among the widely investigated photocatalysts, semiconducting metal oxides such as TiO_2, ZnO, WO_3, and Fe_2O_3 have demonstrated strong oxidative capabilities under light irradiation. These materials operate based on the generation of electron–hole pairs when irradiated with energy equal to or greater than their band gap, leading to the formation of highly reactive species such as hydroxyl radicals (•OH) and superoxide radicals ($O_2^{\bullet -}$), which can mineralize organic contaminants [29]. Among these materials, titanium dioxide (TiO_2) remains the most extensively studied and applied photocatalyst due to its unique combination of properties, including high chemical stability, non-toxicity, low cost, and strong oxidative power while other materials show their drawbacks [30]. For instance, ZnO exhibits similar band gap energy and higher electron mobility but suffers from photo-corrosion and instability in aqueous systems. WO_3 can absorb visible light due to its narrower band gap; however, its conduction band position is not sufficiently negative to efficiently reduce oxygen, limiting ROS generation [31]. Fe_2O_3 offers visible-light activity and low cost but is hindered by short charge carrier

lifetimes and poor conductivity [32]. These limitations make TiO_2 a more robust and reliable choice for environmental photocatalysis despite its UV-light restriction.

1.2.2 Physical and Electronic Properties of TiO_2

Titanium dioxide is a wide band gap semiconductor that exists in three main crystalline polymorphs: anatase, rutile, and brookite. Anatase and rutile are the most studied phases, with anatase exhibiting a band gap of approximately 3.2 eV and rutile around 3.0 eV. The crystal structure of anatase is characterized by a tetragonal arrangement of TiO_6 octahedra, which promotes higher surface hydroxylation and lower electron–hole recombination compared to rutile. This structural feature is directly linked to its superior photocatalytic performance [33]

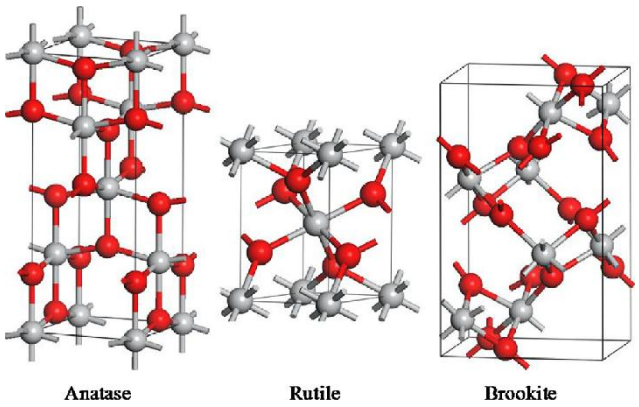

Figure 4. Three main crystalline polymorphs of TiO_2 [34]

From a physical perspective, TiO_2 exhibits high refractive index, strong UV absorption, and excellent chemical and thermal stability. It is chemically inert in aqueous environments and resistant to photo-corrosion. Additionally, TiO_2 is non-toxic and relatively inexpensive, making it highly suitable for environmental applications. The position of its valence band (VB ≈ +2.7 V vs NHE) provides strong oxidative power, sufficient to generate hydroxyl radicals from water or surface hydroxyl groups, while its conduction band (CB ≈ −0.5 V vs NHE) enables reduction of oxygen to superoxide radicals [33], [35]

1.2.3 Photocatalytic Activity of TiO_2

The photocatalytic activity of TiO_2 arises from its ability to absorb photons and generate charge carriers that drive redox reactions. When TiO_2 is irradiated with photons of energy equal to or greater than its band gap, electrons are excited from the valence band to the conduction band, leaving behind holes in the valence band. These charge carriers migrate to the surface and participate in reactions with adsorbed species [30].

The efficiency of this process depends on several factors, including light absorption capacity, charge carrier mobility, recombination rate, and surface adsorption properties. One of the key advantages of TiO_2 is its strong oxidation potential, allowing it to degrade a wide range of organic pollutants non-selectively. However, the overall quantum efficiency is often limited by the rapid recombination of photogenerated electron–hole pairs, which dissipates energy as heat rather than driving chemical reactions [30].

To overcome the intrinsic limitations of TiO_2, particularly its wide band gap and high recombination rate, various modification strategies have been developed. Metal doping (e.g., Ag, Fe, Cu) introduces defect states within the band gap that can act as electron traps, improving charge separation. Noble metals such as Ag can also induce surface plasmon resonance (SPR), enhancing visible-light absorption and photocatalytic efficiency [36]. Non-metal doping (e.g., N, C, P,...) modifies the electronic structure of TiO_2 by narrowing the band gap [37]. Additionally, increasing the specific surface area through nano-structuring or porous architectures enhances adsorption of pollutants and provides more active sites for reactions. Immobilization of nanoparticles onto substrates also improves practical applicability while maintaining high catalytic efficiency [30], [38].

1.2.4 Photocatalytic Mechanism

The photocatalytic degradation mechanism of TiO_2 involves a series of photoinduced redox reactions. Upon UV irradiation, the following primary process occurs:

$TiO_2 + h\nu \rightarrow e^- (CB) + h^+ (VB)$

The photogenerated holes (h^+) can oxidize water or hydroxide ions to produce hydroxyl radicals:

$h^+ + H_2O \rightarrow \bullet OH + H^+$

$h^+ + OH^- \rightarrow \bullet OH$

Simultaneously, electrons in the conduction band reduce dissolved oxygen to form superoxide radicals:

$e^- + O_2 \rightarrow O_2\bullet^-$

These reactive oxygen species (ROS), particularly •OH, are highly oxidative and can attack organic molecules such as OTC, leading to their degradation through a series of intermediate steps and eventual mineralization into CO_2, H_2O, and inorganic ions. The efficiency of this mechanism is strongly influenced by the competition between charge carrier recombination and interfacial charge transfer reactions [29].

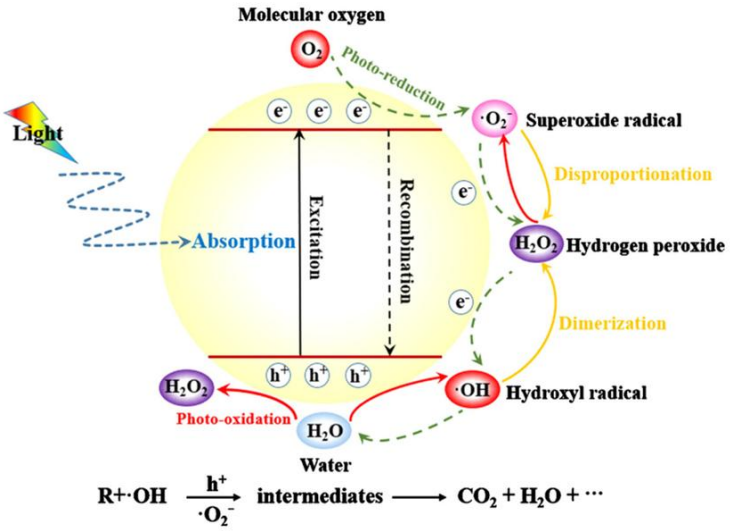

Figure 5. Photocatalytic Mechanism [29], [39]

1.3 Substrates

The immobilization of photocatalysts onto solid substrates is essential for practical applications, as it enables easy recovery, reuse, and integration into water treatment systems. A variety of substrates have been investigated, including glass, ceramics, polymers, and metals. Glass substrates are commonly used due to their transparency and smooth surface, which facilitate optical studies; however, their mechanical fragility limits large-scale applications. Ceramic substrates offer high thermal and chemical stability but can be costly and difficult to process. Polymer substrates provide flexibility and low cost but often suffer from poor thermal resistance and limited durability under UV irradiation. Among them, stainless steel, have attracted increasing attention due to their excellent mechanical strength, corrosion resistance, and scalability for industrial applications [40].

1.3.1 Composition of Stainless Steel

Stainless steel is an iron-based alloy primarily composed of iron (Fe) with a minimum chromium (Cr) content of approximately 10.5 wt%, which is essential for its corrosion resistance. In addition to chromium, stainless steels typically contain varying amounts of nickel (Ni), molybdenum (Mo), manganese (Mn), silicon (Si), and carbon (C), depending on the grade. For example, a commonly used austenitic stainless steel such as 304 contains ~18–20% Cr and 8–10.5% Ni, while 316 stainless steel includes additional Mo (~2–3%) to enhance corrosion resistance, particularly in chloride-containing environments [41].

max %	304	304L	316	316L	316LN	316H
Fe	balance	balance	balance	balance	balance	Balance
Cr	18–20	18–20	16–18	16–18	16–18	16–18
Ni	8.0–10.5	8.0–10.5	10.0–14.0	10.0–14.0	10.0–14.0	10.0–14.0
Mo	-	-	2–3	2–3	2–3	2–3
Mn	2.00	2.00	2.00	2.00	2.00	2.00
Si	0.75	0.75	0.75	0.75	0.75	0.75
N	0.10	0.10	0.10	0.10	0.10–0.30	-
P	0.045	0.045	0.045	0.045	0.045	0.045
C	max. 0.08	max. 0.03	max. 0.08	max. 0.03	max. 0.03	0.04–0.10

Figure 6. Composition of Stainless Steel [41]

Chromium plays a critical role by forming a thin, adherent, and self-healing passive oxide layer (primarily Cr_2O_3) on the surface, which protects the underlying metal from corrosion. Nickel stabilizes the austenitic phase, improving ductility and toughness, while molybdenum enhances resistance to pitting and crevice corrosion. The low carbon content minimizes carbide precipitation, which could otherwise degrade corrosion resistance [41].

1.3.2 Physical and Chemical Properties for Reactor Applications

The suitability of stainless steel as a reactor material arises from a combination of mechanical, thermal, and chemical properties. Mechanically, stainless steel exhibits high tensile strength, toughness, and fatigue resistance, allowing it to withstand pressure, flow-induced stress, and long-term operation in industrial systems. Its relatively high melting point (above 1400 °C) and good thermal conductivity enable it to tolerate elevated temperatures and thermal cycling without significant degradation [42].

Property	Units	SS 316L
Density	kg/m^3	8000
Elastic modulus	GPa	193
Thermal conductivity	W/m·K	16.3 at 100 °C; 21.5 at 500 °C
Specific heat 0-100 °C	J/kg·K	500
Electrical resistivity	nΩ·m	740
Tensile strength	MPa	485
Yield strength	MPa	170
Hardness	Rockwell	95

Figure 7. Physical properties of stainless-steel [43]

Chemically, the most important property is its excellent corrosion resistance, which is attributed to the formation of the passive chromium oxide layer. This passive film is stable over a wide range of pH conditions and can self-repair when damaged, making stainless steel particularly suitable for aqueous environments, including those containing dissolved oxygen and reactive species. In photocatalytic systems, where reactive oxygen species (ROS) such as hydroxyl radicals are generated, material stability is critical. Stainless steel demonstrates sufficient resistance to oxidative degradation under these conditions compared to many other metals [44].

Additionally, stainless steel surfaces can be modified through treatments such as acid etching, polishing, or oxidation, which alter surface roughness and chemical composition. These modifications are beneficial for improving coating adhesion and enhancing interfacial interactions with photocatalytic layers [44].

1.3.3 Interfacial Bonding with TiO_2 Coatings

The adhesion between TiO_2 coatings and stainless-steel substrates is governed by a combination of mechanical interlocking, chemical bonding, and interfacial diffusion. The native oxide layer on stainless steel, composed mainly of Cr_2O_3 and Fe oxides (Fe_2O_3/Fe_3O_4), plays a crucial role in facilitating bonding with TiO_2 [45].

During sol–gel deposition and subsequent thermal treatment, hydroxyl groups (–OH) present on both the TiO_2 precursor and the oxidized stainless-steel surface can undergo condensation reactions, forming metal–oxygen–metal (M–O–M) bonds, such as Fe–O–Ti or Cr–O–Ti linkages. These chemical bonds significantly enhance adhesion strength at the interface [45].

In addition to chemical bonding, surface roughness of the stainless-steel substrate contributes to mechanical interlocking, where the TiO_2 sol penetrates microscopic asperities on the surface and anchors upon drying and densification. Thermal treatment further promotes densification of the coating and improves interfacial cohesion [46].

Furthermore, diffusion processes at elevated temperatures may lead to the formation of a graded interface, reducing interfacial stress and improving coating stability. The combination of these mechanisms results in a robust and durable TiO_2 coating on stainless steel, suitable for repeated use in photocatalytic reactors [45], [46].

1.4 Materials Synthesis Methods

Various synthesis methods have been developed for preparing photocatalytic materials, including sol–gel, hydrothermal, solvothermal, chemical vapor deposition (CVD), and sputtering techniques. Hydrothermal and solvothermal methods enable precise control over crystal structure and morphology but often require high pressure and temperature conditions. CVD and sputtering produce highly uniform and adherent coatings; however, they involve complex equipment and high operational costs, limiting their scalability. Among these methods, the sol–gel and colloidal synthesis are techniques used widely for synthesizing TiO_2-based photocatalysts, especially for a coating purpose because of its simplicity and easy control [47].

1.4.1 Sol–Gel Synthesis

a) Mechanism

The sol–gel process is based on the transition of a system from a liquid “sol” (a colloidal suspension of particles) into a solid “gel” phase through a series of hydrolysis and condensation reactions. Typically, metal alkoxide precursors such as titanium isopropoxide (TTIP) with a molecular formula of $Ti\{OCH(CH_3)_2\}_4$, are used due to their high reactivity toward water [48].

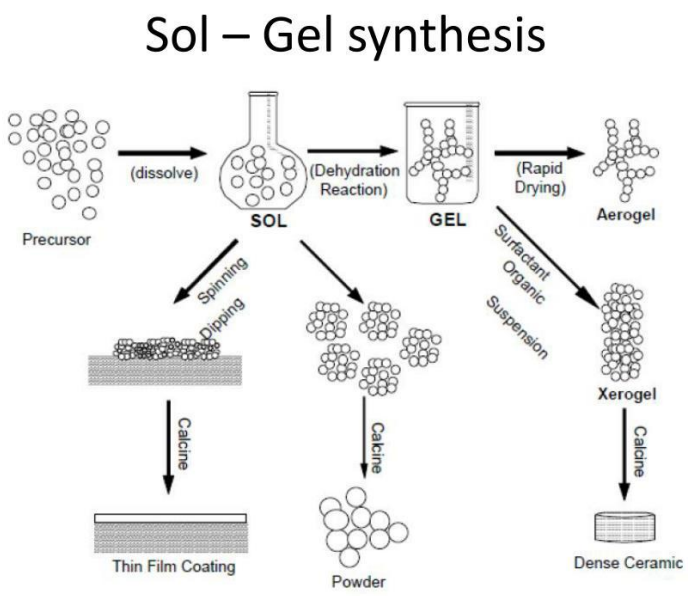

Figure 8. Sol-gel synthesis [47]

The process begins with hydrolysis, in which alkoxide groups (–OR) are replaced by hydroxyl groups (–OH) in the presence of water:

$Ti–OR + H_2O \rightarrow Ti–OH + ROH$

This step is highly sensitive to parameters such as water-to-precursor ratio, pH, temperature, and solvent type, which influence the rate of reaction and the structure of the resulting network [49]. Following hydrolysis, condensation reactions occur between hydroxylated species, forming Ti–O–Ti bonds and releasing water or alcohol:

$Ti–OH + Ti–OH \rightarrow Ti–O–Ti + H_2O$

$Ti–OH + Ti–OR \rightarrow Ti–O–Ti + ROH$

These reactions lead to the formation of a three-dimensional inorganic network, gradually increasing viscosity until a gel is formed. The resulting gel consists of a solid network enclosing a liquid phase. Subsequent drying removes the solvent, producing a porous xerogel, while thermal treatment (calcination) induces crystallization, densification, and removal of residues [50], [51].

An important feature of the sol–gel process is the ability to control nucleation and growth at the molecular level, allowing homogeneous incorporation of dopants such as Ag or the dispersion of nanoparticles such as P25. Additionally, parameters such as pH and complexing agents (e.g., acetylacetone, EDAS) can be used to moderate hydrolysis rates and prevent uncontrolled precipitation, enabling better control over film uniformity and microstructure [49]

b) Advantages and Limitations of the Sol–Gel Synthesis

The sol–gel method offers several key advantages that make it highly suitable for the synthesis of photocatalytic coatings. One of its most significant strengths is the molecular-level

homogeneity, which enables uniform distribution of dopants and additives, leading to improved photocatalytic performance. The process operates at relatively low temperatures compared to vapor-phase techniques, reducing energy consumption and allowing compatibility with a wider range of substrates, including metals and polymers [50], [51].

Another important advantage is the tunability of material properties. Parameters such as precursor concentration, solvent composition, pH, and aging time can be adjusted to control particle size, porosity, and surface area. This is particularly important for photocatalysis, where high surface area and accessible sites are essential. Furthermore, the sol–gel method is inherently compatible with coating techniques such as dip-coating, enabling the fabrication of uniform thin films on substrates with complex geometries [50], [51].

However, the sol–gel process also presents several limitations. One of the main challenges is shrinkage and cracking during drying and calcination, caused by capillary stresses as solvent evaporates. This can compromise film integrity and adhesion if not properly controlled. Additionally, the process is highly sensitive to environmental conditions such as humidity and temperature, which can affect reproducibility. The relatively slow processing time, including aging and drying steps, may also limit throughput in industrial applications. Finally, achieving high crystallinity often requires post-synthesis thermal treatment, which may affect substrate compatibility [51].

1.4.2 Colloidal Method

a) Mechanism

In this approach, the colloidal method is based on the dispersion of nanosized photocatalyst powders into a liquid medium to form a stable colloidal system. Unlike chemical sol formation, the nanoparticles are already synthesized and are then dispersed in a solvent such as water, ethanol, or mixed solvents [52].

Due to their nanoscale size, the particles exhibit Brownian motion and can remain suspended if sufficient stabilization is achieved. Dispersing agents, surfactants, or pH adjustment are often used to generate electrostatic or steric repulsion, preventing agglomeration and ensuring a stable colloidal dispersion [52], [53].

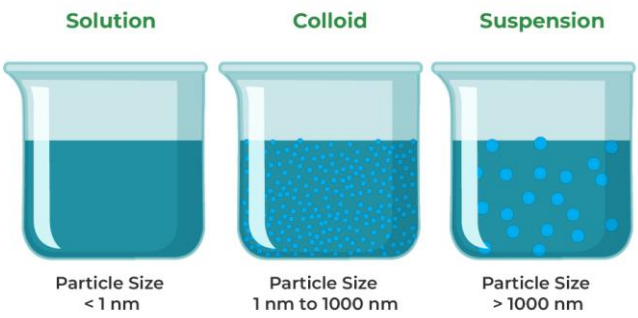

Figure 9. Colloidal synthesis

b) Advantages and Limitations of the Colloidal Synthesis

The colloidal method offers several advantages for photocatalytic coating fabrication. Due to the nanoscale dispersion of particles, it enables more uniform and homogeneous coatings compared to suspensions containing larger particles. The use of nanosized materials also helps retain a high specific surface area, which is beneficial for enhancing photocatalytic activity. In addition, the method is relatively simple and flexible, as it allows the direct use of pre-synthesized nanoparticles without complex chemical reactions. It also facilitates the incorporation of modified nanomaterials, such as doped TiO_2 or composite systems, thereby expanding the functional properties of the coating. Furthermore, the colloidal dispersion can be readily applied using conventional coating techniques such as dip-coating, spin-coating, and spray-coating [52], [53].

However, the method also presents several limitations. One of the main challenges is the risk of particle agglomeration if the dispersion is not properly stabilized, which can negatively affect coating uniformity and performance. The adhesion of the resulting film to the substrate is generally weaker than that of chemically bonded coatings produced by sol–gel methods. In addition, maintaining colloidal stability requires careful control of parameters such as pH and the use of appropriate dispersing agents. During drying, capillary forces may induce cracking in the film, especially if the coating thickness or particle concentration is not optimized. Finally, the overall film quality is highly dependent on the stability of the dispersion and the particle size distribution, making process control a critical factor [52], [53]

1.5 Coating Methods

The immobilization of photocatalytic materials onto solid substrates is essential for practical water treatment applications, as it enables catalyst recovery, reuse, and integration into continuous systems. Various coating techniques have been developed, including dip-coating, spin-coating, spray coating, and electrophoretic deposition, each with distinct advantages and limitations in terms of film quality, scalability, and process complexity. Spin-coating is widely used for producing highly uniform and smooth thin films with precise thickness control; however, it is limited to flat and relatively small substrates and involves significant material loss due to centrifugal forces. Spray coating is more suitable for large-scale applications and can cover complex geometries, but it often suffers from non-uniform thickness and reduced coating efficiency. Electrophoretic deposition offers strong adhesion and dense coatings, yet it requires conductive substrates and careful control of suspension stability and electrical parameters [47]

Among these methods, dip-coating is particularly attractive due to its simplicity, cost-effectiveness, and compatibility with sol–gel systems. It enables uniform coating of substrates with complex shapes while allowing good control over film thickness and microstructure. For these reasons, dip-coating is selected in this study for the fabrication of TiO_2-based photocatalytic coatings [47].

1.5.1 Dip-Coating Process

Dip-coating is a liquid-phase deposition technique in which a substrate is immersed in a precursor solution and then withdrawn at a controlled speed, forming a thin liquid film on its surface. The process consists of several stages: immersion, residence (or dwell time), withdrawal, liquid film formation, solvent evaporation, and solidification [47].

During immersion, the substrate surface is fully wetted by the solution, ensuring intimate contact between the liquid and the substrate. The dwell time allows equilibrium adsorption and penetration of the solution into surface irregularities. Upon withdrawal, a liquid film is entrained due to viscous drag forces acting against gravity and surface tension. The thickness of this film is governed by the balance between these forces and is commonly described by the Landau–Levich–Derjaguin (LLD) model [47].

After withdrawal, solvent evaporation leads to concentration of the precursor species, followed by gelation in sol–gel systems. Subsequent drying and thermal treatment result in densification, crystallization, and strong adhesion of the coating to the substrate. The ability to control each stage of this process makes dip-coating highly suitable for fabricating functional thin films.

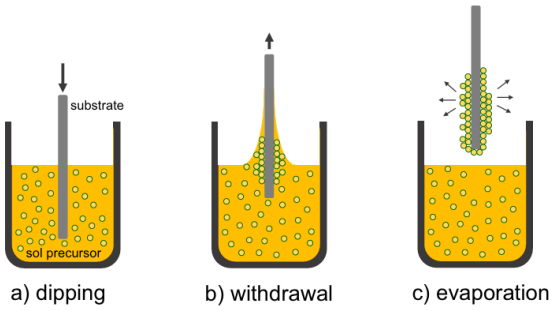

Figure 10. Dip-coating process [54]

1.5.2 Key Parameters of Dip-Coating

The properties of dip-coated films are strongly influenced by several key parameters that must be carefully controlled [55], [56].

- The withdrawal speed is one of the most critical factors, as it directly determines the film thickness. According to the LLD model, higher withdrawal speeds result in thicker films due to increased viscous drag. However, excessively high speeds can lead to instability and non-uniform coatings.
- The viscosity and concentration of the precursor solution also significantly affect film formation. Higher viscosity leads to thicker coatings, while solution concentration influences the amount of material deposited. In sol–gel systems, these parameters are closely linked to hydrolysis and condensation reactions, which determine the microstructure of the final film.
- Surface tension and wettability play an important role in ensuring uniform film formation. Good wetting of the substrate is necessary to avoid defects such as de-

wetting or film rupture. Surface treatments, such as cleaning or chemical modification, are often used to enhance wettability and improve coating quality.

- The evaporation rate of the solvent is another important factor. Rapid evaporation can lead to stress development and cracking, while controlled drying promotes uniform film formation. Environmental conditions such as temperature and humidity must therefore be carefully controlled.

Finally, the number of coating cycles and intermediate heat treatments influence the final thickness and structure of the coating. Multiple deposition cycles are often employed to achieve thicker films while minimizing defects [55].

1.5.3 Advantages and Limitations of Dip-Coating

Dip-coating offers several advantages that make it highly suitable for photocatalytic applications. It is a simple and low-cost technique that does not require complex equipment, making it easily scalable. The method allows uniform coating of substrates with complex geometries and provides good control over film thickness through adjustment of process parameters. It is also highly compatible with sol–gel chemistry, enabling homogeneous incorporation of dopants and precise control over microstructure [57].

Another key advantage is the ability to achieve strong adhesion between the coating and substrate, particularly when combined with appropriate surface preparation and thermal treatment. This is essential for ensuring long-term stability in photocatalytic reactors operating under flowing water conditions [56].

However, dip-coating also has some limitations. One of the main challenges is the formation of cracks during drying and calcination, especially in thicker films, due to capillary stresses. Achieving highly uniform coatings over very large surfaces can also be challenging if process parameters are not carefully optimized. Additionally, multiple coating cycles may be required to reach the desired thickness, which can increase processing time [56].

1.6 Materials Characterization Methods

A comprehensive understanding of photocatalytic coatings requires the integration of multiple characterization techniques to evaluate their structural, morphological, optical, and chemical properties. Each method provides distinct but complementary information, enabling correlation between material characteristics and photocatalytic performance.

1.6.1 X-ray Diffraction (XRD)

X-ray diffraction (XRD) is a fundamental technique used to determine the crystalline structure, phase composition, and crystallite size of photocatalytic materials. It operates based on the constructive interference of monochromatic X-rays scattered by periodic atomic planes in a crystalline material, following Bragg's law. In TiO_2-based systems, XRD is particularly important for identifying the presence of anatase, rutile, and brookite phases, as well as evaluating phase transformations induced by thermal treatment. Since anatase typically exhibits higher photocatalytic activity due to its favourable band structure and lower electron–

hole recombination rate, phase identification is critical. Additionally, crystallite size can be estimated using the Scherrer equation, providing insight into nanoscale features that influence surface reactivity. Therefore, XRD plays a central role in correlating crystal structure with photocatalytic efficiency [47]

1.6.2 Scanning Electron Microscopy (SEM)

Scanning electron microscopy (SEM) is used to investigate the surface morphology and microstructure of coatings. SEM employs a focused electron beam that scans the sample surface, generating signals such as secondary electrons that provide high-resolution images. For photocatalytic coatings, SEM is essential for analysing surface roughness, porosity, crack formation, and coating uniformity. In immobilized TiO_2 systems on stainless steel substrates, SEM allows direct observation of coating adhesion, surface coverage, and defect formation after dip-coating and calcination. These morphological characteristics strongly influence light absorption, pollutant adsorption, and overall photocatalytic performance [47].

1.6.3 Energy-Dispersive X-ray Spectroscopy (EDX)

Energy-dispersive X-ray spectroscopy (EDX), often coupled with SEM or TEM, is used to determine the elemental composition of materials. It is based on the detection of characteristic X-rays emitted when atoms are excited by an electron beam. In photocatalytic coatings, EDX is used to confirm the presence and distribution of elements such as Ti, O, and dopants. This is particularly important in the system to verify successful incorporation of dopants into the TiO_2 matrix and to assess its dispersion homogeneity. EDX mapping further allows spatial visualization of elemental distribution across the coating [47].

1.6.4 Inductively Coupled Plasma Optical Emission Spectroscopy (ICP-OES)

ICP-OES is used to detect and quantify trace metal elements in solution with high sensitivity. The technique involves ionizing the sample in a high-temperature plasma and measuring emitted light at characteristic wavelengths. In photocatalytic systems, ICP-OES is particularly important for evaluating metal leaching, such as Ti release from coatings. This is essential for assessing the long-term stability of the coating and its environmental safety in water treatment applications [58].

1.6.5 Profilometer

A profilometer is a widely used instrument for measuring the thickness and surface profile of thin films and coatings. In photocatalytic coatings, film thickness is an important parameter because it influences light absorption, charge carrier transport, and overall photocatalytic efficiency. Profilometry determines the thickness by scanning across a step edge between the coated and uncoated regions of a substrate and measuring the height difference. This technique provides accurate and non-destructive thickness measurements, making it suitable for evaluating the uniformity and quality of deposited films. In dip-coated samples, profilometer measurements are particularly useful for assessing the effects of coating parameters, such as withdrawal speed and solution properties, on the resulting film thickness [47].

1.7 Photocatalytic Performance Evaluation Methods

1.7.1 UV–Visible Spectroscopy (UV–Vis)

UV–Visible spectroscopy was employed to monitor the photocatalytic degradation of oxytetracycline (OTC) in aqueous solution. The technique measures the absorbance of OTC at its characteristic wavelength, which is proportional to its concentration according to the Beer–Lambert law. During photocatalytic treatment, the decrease in absorbance intensity indicates the degradation of OTC molecules by the photocatalyst. By comparing the absorbance before and after irradiation, the remaining OTC concentration and degradation efficiency can be determined. Therefore, UV–Vis spectroscopy serves as a simple and effective method for evaluating the photocatalytic performance of the prepared coatings [47].

1.7.2 Total Organic Carbon (TOC) Analysis

TOC analysis measures the total amount of carbon present in organic compounds within a sample. It evaluates the degree of mineralization by quantifying the conversion of organic carbon into CO_2. This is crucial in photocatalysis, as complete mineralization is the ultimate goal. Therefore, TOC provides information whether pollutants are fully degraded or merely transformed into intermediate compounds [59].

2 Experimental Section

This chapter describes the materials, methods, and procedures used to investigate the photocatalytic degradation of oxytetracycline (OTC) using the prepared coatings. It details the synthesis and characterization of the photocatalytic materials, the fabrication of the coating systems, and the setup for photocatalytic experiments, including reaction conditions and analytical techniques. The section provides a clear framework for reproducing the experiments and evaluating the performance of the coatings under controlled laboratory conditions.

2.1 Comparative Study of Photocatalytic Coating Fabrication Methods and Their Degradation Performance

2.1.1 Materials and chemicals

The chemicals used in this study were obtained from various commercial sources. Evonik Aeroxide P25 powder (P25) was purchased from Evonik (Brazil). Ethanol, N-[3-(trimethoxysilyl) propyl] ethylenediamine (EDAS, 97% purity), and titanium tetraisopropoxide (TTIP, ≥97% purity) were supplied by Sigma-Aldrich (USA). Polyethylene glycol (PEG) and silver acetate (AgAc, ≥99% purity) were obtained from Merck (Germany). 4-hydroxybenzoic acid (4-HBA) was purchased from Aldrich (Reagent Plus®, USA), and 2-methoxyethanol (MetOH, ≥99.5% purity) was sourced from Acros Organics (Belgium). Ultrapure Milli-Q water was used throughout all experimental procedures.

2.1.2 Experiments of catalyst synthesis

The Figure 11 below summarizes the catalyst synthesis procedures using two different methods: sol–gel and colloidal synthesis. Protocols 1–4 were carried out via the sol–gel method. The variations among these protocols involved the incorporation or absence of P25, PEG, or a combination of P25–PEG in solution B, with the aim of evaluating their influence on coating performance. As a result, four different catalysts were obtained: TiO_2–SiO_2–Ag (TSA), TiO_2–SiO_2–Ag–P25 (TSAP25), TiO_2–SiO_2–Ag–P25–PEG (TSAP25P), and TiO_2–SiO_2–Ag–PEG (TSAP).

Protocol 5 was based on a colloidal synthesis approach, in which nanoparticle powders were first functionalized and subsequently dispersed in a solvent to form a stable suspension suitable for dip-coating.

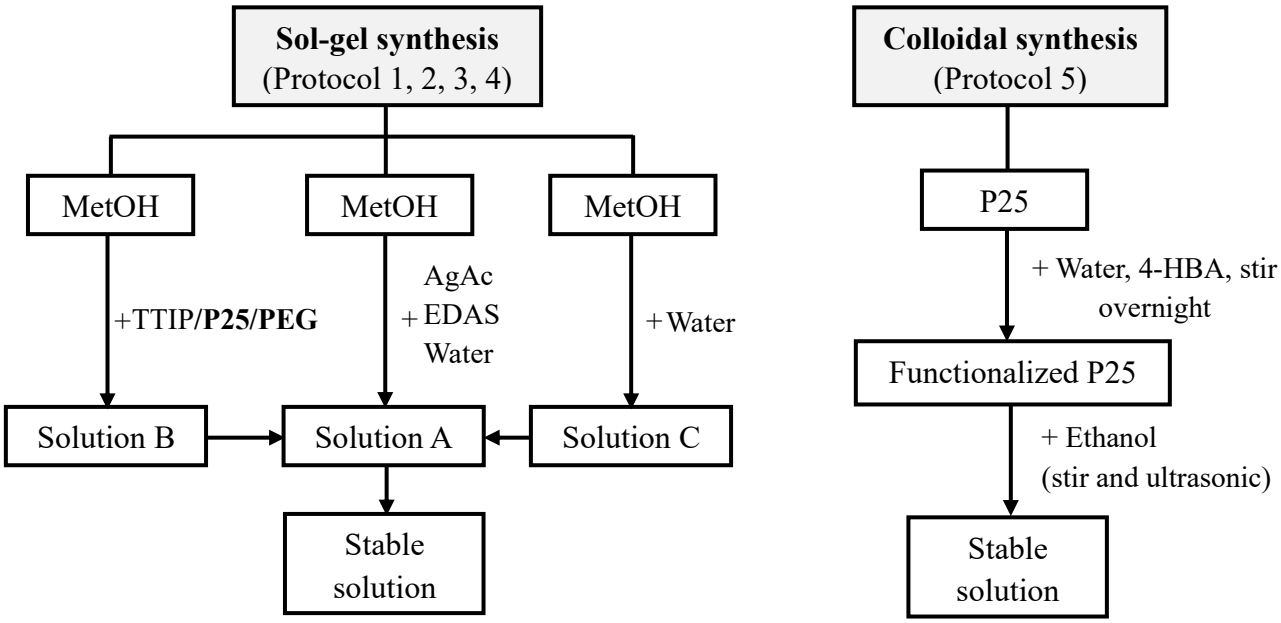

Figure 11. Summary of 2 coating synthesis methods

a) Protocol 1: TiO_2-SiO_2-Ag (TSA)

In this protocol, the material synthesis was adapted from the previous method [60]. The synthesis was carried out by first dissolving 0.171 g of silver acetate in 32 mL of MetOH in a 100 mL Erlenmeyer flask under continuous magnetic stirring. After complete dissolution, 0.7 mL of EDAS was added dropwise, and the mixture was stirred for 30 minutes. Subsequently, 0.17 mL of Milli-Q water was introduced, followed by an additional 30 minutes of stirring (solution A). In a separate Erlenmeyer flask (solution B), 19.7 mL of TTIP was dissolved in 96 mL of MetOH under stirring, and after 30 minutes, this solution was slowly added to the initial mixture while maintaining continuous stirring. In parallel, a third solution (solution C) was prepared by mixing 2.28 mL of Milli-Q water with 32 mL of MetOH and stirring for 15 minutes; this solution was then gradually added to the main reaction mixture. The final mixture was stirred for an additional 30 minutes to ensure homogeneity and completion of the synthesis. The resulting solution was subsequently transferred into a plastic storage bottle and kept for further use in the dip-coating section.

The solution obtained after synthesis is light yellow, transparent, and homogeneous, and it becomes more viscous; however, dip coating should be performed as soon as possible because the solution will turn into a solid gel after several hours.

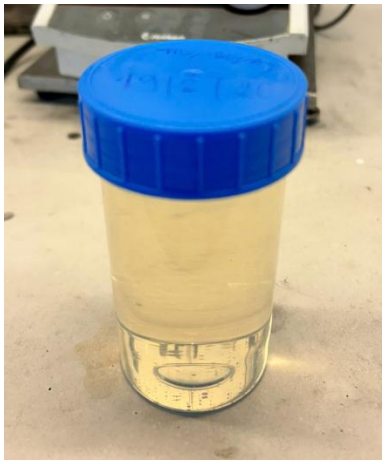

Figure 12. TSA solution

b) Protocol 2: TiO_2-SiO_2-Ag-P25 (TSAP25)

This synthesis follows the same overall procedure as the protocol 1, with a modification in the preparation of the solution B [60]. In this case, 17.6 mL of TTIP was dissolved in 96 mL of MetOH in a separate Erlenmeyer flask and stirred for 10 minutes. Then, 0.55 g of P25 was added to the solution, which was subsequently stirred at 80 °C for at least 12 hours (overnight) to ensure proper dispersion. Prior to adding this P25-containing solution to the primary mixture (Erlenmeyer 1), sonication was applied for approximately 15 minutes to further improve dispersion. All other steps including the dissolution of silver acetate, addition of EDAS and Milli-Q water, preparation of the third solution, and final stirring remained unchanged from the original protocol, with the resulting mixture being transferred to a plastic bottle for dip-coating.

The solution obtained after synthesis is milky white, with TiO_2 P25 particles suspended in it. This sample also needs to undergo dip coating soon because the solution will turn into a solid gel after a few hours.

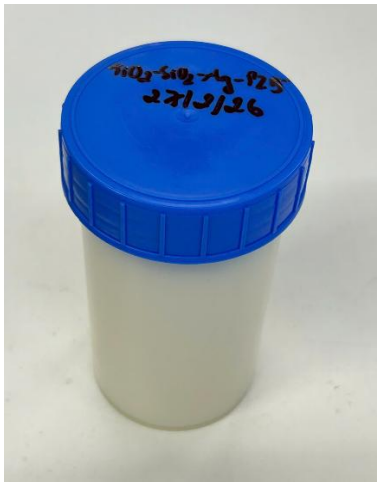

Figure 13. TSAP25 solution

c) Protocol 3: TiO_2-SiO_2-Ag-P25-PEG (TSAP25P)

This synthesis follows protocol 2, with modifications in the solution B with the present of PEG [61]. Here, 17.6 mL of TTIP was dissolved in 96 mL of MetOH containing 0.45 mL of PEG-600 and stirred for 10 minutes. Then, 0.55 g of P25 was added, and the mixture was stirred at 80 °C overnight. Prior to combining with Erlenmeyer 1, the P25 solution was sonicated for 15 minutes. All other steps remained the same as the protocol 2.

The solution obtained after synthesis also looks like protocol 2, ready for dip-coating.

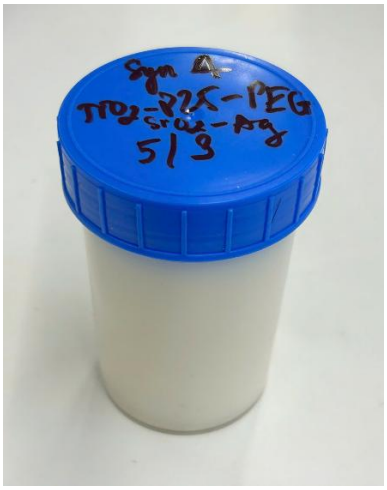

Figure 14. TSAP25P solution

d) Protocol 4: TiO_2-SiO_2-Ag-PEG (TSAP)

This synthesis protocol follows the same procedure as described in the protocol 1, with a modification in the preparation of the solution B referred from another research [61]. Specifically, in the second Erlenmeyer flask, 0.45 mL of PEG was dissolved in 96 mL of MetOH, stirring about 10 minutes, and then 19.7 mL of TTIP was incorporated into the mixture. The solution was stirred for 30 minutes before being added to the primary reaction mixture. All other steps and conditions remained unchanged from the original protocol.

The solution obtained after synthesis also looks like protocol 1, ready for dip-coating.

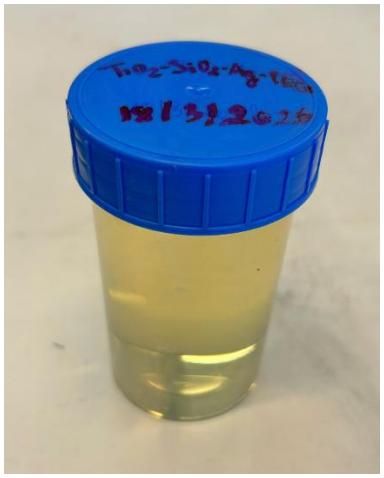

Figure 15. TSAP solution

e) Protocol 5: P25-4HBA (P25)

Based on the process of making P25 coating from its powder [62], and the patent **WO2013171297** [63], this protocol was modified with some factors. First, a saturated aqueous solution of 4-hydroxybenzoic acid (5 g/L) was prepared, and 15 g of P25 powder was added to 1 L of this solution. The mixture was stirred for 16 hours under light protection using aluminium foil, then centrifuged at 7000 rpm to separate the solid. The supernatant was discarded, and the remaining solid was redispersed in water, ultrasonicated, and centrifuged again at 7000 rpm. After removing the water, the solid was dried at 90 °C and finally ground to obtain a yellow powder.

Figure 16. Functionalized P25

After the synthesis of functionalized P25, a main solution was prepared by mixing 90 mL ethanol, 0.09 g 4-HBA, and 0.9 g functionalized P25, followed by ultrasonication for 30 minutes and stirring at 700 rpm for 2 hours. A secondary solution, consisting of 90 mL ethanol, 0.09 g 4-HBA, and 0.75 mL H_2O, was prepared separately and then added to the main solution. The combined mixture was ultrasonicated for 30 minutes and stirred for an additional 2 hours. Then the solution was allowed to decant for 1 to 16 hours to ensure stability, and then ready for dip-coating.

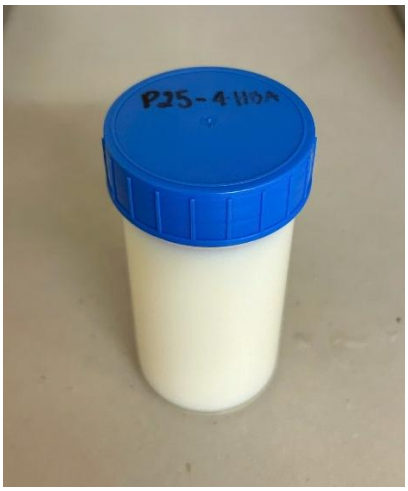

Figure 17. P25 solution

Note: All five protocols were adapted from previously reported studies; therefore, the molar, mass, and volume ratios used in each protocol are based on conditions reported as optimal in the literature.

Table 2. Total TiO_2 mass in solution before dip-coating

Protocol	Catalyst	Method	TiO_2 from precursor (g)	TiO_2 from P25 (g)	Total TiO_2 in final solution (g)
1	TSA	Sol-gel	5.15	0	5.15
2	TSAP25		4.6	0.55	5.15
3	TSAP25P		4.6	0.55	5.15
4	TSAP		5.15	0	5.15
5	P25	Colloid	0	0.9	0.9

The Table 2 presents the mass of TiO_2 in the solutions prior to dip-coating. The TiO_2 content in the sol-gel-derived solution is higher than that in the colloidal solution. Therefore, under identical dip-coating conditions, the coatings obtained from the sol–gel method are expected to yield a higher deposited mass of TiO_2 on the substrate compared to those from the colloidal method. To enable a fair comparison in subsequent analyses, the mass of the catalytic coatings on the substrates should be measured. However, direct measurement of the colloid-based coating mass was challenging due to its extremely low thickness. To address this issue, the colloid-based coating process was modified from a single dip-coating cycle to 6 cycles, allowing sufficient mass accumulation for reliable measurement. Therefore, these conditions will be maintained in the next experiments, with 1 dip-coating cycle applied for the sol-gel-based coatings and 6 cycles for the colloid-based coatings to ensure consistency in comparison.

2.1.3 Dip-coating

After the synthesis, the resulting solution stored in the plastic container was used for dip-coating. For each protocol, the solution was applied to five similar substrates as stainless steels with size of 7.5 cm x 2.5 cm x 0.8 mm (316L steel, Mecanic Systems, Braine-l'Alleud, Belgium) for subsequent activity testing and characterization. With 5 different protocols, it generates 25 samples in total.

Table 3. Dip-coating cycles of sol-gel and colloid coatings

Protocol	Catalyst	Method	Sample quantity	Dip-coating cycle
1	TSA	Sol-gel	5	1
2	TSAP25		5	1
3	TSAP25P		5	1
4	TSAP		5	1
5	P25	Colloid	5	6

Prior to dip-coating, the substrates were carefully cleaned to remove dust and surface impurities. The cleaning procedure involved washing with soap, rinsing thoroughly with Milli-Q water, and immersing the substrates in an acetone/ethanol bath within an ultrasonic cleaner

for 5 minutes. The substrates were then dried using compressed air before proceeding to dip-coating.

The dip-coating process (Dip-Coater, RDC 21-K, Bungard Elektronik, Germany) was carried out using a standardized program with the following parameters: an offset of 0 mm, a total dip distance of 162 mm (with a distance from the holder to the liquid surface of 145 mm), no dwell time at the up or down positions, a withdrawal speed of 200 mm/min, a dipping speed of 200 mm/min, an upward movement speed of 200 mm/min, and an upward dipping speed of 60 mm/min.

To ensure consistent coating dimensions on substrate (5.5 cm × 2.5 cm, corresponding to 13.75 cm^2), the solution level in the container was adjusted to a predefined reference mark prior to each coating cycle. If the solution level dropped below this mark during the process, additional solution was added to restore the initial level, thereby maintaining uniform coating area and reproducibility across samples.

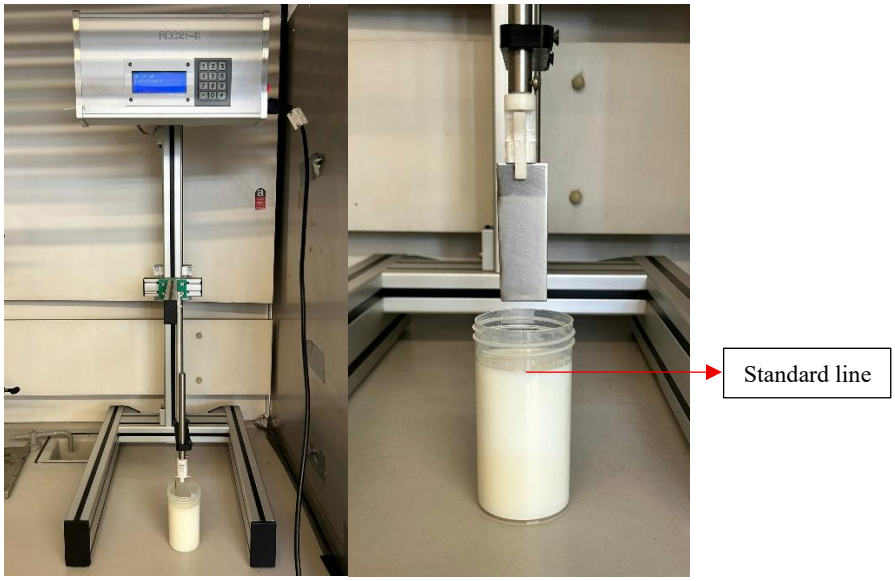

Figure 18. Dip-coating machine

2.1.4 Drying and calcination

After dip-coating, the substrates were dried at 100 °C for 80 minutes in a drying oven to remove residual solvents. Subsequently, the dried films were calcined at 500 °C for 1 hour to remove residual organics and achieve the desired crystalline structure and stability [60].

2.1.5 Direct measurement of coating mass

The use of steel substrates posed difficulties for weighing due to their relatively high density, magnetic issue and composition effects which reduced the stability and accuracy of measurements on an analytical balance. To minimize measurement error, aluminium substrates (Mecanic Systems, Braine-l'Alleud, Belgium) were selected as reference materials. Aluminium is lightweight and possesses a surface roughness comparable to that of steel, making it a suitable alternative for estimating coating mass.

The experimental procedure was as follows: aluminium substrates were cleaned using the same protocol as for the steel substrates, then dried and weighed 5 times to obtain an average initial mass. After dip-coating and drying at 100 °C for 2 hours to remove solvents, the coated substrates were weighed again 5 times to determine the average final mass. The coating mass was calculated using the following equation [61]:

Coating mass: $m_{coating} = m_{coated\ substrate} - m_{substrate}$

2.1.6 The degradation of OTC under UVC light with photocatalytic coating

After drying and calcination, the coated substrates were placed in a Petri dish, and 40 mL of 0.1 mM OTC solution was added. The Petri dish was then covered with a quartz plate and placed on an orbital shaker under UVC illumination at a distance of about 14 cm. The UVC light intensity was maintained at approximately 3.9-4.0 mW/cm² for 3 hours which was measured by a UVC detector. At 1-hour intervals, aliquots of the solution were collected to monitor the photocatalytic activity by measuring the decrease in OTC concentration using UV–Vis spectroscopy. After 3 hours, the solution was analysed for total organic carbon (TOC) to determine the extent of overall carbon degradation. Each batch will include three different catalysts and one control sample without a catalyst, allowing evaluation of the effect of UVC light alone on OTC degradation as well as the contribution of each catalyst to the overall degradation process.

Figure 19. UVC irradiation setup

2.1.7 The adhesion of TiO_2 coating on the substrate

A tape test used for checking the adhesion of coating, which was conducted in accordance with ASTM D3359, using Elcometer 99 tape. First of all, a grid pattern was created on the surface of the coated mortar sample by making parallel cuts, each approximately 20 mm in length, intersected by perpendicular cuts [47].

Figure 20. Elcometer 99 tape

A piece of Elcometer 99 tape, approximately three inches long, was then applied to the centre of the grid and gently pressed using an eraser to ensure proper contact. A visible change in the tape's appearance indicated full adhesion to the surface. The tape was subsequently removed in a smooth motion at a 180° angle from the opposite end of application [64]. Finally, the tested area was evaluated by comparing it with the classification patterns presented in Table 4 below.

Table 4. Adherence evaluation based on ASTM D3359 standard [65]

Classification	Descriptions	Minimum removal	Maximum removal
5B	The edges of the cuts are completely smooth; none of the squares of the lattice are detached.	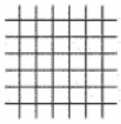	
4B	Small flakes of the coating are detached at intersections; less than 5% of the area is affected.	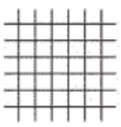	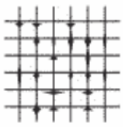
3B	Coating has flaked along the edges and at intersections; 5–15% of the area is affected.	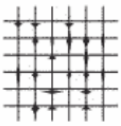	
2B	Coating has flaked along the edges and partly or wholly in large squares; 15–35% of the area is affected.		

1B	Coating has flaked along the edges of cuts in large ribbons and whole squares have detached; 35–65% of the area is affected.		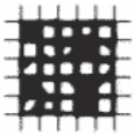
0B	Flaking and detachment worse than Grade 1B; more than 65% of the area is affected.		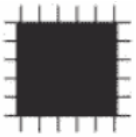

The selected catalyst will be based on the photocatalytic activity and their adherence level on the substrate.

2.1.8 Characterizations of sol-gel and colloid synthesis-based coatings

Table 5. Sample preparation for characterization methods

Method	Sample preparation
SEM (TESCAN/CLARA)	Five coated steel sheets were cut into smaller specimens for analysis. The prepared samples were then examined by scanning electron microscopy (SEM) to investigate their surface morphology.
XRD	Four catalysts were synthesized via the sol–gel method. After aging overnight, the sols transformed into gels. The gels were then dried at 100 °C until complete removal of residual water was achieved. The resulting solids were subsequently calcined at 500 °C for 1 hour (like coating's conditions). After calcination, the materials were ground into fine powders [66] The obtained powders from those four catalysts, together with a commercial TiO_2 powder (P25) calcined at 500 °C for 1 hour, were characterized by X-ray diffraction (XRD) to determine their phase composition and crystallinity.

2.1.9 Evaluation of photocatalytic efficiency of sol-gel and colloid synthesis-based coatings

Table 6. Sample preparation for photocatalytic efficiency analysis methods

Method	Sample preparation
UV-Vis (Genesys 150, Thermo Scientific)	At each reaction interval, 1–1.5 mL of sample was collected for UV–Vis analysis to monitor the decrease in OTC absorbance at 355 nm and determine the degradation efficiency.
TOC analysis (TOC-L, Shimadzu)	TOC was measured before and after the photocatalytic reaction to evaluate organic carbon removal. At least 15 mL of sample was required for each TOC measurement.

2.2 Process Optimization of Photocatalytic Coating for Enhanced OTC Degradation

Based on the result of photocatalytic activity and adherence of TiO_2 coating compiled in the previous section, the protocol 5 was chosen to optimize it by changing different parameters following:

2.2.1 Effects of TiO_2 powder types on the particle deposition in the solution before dip-coating process

Two types of TiO_2 powder were considered to use to test the stability of solution obtained in the protocol 5: (1) P25 from Evonik (Degussa) and (2) pure TiO_2 powder (98-100.5%) from Thermo Scientific. All conditions in protocol 5 was kept remain to check the stability of the obtained solution as well as the particle deposition.

After synthesis, the obtained solution was left undisturbed for 2 days to evaluate particle sedimentation. The degree of deposition was determined by comparing the initial mass of P25 powder added into the solution with the mass of particles collected at the bottom of the container after the settling period. From this experiment, the percentage of particle sedimentation was calculated, providing an indication of the stability and dispersion behaviour of the suspension.

2.2.2 Effect of substrate nature on colloidal coating loading

As mentioned earlier, accurately measuring coating mass on steel substrates is challenging. Therefore, glass (VWR, Belgium) and aluminium (Mecanic Systems, Braine-l'Alleud, Belgium) were selected as representative substrates with lower mass but distinctly different surface characteristics. The aim is to evaluate how surface properties influence the interaction and loading behaviour of colloidal-based coatings.

The substrate preparation and cleaning procedures followed the same protocol of stainless-steel as in previous experiments. Before coating, the surface roughness of both substrates was measured using a profilometer at multiple locations to obtain representative values. The samples were then coated under identical dip-coating conditions, using the same colloidal concentration and withdrawal speed. Six coating cycles were performed to ensure sufficient mass accumulation for reliable measurement.

After coating, all samples were dried at 100 °C for 2 hours and calcined at 500 °C in 1 hour to remove remaining solvent. The coating mass was determined by weighing the samples before and after coating using a high-precision analytical balance (±0.01 mg accuracy). Each measurement was repeated 5 times, and the average value was used to minimize experimental error.

Finally, the results were compared between glass and Al substrates to assess the influence of surface roughness and substrate characteristics on colloidal coating loading behaviour.

2.2.3 Coating layer number on steel substrate

Regarding the recommendations from the patent **WO2013171297** [63]**,** it is possible to dip many layers for the substrate until getting the desired photocatalytic activity. Therefore, the optimization of the coating layers would be following the Table 7 below.

Table 7. Test of coating layers

No.	Dip times	Calcination temperature	Calcination time
1	6	500 °C	1h
2	9		
3	12		
4	15		
5	18		
6	21		

The number of dip-coating layers was varied from 6 to 21 layers. A minimum of 6 layers was selected because a smaller number of coatings would produce an extremely thin film, making it difficult to accurately measure its mass and resulting in insufficient coverage and low photocatalytic activity.

On the other hand, the upper limit of 21 layers was chosen because excessively thick coatings can hinder light penetration and limit the accessibility of active sites. This can reduce photocatalytic efficiency due to mass transfer limitations and possible internal shading effects within the film. Additionally, overly thick layers may increase the risk of cracking or poor adhesion due to accumulated internal stress. Therefore, the range of 6–21 layers was selected to balance coating measurability, structural stability, and effective photocatalytic performance.

Samples with different dip-coating layers will be reacted with OTC under UVC, and their results continued analysed by UV-vis, TOC analysis and tape test to choose the best sample.

2.2.4 Calcination temperature (coated stainless-steel samples)

Table 8. Test of calcination temperature

No.	Dip times	Calcination temperature	Calcination time
1	18	300 °C	1h
2		400 °C	
3		500 °C	
4		600 °C	

The calcination temperature range was set between 300 °C and 600 °C to ensure a meaningful balance between sufficient thermal activation and avoidance of structural degradation. The lower limit of 300 °C was selected because temperatures below this are generally insufficient to achieve proper crystallization of TiO_2, which can lead to weak coating formation and poor adhesion to the steel substrate.

The upper limit of 600 °C was chosen to prevent excessive thermal effects such as particle sintering, grain growth, and increased thermal stress at the coating–substrate interface. These effects can reduce surface area, lower photocatalytic activity, and increase the risk of coating defects such as microcracks or delamination, while also unnecessarily increasing energy consumption. Therefore, 300–600 °C represents a practical and effective range for evaluating the influence of calcination temperature on coating performance.

Samples with different calcination temperatures will be reacted with OTC under UVC, and their results continued analysed by UV-vis and TOC analysis, as well as the tape test to choose the most optimal sample.

2.2.5 Calcination time (coated stainless-steel samples)

Table 9. Test of calcination time

No.	Dip times	Calcination temperature	Calcination time
1	18	400 °C	1h
2			2h
3			3h
4			4h

The calcination time was investigated from 1 hour to 4 hours because excessively short or long heat treatment durations may negatively affect the coating properties. Calcination times shorter than 1 hour may not provide sufficient time for TiO_2 particles to establish strong interparticle connections and proper bonding with the steel substrate, resulting in weaker coating stability and lower adhesion performance.

On the other hand, excessively long heat treatment durations, such as 5–6 hours, may introduce several undesirable effects on the coating system. Prolonged exposure to high temperatures can promote further oxidation of the steel substrate and enhance nanoparticle agglomeration and grain growth, reducing the specific surface area and consequently lowering photocatalytic activity. From a practical perspective, longer calcination times also increase energy consumption and processing cost, making the process less efficient for potential large-scale applications. Therefore, 1 hour and 4 hours were considered reasonable lower and upper limits, respectively, for evaluating the influence of calcination time on coating performance.

Samples with different calcination times will be reacted with OTC under UVC, and their results continued analysed by UV-vis and TOC analysis, as well as the tape test to choose the most optimal sample.

2.3 Characterizations of the optimal coating

2.3.1 Coating mass

Through the optimization of coating layers, the optimal coating can provide a significantly higher coating mass compared to the 6-layer samples used in the screening stage, so direct measurements on the steel substrate could be performed without requiring a reference substrate. The procedure was carried out in the same manner as previously described.

2.3.2 Coating thickness

The thickness of optimal coating was measured using a profilometer. However, because of the rough surface of the steel substrate, a glass substrate coated under the same conditions was additionally used as a reference for thickness determination.

2.3.3 Coating morphology

The coated steel sheets were cut into smaller specimens for further analysis. The prepared samples were then characterized using scanning electron microscopy coupled with energy-dispersive X-ray spectroscopy (SEM–EDX) to investigate the surface morphology and determine the elemental composition of the coating.

2.3.4 Coating crystallinity and phase composition

Since the optimized coating consisted solely of P25 nanoparticles without the addition of binders or other supporting components, the coating layer was formed by the adhesion of P25 particles onto the substrate during the calcination process. Therefore, the crystallinity and phase composition of the coating were evaluated indirectly using P25 powder treated under identical calcination conditions as the coated samples.

Specifically, P25 powder was calcined at 400 °C for 4 h, corresponding to the thermal treatment applied during the coating preparation. After calcination, the powder samples were characterized by X-ray diffraction (XRD) analysis to investigate the crystallinity and phase composition, as well as any structural changes induced by the calcination process.

2.4 Leaching test of the optimal coating on stainless-steel substrate

The testing protocol followed the same procedure as the OTC degradation experiment, with the only difference being the extended reaction time. Specifically, the coated substrate was placed in a Petri dish containing 40 mL of 0.1 mM OTC solution. The Petri dish was covered with a quartz plate and positioned on an orbital shaker under UVC irradiation at a distance of 14 cm. The UV light intensity was maintained at approximately 3.9–4.0 mW/cm² for 24 h. After irradiation, the solution was collected and analysed by ICP–OES to determine Ti leaching from the coating [60], [61].

2.5 Reusability test

The reusability of the TiO_2 coating was evaluated through repeated cycles of photocatalytic degradation using the same coated specimen. After each photocatalytic cycle under identical UVC irradiation conditions, the coated sample was removed, rinsed with milli Q water to

eliminate residual contaminants, and reused in a fresh oxytetracycline (OTC) solution. The procedure was repeated for 7 cycles, and the degradation efficiency in each cycle was determined using UV–Vis spectroscopy at 355 nm and TOC analysis to assess the stability and reusability of the coating [61] [67].

After several photocatalytic cycles, the degradation efficiency may decrease due to the accumulation of intermediate pollutants and reaction by-products on the TiO_2 surface. To restore the activity of the coating, a regeneration process was performed [61].

The regeneration procedure followed the same protocol as the OTC degradation experiment, with the main difference being that Milli-Q water was used instead of the polluted solution during irradiation under a UVC lamp for 3 h and 16 h. Under UVC irradiation, TiO_2 generates reactive species such as hydroxyl radicals, which can decompose and remove the adsorbed by-products from the coating surface. This process restores the exposed active sites and reactivates the photocatalyst due to the self-cleaning properties of TiO_2 [61]. After the regeneration treatment, the coating was reused for OTC degradation experiments to evaluate the recovery of its photocatalytic activity.

Table 10. Procedure of reusability test

	Solution during irradiation	Time	Cleaning procedure before next cycle
Cycle 1	OTC 0.1 mM	3 h	Milli Q water, drying 100 °C for 15 minutes
Cycle 2	OTC 0.1 mM	3 h	Milli Q water, drying 100 °C for 15 minutes
Cycle 3	OTC 0.1 mM	3 h	Milli Q water, drying 100 °C for 15 minutes
Cycle 4	OTC 0.1 mM	3 h	Milli Q water, drying 100 °C for 15 minutes
Cycle 5	OTC 0.1 mM	3 h	Milli Q water, drying 100 °C for 15 minutes
Regeneration 1	Milli Q water	3 h	Milli Q water, drying 100 °C for 16 hours
Cycle 6	OTC 0.1 mM	3 h	Milli Q water, drying 100 °C for 15 minutes
Regeneration 2	Milli Q water	16 h	Milli Q water, drying 100 °C for 15 minutes
Cycle 7	OTC 0.1 mM	3 h	Milli Q water, drying 100 °C for 15 minutes

2.6 Adsorption Test of P25 coating and powder

Adsorption experiments were conducted to evaluate the adsorption behaviour of oxytetracycline (OTC) on the P25 coating and P25 powder systems under dark conditions. The purpose of this experiment was to distinguish the contribution of adsorption from the photocatalytic degradation process during UVC irradiation.

For the P25 coating system, the coated substrate prepared under optimized conditions was immersed in 40 mL of a 0.1 mM OTC solution. For the powder system, half the mass of the P25 coating used for the powder form (since only one side of the coated sheet is exposed to the OTC solution) was dispersed in 40 mL of a 0.1 mM OTC solution. Both systems were placed on the same shaker to ensure consistent and uniform mixing throughout the experiment.

The adsorption experiments were carried out entirely in the dark at room temperature for 1 h without UVC irradiation. Liquid samples were collected every 10 minutes to monitor the

adsorption behaviour of OTC onto the catalyst surfaces. The collected samples were analysed using UV–Vis spectroscopy to determine the remaining OTC concentration in the solution.

The adsorption efficiency was calculated based on the decrease in OTC concentration during the dark treatment. The obtained results were used to evaluate the adsorption capability of the P25 coating and P25 powder systems and to distinguish adsorption effects from photocatalytic degradation in subsequent experiments.

2.7 Comparison of the Photocatalytic Activity between P25 coating and powder

Based on the coating mass obtained from the previously optimized sample, an equivalent mass of P25 powder was prepared to compare the photocatalytic performance of the P25 coating and powder systems. The experimental procedure and operating conditions were maintained identical for both systems to ensure a reliable comparison. In each experiment, 40 mL of 0.1 mM OTC solution was used, and the photocatalytic reaction was conducted for 3 h under UVC irradiation (UVC intensity of 3.9-4.0 mW/cm^2). Both systems were placed on the same shaker to ensure consistent mixing conditions throughout the experiment.

Prior to UVC irradiation, the samples were kept under dark conditions with continuous shaking for 15 minutes to evaluate the adsorption of OTC onto the catalysts. During the 3 h irradiation period, liquid samples were collected at reaction times of 5, 10, 20, 30, 60, 120, and 180 minutes to monitor the degradation behaviour of OTC in both systems. The collected samples were analysed using UV–Vis spectroscopy and total organic carbon (TOC) analysis to evaluate and compare the photocatalytic degradation efficiency and mineralization performance of the P25 coating and P25 powder systems.

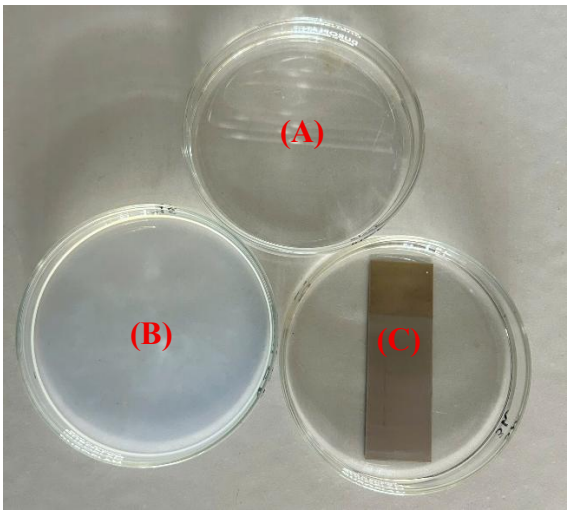

Figure 21. Sample preparation (A) OTC, (B) OTC and P25 powder, (C) OTC and P25 coating

3 Results and Discussions

This chapter presents and analyses the experimental results obtained from the photocatalytic degradation of oxytetracycline (OTC) using the prepared coatings. The findings are discussed in detail to evaluate the material properties, photocatalytic performance, degradation efficiency, and the influence of different experimental conditions. Comparisons with previous studies are also provided to highlight the significance of the results and the potential improvements achieved in this work.

3.1 Results of Comparative Study of Photocatalytic Coating Fabrication Methods and Their Degradation Performance

3.1.1 Results of visual characteristics of single-cycle photocatalytic coatings

The Figure 22 below presents five different catalytic coatings on steel sheets obtained after a single dip-coating step, followed by drying and calcination.

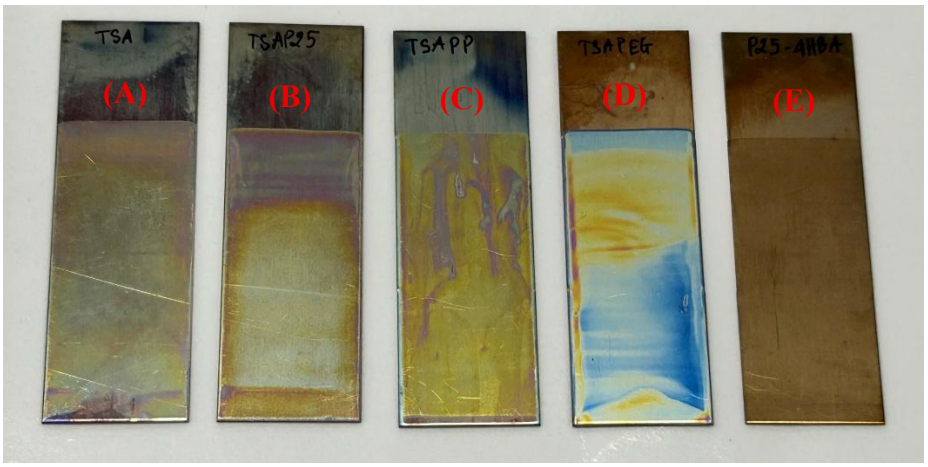

Figure 22. Five synthesized coatings with a single cycle of dip-coating (A) TSA, (B) TSAP25, (C) TSAP25P, (D) TSAP, (E) P25

Visually, the Figure 22 (A) TSA, (B) TSAP25, (C) TSAP25P, (D) TSAP (coatings derived from the sol–gel method) appear significantly thicker than that prepared via the colloidal method. The sol-gel-based coatings effectively obscure the colour of the steel substrate, indicating a higher film thickness and coverage. In contrast, the colloidal coating remains relatively transparent, allowing the substrate colour to be clearly observed. This observation is consistent with previous studies, which report that colloidal synthesis typically produces ultrathin films at the nanoscale [68]. That's why increasing the cycles of dip-coating for colloid-based coating is necessary. However, quantitative analysis of the coating mass should be conducted in subsequent steps to provide more persuasive evidence.

3.1.2 Results of direct measurement of coating mass

The Table 11 and Table 12 below present the mass measurement results for a representative sample from the sol–gel-based coatings (TSAP selected) and the colloid-based coating (P25). These results do not imply that the coating mass of TSAP is identical to that of other sol–gel-based coatings; rather, they are intended to illustrate the general difference in coating mass between the sol–gel-based and colloid-based deposition methods.

Table 11. The mass of sol-gel based coating

1 layer of sol-gel-based coating on Al substrate		
Repeated	**Before coating (g)**	**After coating (g)**
1	3.7513	3.75226
2	3.7513	3.75224
3	3.75128	3.75223
4	3.75135	3.75224
5	3.75131	3.75226
Average	3.751308	3.752246
Coating mass (mg)	**0.938**	

The Table 11 shows that the average coating mass obtained from the sol–gel method is about 0.938 mg, whereas the average mass of the colloid-based coating is 0.426 mg showed in the Table 12. Despite increasing the number of dip-coating cycles to 6, the coating mass produced by the colloidal method remains significantly lower than that of the sol–gel method. Nevertheless, these approximate mass values provide an important basis for ensuring that subsequent comparisons are meaningful from a quantitative perspective.

Table 12. The mass of colloid based coating

6 layers of colloid-based coating on Al substrate		
Repeated	**Before coating (g)**	**After coating (g)**
1	3.77294	3.77338
2	3.77295	3.77338
3	3.77293	3.77334
4	3.77298	3.77343
5	3.77295	3.77335
Average	3.77295	3.773376
Coating mass (mg)	**0.426**	

3.1.3 Characterizations by SEM

The surface morphologies of the bare steel substrate and the synthesized coatings are illustrated in Figure 23 below.

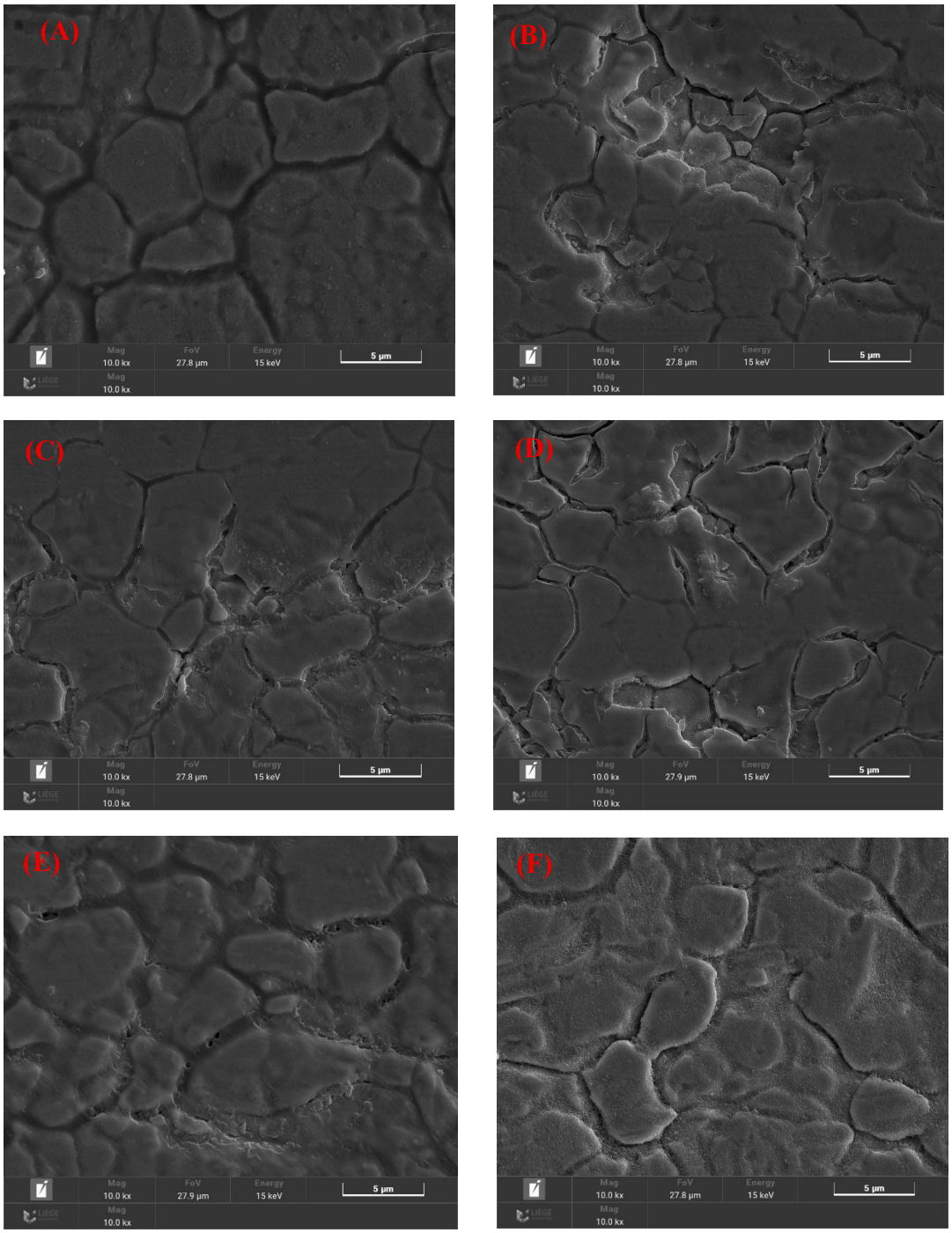

Figure 23. SEM images of (A) Steel, (B) TSA coating, (C) TSAP25 coating, (D) TSAP25P coating, (E) TSAP coating, (F) P25 coating at 10 kx magnitude

The uncoated steel surface from the Figure 23 (A), exhibits a highly irregular morphology with intrinsic cracks and high roughness.

For the sol–gel derived coatings showed in the Figure 23 (B), (C), (D), (E), the precursor solution successfully covers the steel substrate, transitioning into an interconnected matrix.

However, rather than forming a seamless film, these coatings exhibit distinct cracking patterns. This phenomenon is highly characteristic of sol-gel coatings subjected to high-temperature calcination, where severe tensile stress arises from volume shrinkage and the mismatch of thermal expansion coefficients between the organic-inorganic gel matrix and the steel substrate [69]. Despite these thermal cracks, the domains of the TSA, TSAP25, TSAP25P, and TSAP coatings remain dense and adhere to the substrate, mostly masking the underlying steel morphology.

A fundamentally different deposition mechanism is observed for the colloidal-derived P25 coating from the Figure 23 (F). Unlike the gel network of the sol-gel samples, the colloidal method results in the random deposition of discrete P25 nanoparticles and small aggregates on the steel surface rather than a seamless film, leaving parts of the substrate exposed.

Although the TSAP25P and TSAP coatings were expected to exhibit a porous structure due to the addition of PEG, no distinct pores were observed in the SEM images. This may be attributed to the formation of pores with dimensions below the resolution limit of the SEM at the magnification used [70].

Nevertheless, PEG addition appeared to improve the coating integrity by reducing crack formation. As shown in Figure 23 (E), TSAP coating exhibited a more uniform surface with fewer visible cracks. Similar observations have been reported by Bing Guo et al., who found that PEG-assisted sol-gel TiO_2 films could reducing crack generation after calcination, whereas films prepared without PEG exhibited severe cracking [71]. Regarding TSAP25P and TSAP25, smaller cracks were observed compared to the TSA sample. This indicates that the addition of P25 helped alleviate shrinkage stresses during film formation and calcination, thereby reducing the severity of coating cracks [72].

To gain a deeper insight into the microstructural features at the nanoscale, the coatings were further examined at an ultra-high magnification of 100 kx, as presented in Figure 24 below.

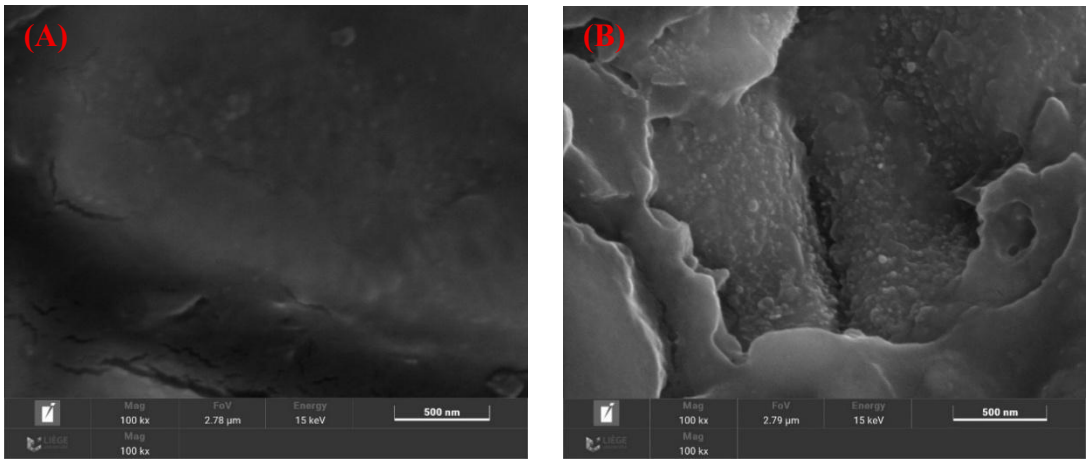

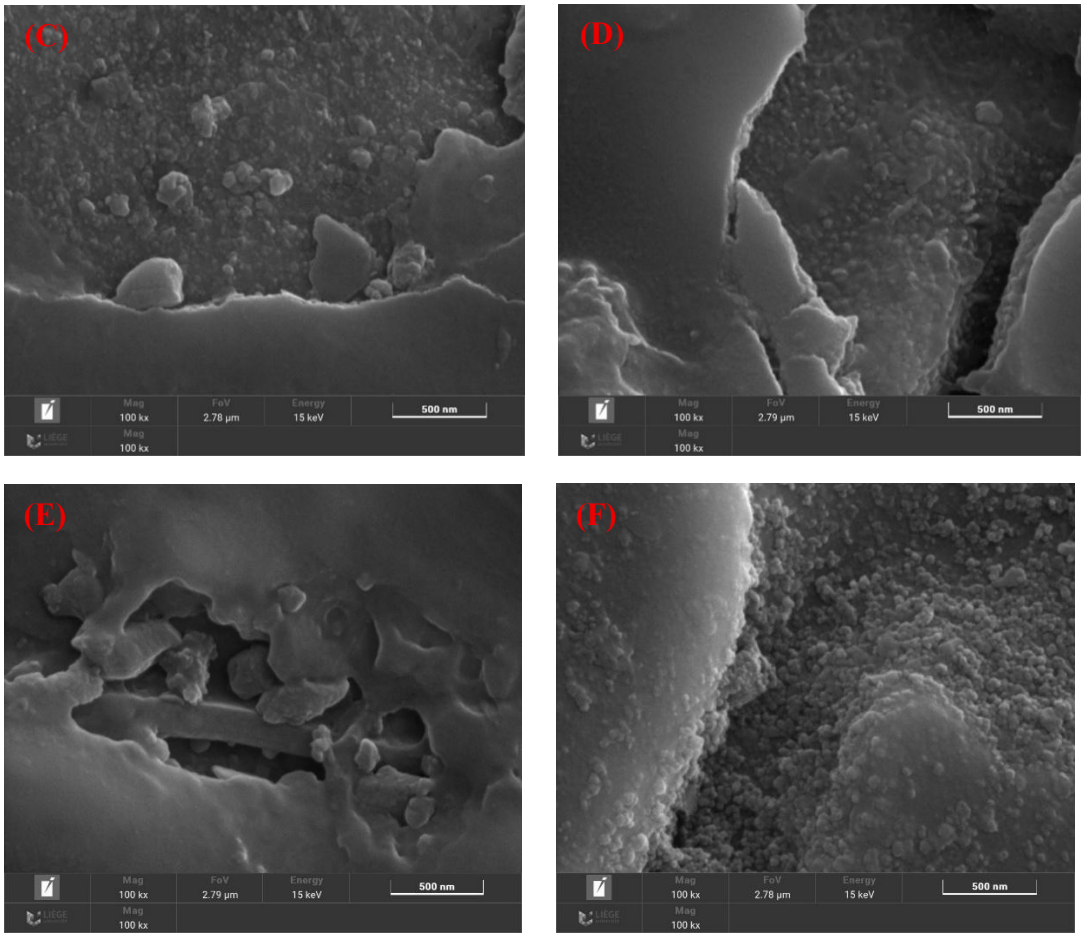

Figure 24. SEM images of (A) Steel, (B) TSA coating, (C) TSAP25 coating, (D) TSAP25P coating, (E) TSAP coating, (F) P25 coating at 100 kx magnitude

The Figure 24 (A) showed the surface of steel without coating that allows the comparison with the coated samples. A common characteristic observed for the Figure 24 (B), (C), (D), and (E) (sol-gel based coatings) was that the TiO_2 appears as a compact layer formed by clustered particles, which made it difficult to clearly see the boundary of each particle. These may be attributed to the hydrolysis-condensation reactions and subsequent particle growth during calcination. During solution formation, the hydrolysis and condensation reactions of the titanium precursor generate primary particles that gradually form a three-dimensional network. If these reactions proceed too rapidly, particle growth becomes difficult to control, leading to the formation of larger aggregates and a less homogeneous coating structure. Moreover, agglomeration becomes more pronounced during calcination, where thermal energy promotes particle growth and coalescence [54]. As a result, some particles are covered or overlapped by others, leading to a reduction in the exposed active sites available for pollutant adsorption and photocatalytic reactions.

In contrast, the P25 coating exhibited a more uniform and well-dispersed distribution of TiO_2 nanoparticles across the stainless-steel substrate. As this coating was prepared directly from commercial P25 powder without the incorporation of binders or additional components such as SiO_2 and Ag, the TiO_2 nanoparticles remained largely exposed on the surface. Although some degree of particle agglomeration occurred during calcination due to the tendency of

nanoparticles to reduce their surface energy through coalescence, the agglomeration was relatively limited. The individual particle boundaries could still be clearly distinguished, indicating that complete fusion of the nanoparticles had not occurred. Consequently, a larger fraction of the catalyst surface remained accessible, providing more exposed active sites for pollutant adsorption and photocatalytic reactions.

3.1.4 Characterizations by XRD

Figure 25 below shows the XRD patterns of (a) P25, (b) TSAP25P, (c) TSAP25, (d) TSAP and (e) TSA samples under the powder form. Among them, powder samples of (b), (c), (d), (e) were derived from sol-gel method.

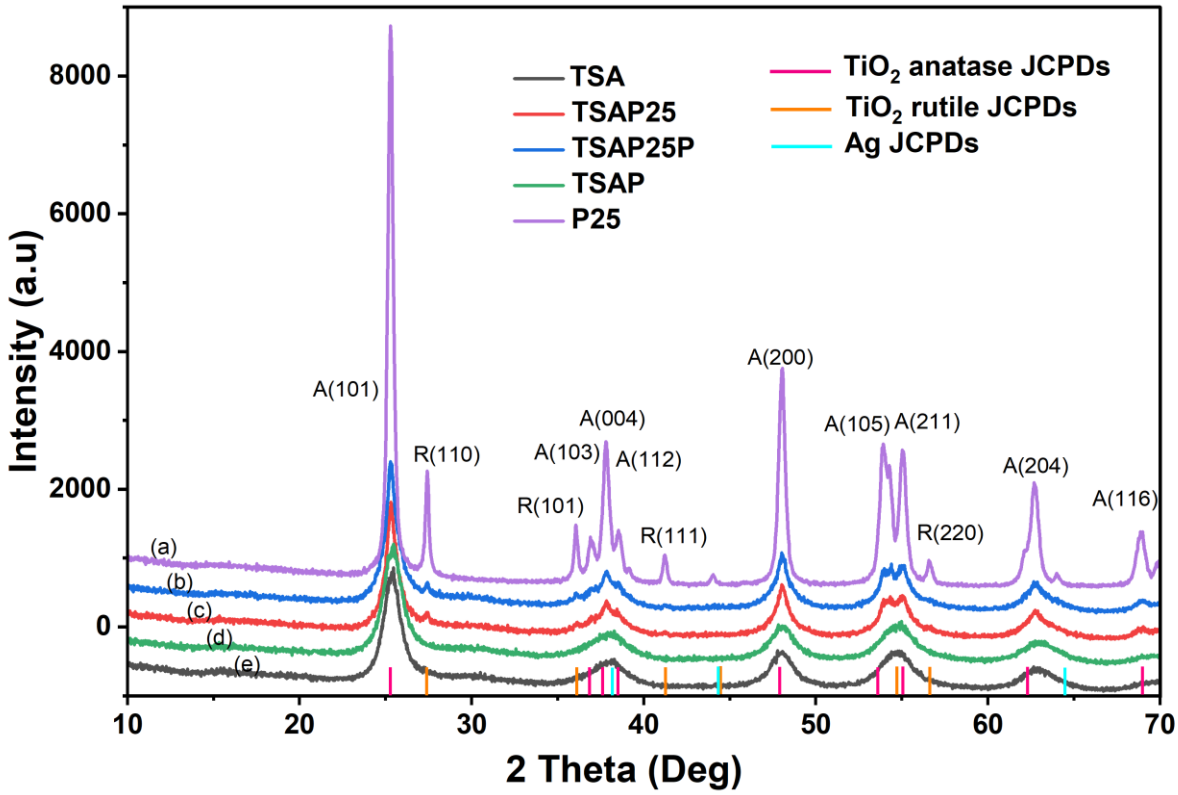

Figure 25. XRD patterns of photocatalytic powder calcined at 500 °C in 1 hour (a) P25, (b) TSAP25P, (c) TSAP25, (d) TSAP, (e) TSA

The P25 powder sample (a) clearly exhibited all characteristic anatase and rutile peaks with high intensity, in good agreement with the standard TiO_2 diffraction data.

A clear difference in diffraction peak intensity and peak sharpness can be observed between the sol-gel based samples with and without P25. In general, the XRD pattern of TSAP25P (b) is similar to that of TSAP25 (c), while TSAP (d) shows a similar pattern to TSA (e). This suggests that PEG did not significantly affect the crystalline phase composition after calcination, likely because PEG was thermally decomposed during the calcination process.

In addition, no distinct diffraction peaks corresponding to metallic Ag were observed in the XRD patterns. This can be attributed to the overlap between the strongest Ag diffraction peak,

Ag (111) at approximately 38.1°, and the anatase TiO_2 (004) peak located at approximately 37.8°, which may mask the Ag signal. Furthermore, the low Ag loading in the catalyst system may be insufficient to generate detectable crystalline Ag domains, causing the weak Ag diffraction intensity to be overshadowed by the stronger TiO_2 reflections. As a result, other characteristic Ag peaks, such as Ag (200) at 44.3° and Ag (220) at 64.4°, were also not observed [60].

For the samples without P25 including TSAP (d) and TSA (e), several characteristic rutile peaks, including R (110) at 27.4°, R (101) at 36.1°, R (111) at 41.2°, and R (220) at 56.6°, were absent or significantly reduced in intensity, indicating that the rutile phase was either substantially reduced or below the detection limit of XRD. In addition, the main anatase peak A (101) at approximately 25.3° exhibited lower intensity compared to the P25-containing samples. Other anatase peaks A (004) at 37.5°, A (211) at 55°, A (204) at 62.7° appeared broader and partially merged, resulting in wider and less defined diffraction peaks. Such peak broadening generally suggests lower crystallinity, smaller crystallite size, and/or increased lattice disorder in the TiO_2 structure. This behaviour may be attributed to the sol-gel synthesis conditions such as calcination temperature and the presence of amorphous SiO_2 matrix, which may reduce crystallite development of TiO_2 during calcination [73].

For the samples containing P25 including TSAP25P (b) and TSAP25 (c), the XRD patterns exhibited the characteristic peaks of both anatase and rutile TiO_2 phases. Compared with TSA and TSAP, the samples with P25 in their systems showed sharper and more intense diffraction peaks, particularly A (101) at 25.3°, A (004) at 37.5°, A (200) at 48°, and A (204) at 62.7°, indicating improved crystallinity of TiO_2. Furthermore, rutile peaks such as R (110) at 27.4°, R (101) at 36.1°, R (111) at 41.2°, and R (220) at 56.6° were clearly detected, although their intensities remained lower than those of anatase peaks. This observation is consistent with the intrinsic mixed-phase composition of commercial P25, which contains both anatase and rutile phases. Therefore, incorporating P25 into the system increased the rutile contribution and improved the overall crystallinity of the TiO_2-based material [73].

Although the XRD analysis was performed on powder samples, the results revealed the intrinsic phase composition and crystallinity of the catalyst material after calcination. These findings do not confirm that the coatings possess the same phase composition and crystallinity as the powders; however, they support the photocatalytic behaviours of the coatings, in which samples containing P25 could have higher activity than those without P25. In addition, the role of PEG in coating samples may differ from its role in powder samples. Although PEG did not significantly affect the crystalline structure of the powders, its decomposition during calcination may promote pore formation and increase surface roughness in the coatings, thereby enhancing photocatalytic activity through an increase in effective surface area.

3.1.5 The result of the coating adherence on substrate

a) Protocol 1: TiO_2-SiO_2-Ag (TSA)

The Figure 26 shows five coating samples prepared from the same synthesis batch. Overall, the coatings on the steel substrates appear relatively homogeneous. However, despite identical substrate preparation procedures, slight variations in coating uniformity were observed among the samples.

Out of the five samples, only one exhibited fully uniform coverage, while the remaining four showed minor inhomogeneities. These non-uniform regions are highlighted by red frames.

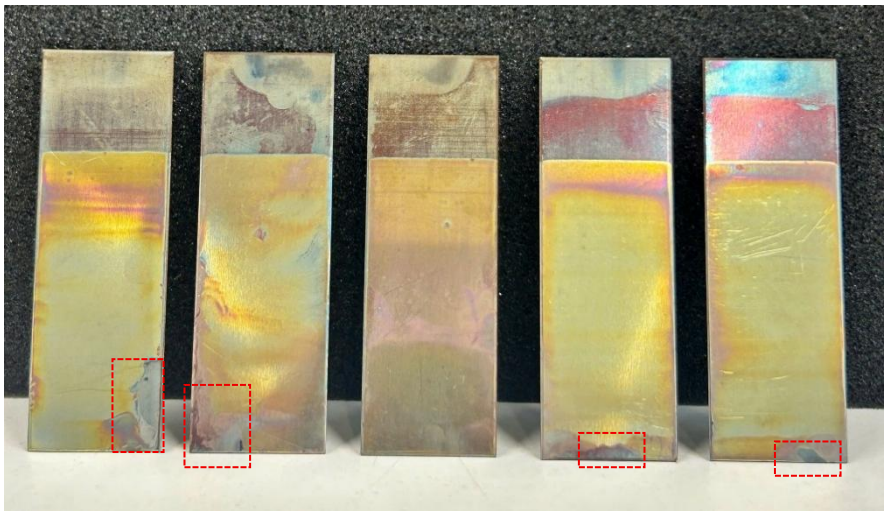

Figure 26. Homogeneity of TSA coating surface

The Figure 27 below shows the coating surface before and after the adherence test. After removing the tape, the edges of the cuts remained smooth, and none of the lattice squares were detached. According to ASTM D3359, this corresponds to a classification of 4B-5B, indicating excellent coating adhesion.

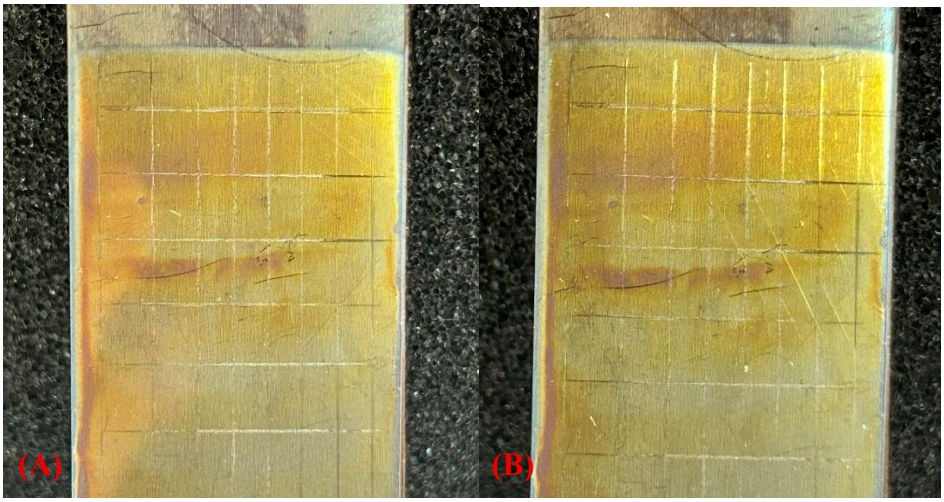

Figure 27. Tape test of TSA coating (A) before, (B) after

b) Protocol 2: TiO_2-SiO_2-Ag-P25 (TSAP25)

The Figure 28 presents five coating samples produced from the same synthesis batch. In general, the coatings on the steel substrates appear uniform, but slight differences in coating uniformity can be observed between samples. Among the five samples, two showed completely uniform coverage, while the other three exhibited minor inhomogeneities.

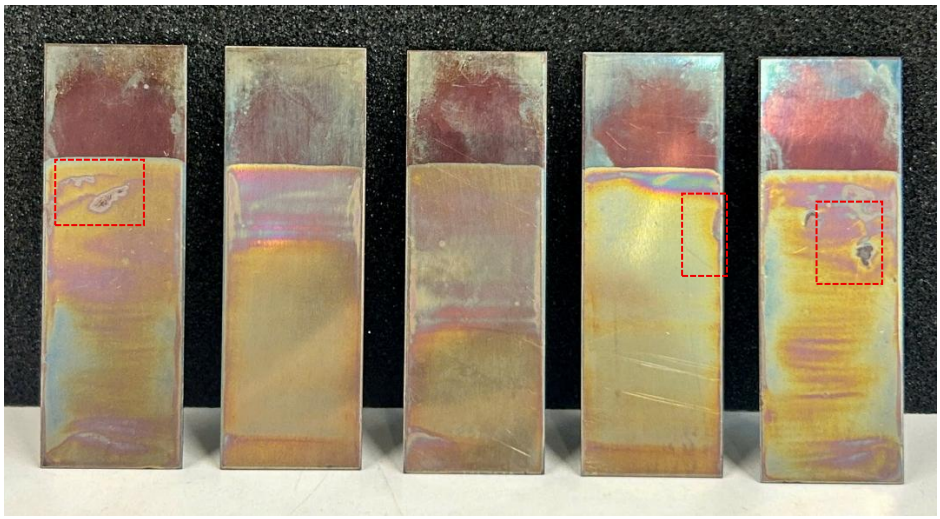

Figure 28. Homogeneity of TSAP25 coating surface

The Figure 29 below shows the coating surface before and after the adherence test. After the tape test, the edges of the cuts remained smooth, and none of the lattice squares were detached. According to ASTM D3359, this corresponds to a classification of 4B-5B, indicating excellent coating adhesion.

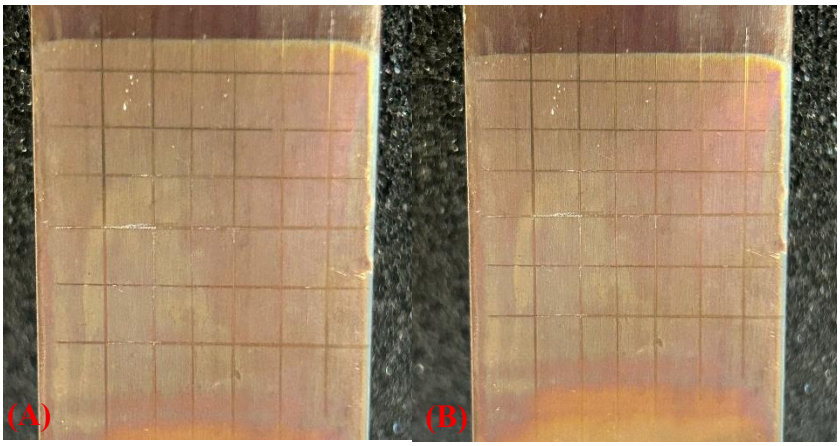

Figure 29. Tape test of TSAP25 coating (A) before, (B) after

c) Protocol 3: TiO_2-SiO_2-Ag-P25-PEG (TSAP25P)

The Figure 30 presents five coating samples produced from the same synthesis batch. In general, the coatings on the steel substrates appear uniform, but slight differences in coating uniformity can be observed between samples. Among the five samples, two showed completely uniform coverage, while the other three exhibited minor inhomogeneities.

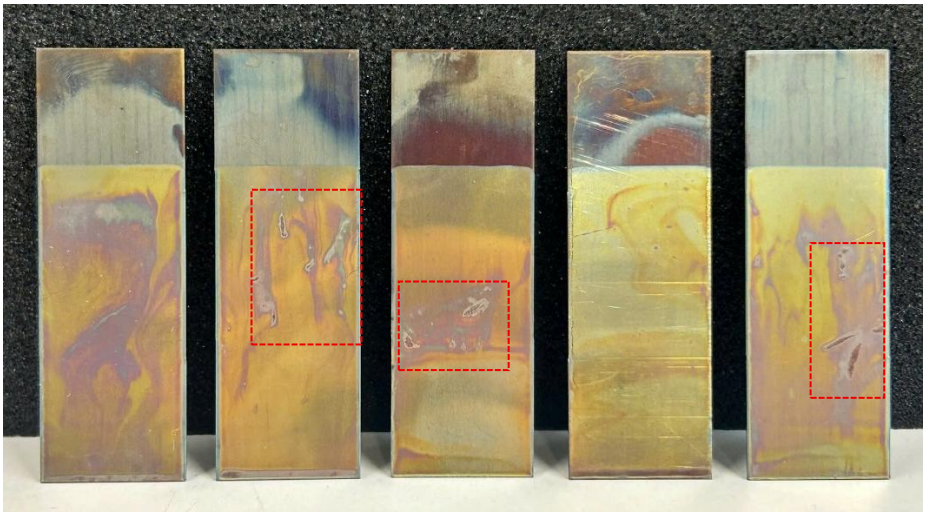

Figure 30. Homogeneity of TSAP25P coating surface

After the tape test, the Figure 31 below shows that the edges of the cuts remained smooth, and none of the lattice squares were detached. According to ASTM D3359, this corresponds to a classification of 4B-5B, indicating excellent coating adhesion.

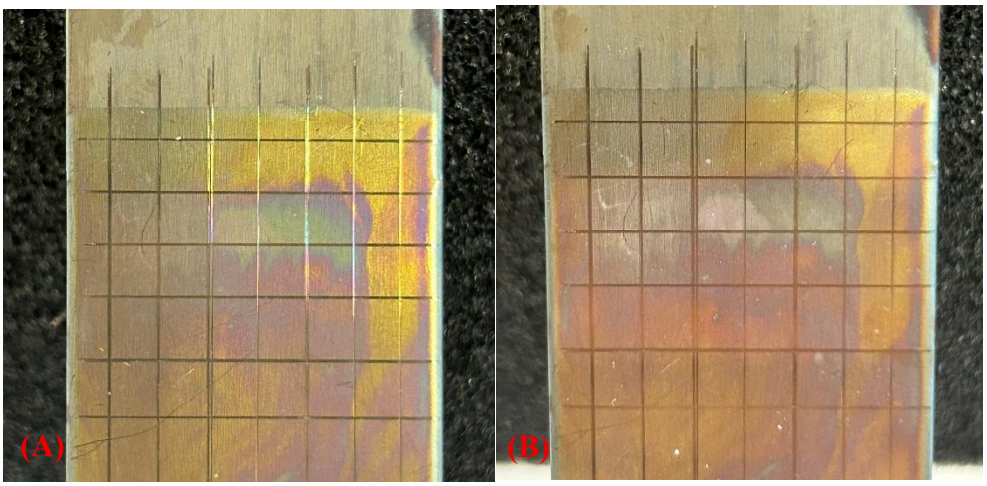

Figure 31. Tape test of TSAP25P coating (A) before, (B) after

d) Protocol 4: TiO_2-SiO_2-Ag-PEG (TSAP)

The Figure 32 presents five coating samples produced from the same synthesis batch. In general, the coatings on the steel substrates appear uniform, but slight differences in coating uniformity can be observed between samples. Among the five samples, two showed completely uniform coverage, while the other three exhibited minor inhomogeneities.

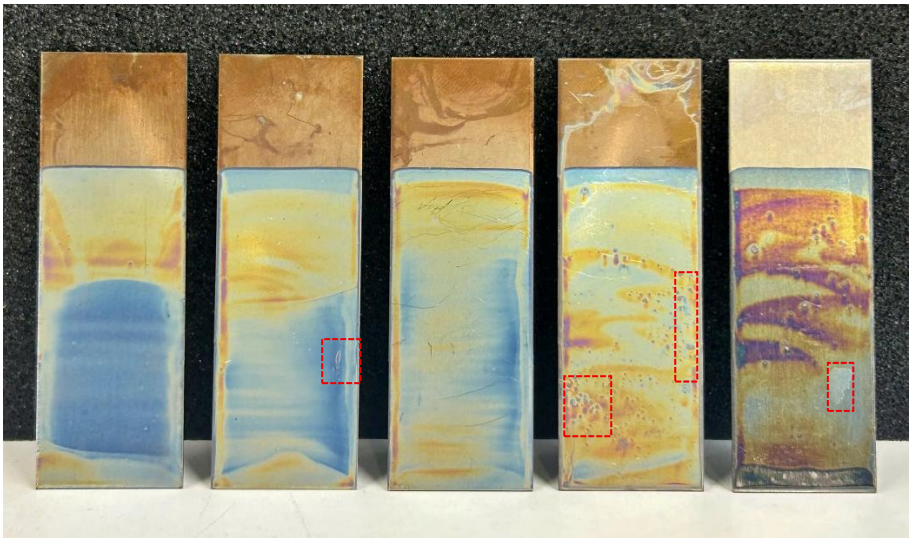

Figure 32. Homogeneity of TSAP coating surface

After the tape test, the Figure 33 shows that the edges of the cuts remained smooth, and none of the lattice squares were detached. According to ASTM D3359, this corresponds to a classification of 4B-5B, indicating excellent coating adhesion.

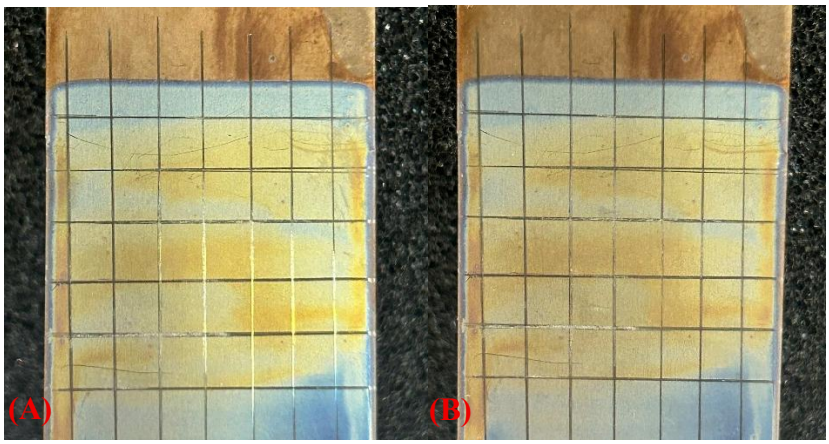

Figure 33. Tape test of TSAP coating (A) before, (B) after

e) Protocol 4: P25-4HBA (P25)

The Figure 34 presents five coating samples produced from the same synthesis batch. Overall, the coatings on the steel substrates appear uniform; however, slight variations in coating homogeneity can still be observed among the samples. Four of the five samples exhibited completely uniform coverage, while only one showed a minor inhomogeneity.

Compared to protocols 1–4, where only 1–2 out of 5 samples achieved complete surface homogeneity, protocol 5 resulted in 4 out of 5 samples with fully uniform coatings. This suggests that the solution used in protocol 5 provides greater stability and is more effective for producing homogeneous coatings on steel substrates.

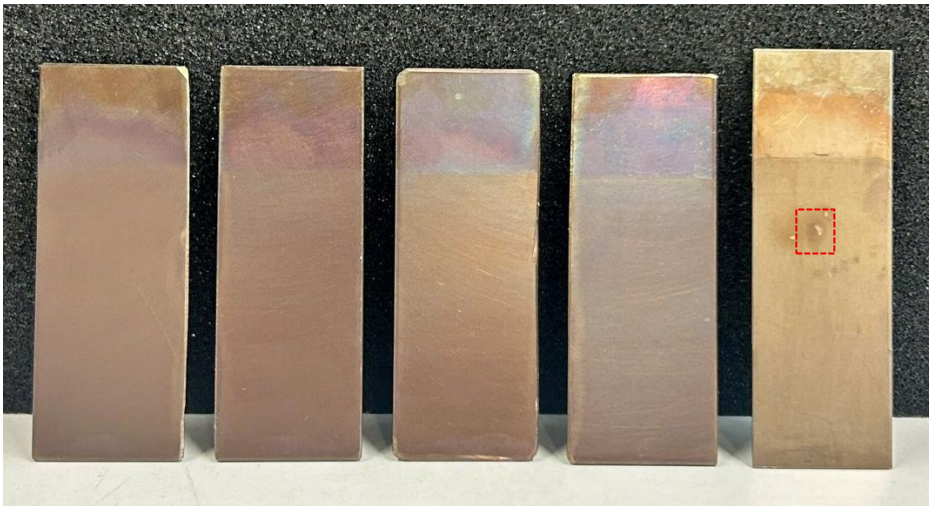

Figure 34. Homogeneity of P25 coating surface

After the tape test, the Figure 35 shows that the edges of the cuts remained smooth, and none of the lattice squares were detached. According to ASTM D3359, this corresponds to a classification of 4B-5B, indicating excellent coating adhesion.

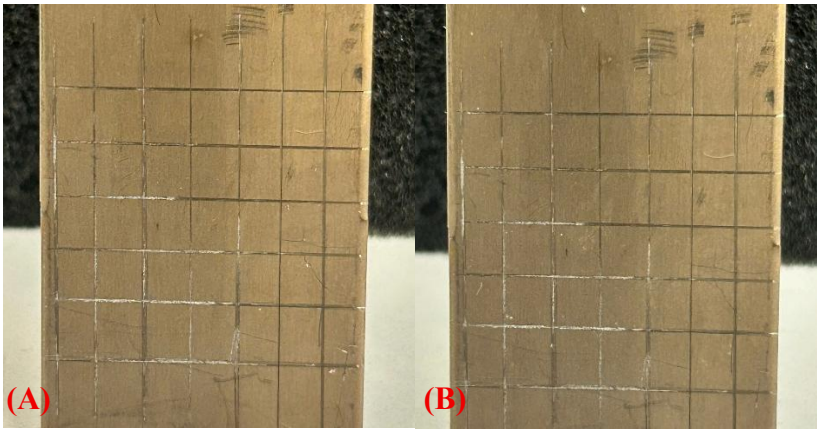

Figure 35. Tape test of P25 coating (A) before, (B) after

The tape test results (ASTM D3359) showed that all five coatings achieved a maximum adhesion rating of 4B-5B, independent of the synthesis route (sol–gel or colloid method). This suggests that the adhesion performance is primarily governed by the interfacial bonding between TiO_2 and the steel substrate, which is significantly enhanced after calcination [74].

3.1.6 Results of OTC degradation with photocatalytic coatings by UV-vis and TOC methods

a) Protocol 1: TiO_2-SiO_2-Ag (TSA)

The photocatalytic degradation of oxytetracycline (OTC) was evaluated using both UV–Vis spectroscopy and total organic carbon (TOC) analysis. The UV–Vis spectra show that the main absorption peak of OTC occurs at 355 nm [75] which would be used for the comparisons of activity among 5 different catalysts.

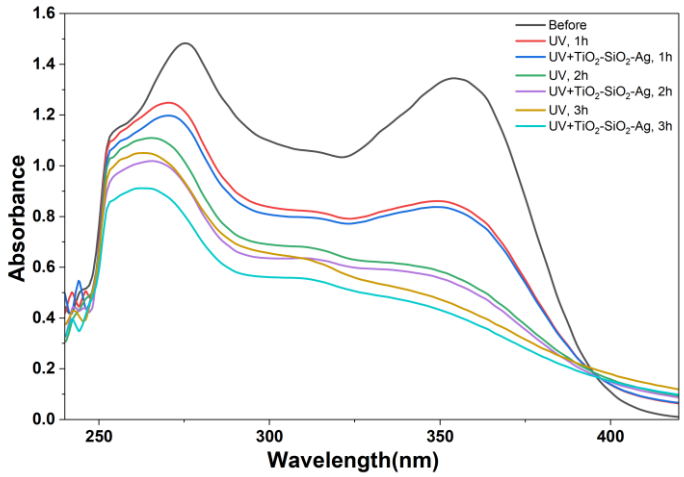

Figure 36. UV-vis spectra of OTC degradation with TSA coating

The Figure 36 shows that initially the absorbance at wavelength of 355 nm was 1.344. After 3 hours of reaction under UVC irradiation, a significant decrease in absorbance was observed for both the UVC-only and photocatalytic systems, indicating the progressive degradation of OTC.

Quantitatively, the absorbance decreased from 1.344 to 0.448 under UVC irradiation alone and to 0.408 in the presence of the TSA coating after 3 hours. This confirms that the photocatalyst slightly enhances degradation efficiency compared to direct photolysis. The reduction in absorbance corresponds to the breakdown of the characteristic chromophoric structures of OTC, particularly its conjugated ring system, which is consistent with reported photocatalytic degradation pathways of tetracycline antibiotics [75].

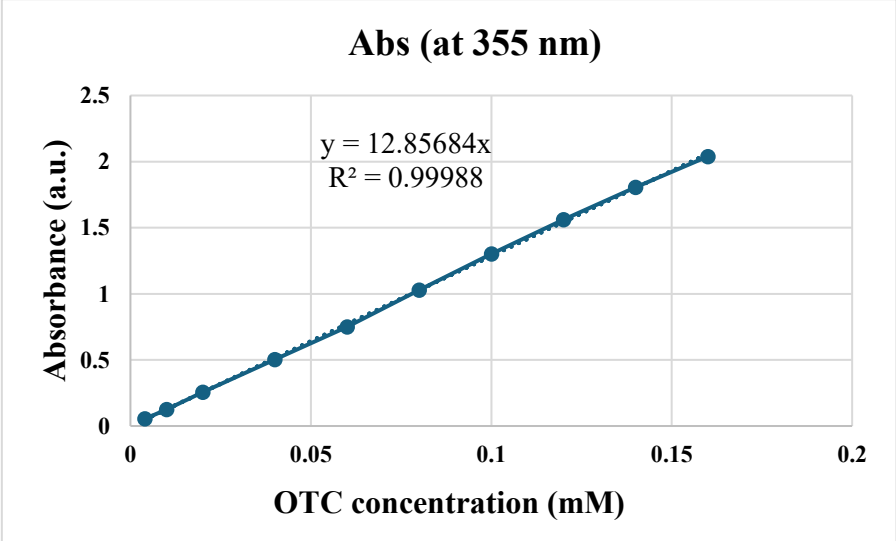

Figure 37. Calibration curve of OTC

To accurately determine the amount of OTC degraded, the absorbance values can be converted into concentrations using the calibration (standard) curve obtained from UV–Vis analysis of OTC. This curve would be used for the transformation of UV-Vis in results of next protocols as well.

The photocatalytic efficiency and catalyst contribution were calculated using the following equations:

- E (efficiency) = $\frac{C0-C}{C0} \times 100$ (%) where C_0 is the initial concentration and C is the final concentration
- C (catalyst contribution) = $E_{(UVC+catalyst)} - E_{(UVC)}$ (%) where $E_{(UVC + catalyst)}$ and $E_{(UVC)}$ represent the removal efficiencies obtained with and without the catalyst, respectively.

These equations were used to calculate the OTC and TOC removal efficiencies for all photocatalytic degradation experiments.

Table 13. OTC degradation efficiency in the TSA system

	UV-vis (355)					
Sample ID	**UV intensity (mW/cm^2)**	**OTC (mM) Before**	**OTC (mM) 3h**	**Degraded OTC (mM)**	**Efficiency (%)**	**Catalyst contribution (%)**
UVC only	3.85	0.1045	0.0351	0.0695	66.5	0
UVC+TSA	3.85	0.1045	0.032	0.0726	69.47	2.97

To clarify, the Table 13 illustrates the decrease in OTC concentration over 3 hours under UVC alone and in the presence of the catalyst. The efficiency of OTC degradation without and with catalyst is 66.5% and 69.47%, respectively, corresponding to an efficiency improvement of about 2.97% from catalyst.

Table 14. TOC degradation efficiency in the TSA system

	TOC				
Sample ID	**TOC First (mgC/L)**	**TOC Final (mgC/L)**	**Degraded TOC (mgC/L)**	**Efficiency (%)**	**Catalyst contribution (%)**
UVC only	24.01	22.17	1.84	7.66	0
UVC+TSA	24.01	20.97	3.04	12.66	5

The Table 14 shows that the initial TOC was 24.01 mgC/L. After 3 hours of UVC irradiation, the TOC decreased to 22.17 mgC/L (7.66%) for UVC alone and to 20.97 mgC/L (12.66%) for the system with TSA. The addition of the catalyst to the photolysis process enhanced mineralization by about 1.2 mgC/L, corresponding to an efficiency improvement of approximately 5%.

b) Protocol 2: TiO_2-SiO_2-Ag-P25 (TSAP25)

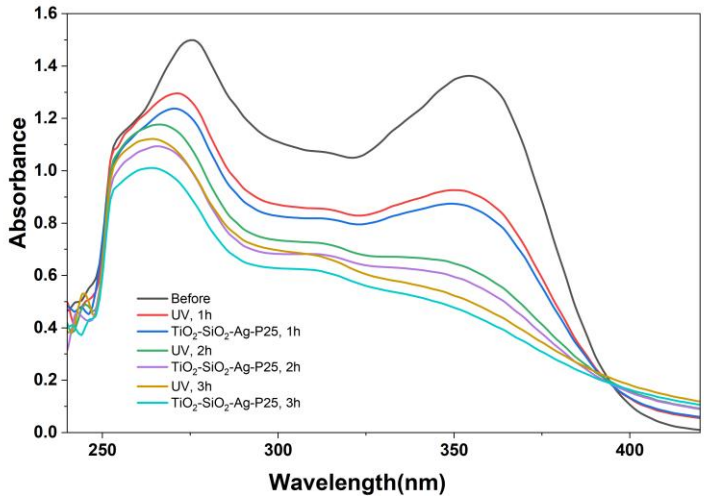

Figure 38. UV-vis spectra of OTC degradation with TSAP25 coating

The Figure 38 showed that the initial absorbance of OTC at 355 nm was 1.362, which decreased after 3 hours of UVC irradiation, indicating the degradation of OTC.

Under UVC irradiation alone, the absorbance decreased to 0.498, whereas in the presence of TSAP25, it further decreased to 0.451. This difference suggests that TSAP25 provides slight enhancement in photocatalytic activity compared to direct photolysis.

Table 15. OTC degradation efficiency in the TSAP25 system

	UV-vis (355)					
Sample ID	**UV intensity (mW/cm^2)**	**OTC (mM) Before**	**OTC (mM) 3h**	**Degraded OTC (mM)**	**Efficiency (%)**	**Catalyst contribution (%)**
UVC only	3.97	0.1059	0.0389	0.067	63.26	0
UVC+TSAP25	3.97	0.1059	0.0353	0.0707	66.76	3.5

The Table 15 illustrates the decrease in OTC concentration over 3 hours under UVC irradiation alone and in the presence of the catalyst. The efficiency of OTC degradation without and with catalyst is 63.26% and 66.76%, respectively, corresponding to an efficiency improvement of about 3.5% from catalyst.

Table 16. TOC degradation efficiency in the TSAP25 system

	TOC				
Sample ID	**TOC First (mgC/L)**	**TOC Final (mgC/L)**	**Degraded TOC (mgC/L)**	**Efficiency (%)**	**Catalyst contribution (%)**
UVC only	24.33	22.41	1.92	7.9	0
UVC+TSAP25	24.33	21.13	3.2	13.15	5.25

The TOC results from the Table 16 reveal that after 3 hours of UVC irradiation, the TOC decreased from 24.33 to 22.41 mgC/L (7.9%) for UVC alone and to 21.13 mgC/L (13.15%) for

the system with TSAP25. The addition of the catalyst to the photolysis process enhanced mineralization by about 1.28 mgC/L, corresponding to an efficiency improvement of approximately 5.25%.

The result showed that adding P25 enhances the photocatalytic activity of the coating due to its mixed anatase–rutile phase composition, which promotes efficient charge separation. The heterojunction between anatase and rutile reduces electron–hole recombination, allowing more photogenerated charge carriers to participate in redox reactions. Additionally, P25 has a high surface area and strong UVC absorption, providing more active sites for photocatalytic reactions and improving the generation of reactive oxygen species (•OH and $O_2^{\bullet -}$), which accelerate the degradation of organic pollutants [60].

c) Protocol 3: TiO_2-SiO_2-Ag-P25-PEG (TSAP25P)

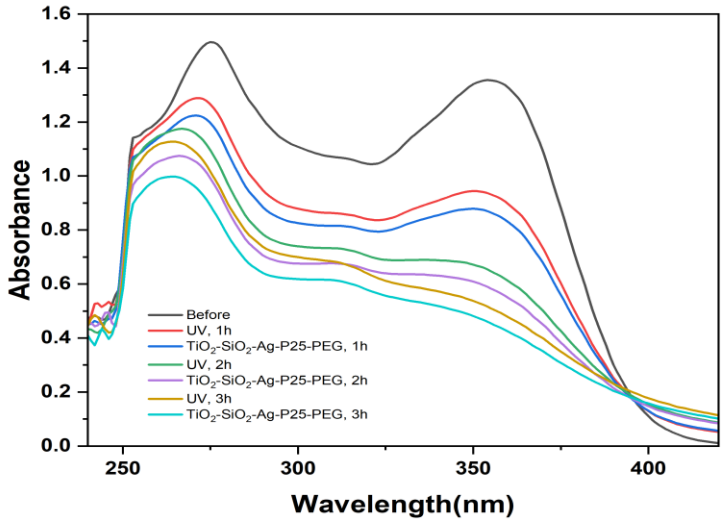

Figure 39. UV-vis spectra of OTC degradation with TSAP25P coating

The Figure 39 showed that the initial absorbance of OTC at 355 nm was 1.354, which decreased after 3 hours of UVC irradiation, indicating the degradation of OTC.

Under UVC irradiation alone, the absorbance decreased to 0.51, whereas in the presence of TSAP25P, it further decreased to 0.455. This difference suggests that TSAP25P also provides improvement in photocatalytic activity compared to direct photolysis.

Table 17. OTC degradation efficiency in the TSAP25P system

	UV-vis (355)					
Sample ID	**UV intensity (mW/cm^2)**	**OTC (mM) Before**	**OTC (mM) 3h**	**Degraded OTC (mM)**	**Efficiency (%)**	**Catalyst contribution (%)**
UVC only	3.94	0.1053	0.0399	0.0655	62.2	0
UVC+TSAP25P	3.94	0.1053	0.0356	0.0697	66.19	3.99

The Table 17 illustrates the decrease in OTC concentration over 3 hours under UVC irradiation alone and in the presence of the catalyst. The efficiency of OTC degradation without and with catalyst is 62.2% and 66.19%, respectively, corresponding to an efficiency improvement of about 3.99% from catalyst.

Table 18. TOC degradation efficiency in the TSAP25P system

	TOC				
Sample ID	**TOC First (mgC/L)**	**TOC Final (mgC/L)**	**Degraded TOC (mgC/L)**	**Efficiency (%)**	**Catalyst contribution (%)**
UVC only	24.01	22.17	1.84	7.66	0
UVC+TSAP25P	24.01	20.53	3.48	14.5	6.83

Similarly, the TOC results from the Table 18 reveal that after 3 hours of UVC irradiation, the TOC decreased from 24.01 to 22.17 mgC/L (7.66%) for UVC alone and to 20.53 mgC/L (14.5%) for the system with TSAP25P. The addition of the catalyst to the photolysis process enhanced mineralization by about 1.64 mgC/L, corresponding to an efficiency improvement of approximately 6.83%.

Although this improvement remains relatively modest, it is higher than that observed for the TSAP25 system without PEG, suggesting that the incorporation of polyethylene glycol (PEG) contributes positively to the photocatalytic performance. PEG is known to act as a structure-directing agent, improving the porosity and surface area of the coating, thereby enhancing the adsorption of OTC molecules and facilitating better interaction between pollutants and reactive sites [76].

d) Protocol 4: TiO_2-SiO_2-Ag-PEG (TSAP)

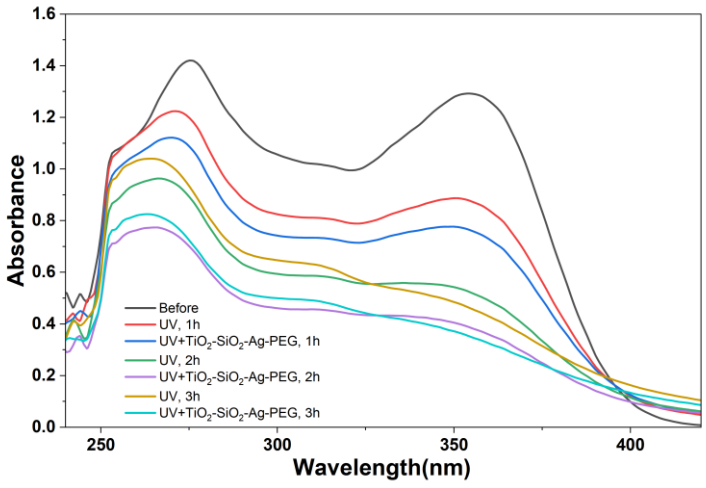

Figure 40. UV-vis spectra of OTC degradation with TSAP coating

The Figure 40 showed that the initial absorbance of OTC at 355 nm was 1.292, which decreased after 3 hours of UVC irradiation, indicating the degradation of OTC.

Under UVC irradiation alone, the absorbance decreased to 0.459, whereas in the presence of TSAP, it further decreased to 0.349. This difference suggests that TSAP also provides a significant improvement in photocatalytic activity compared to direct photolysis.

Table 19. OTC degradation efficiency in the TSAP system

	UV-vis (355)					
Sample ID	**UV intensity (mW/cm^2)**	**OTC (mM) Before**	**OTC (mM) 3h**	**Degraded OTC (mM)**	**Efficiency (%)**	**Catalyst contribution (%)**
UVC only	3.88	0.1005	0.0359	0.0646	64.28	0
UVC+TSAP	3.88	0.1005	0.0274	0.0731	72.74	8.46

The Table 19 illustrates the decrease in OTC concentration over 3 hours under UVC irradiation alone and in the presence of the catalyst. The efficiency of OTC degradation without and with catalyst is 64.28% and 72.74%, respectively, corresponding to an efficiency improvement of about 8.46% from catalyst.

Table 20. TOC degradation efficiency in the TSAP system

	TOC				
Sample ID	**TOC First (mgC/L)**	**TOC Final (mgC/L)**	**Degraded TOC (mgC/L)**	**Efficiency (%)**	**Catalyst contribution (%)**
UVC only	23.17	21.82	1.35	5.83	0
UVC+TSAP	23.17	19.53	3.64	15.71	9.88

The TOC results from the Table 20 show that after 3 hours of UVC irradiation, the TOC decreased from 23.17 to 21.82 mgC/L (5.83%) for UVC alone and to 19.53 mgC/L (15.71%) for the system with TSAP. The addition of the catalyst to the photolysis process enhanced mineralization by about 2.29 mgC/L, corresponding to an efficiency improvement of approximately 9.88%.

The result shows that adding only PEG into catalyst can make a better photocatalytic activity than adding both PEG and P25. This is mainly because PEG acts as a structure-directing and pore-forming agent, leading to improved dispersion and increased surface area, which enhances photocatalytic performance [76]. In contrast, with a PEG-P25-based coating, the interaction between P25 particles in the gel system during calcination may limit the presence of pores generated from PEG. Additionally, P25 particles tend to form aggregates within the coating, which can reduce effective surface area and hinder mass transfer of reactants [77].

e) Protocol 5: P25-4HBA (P25)

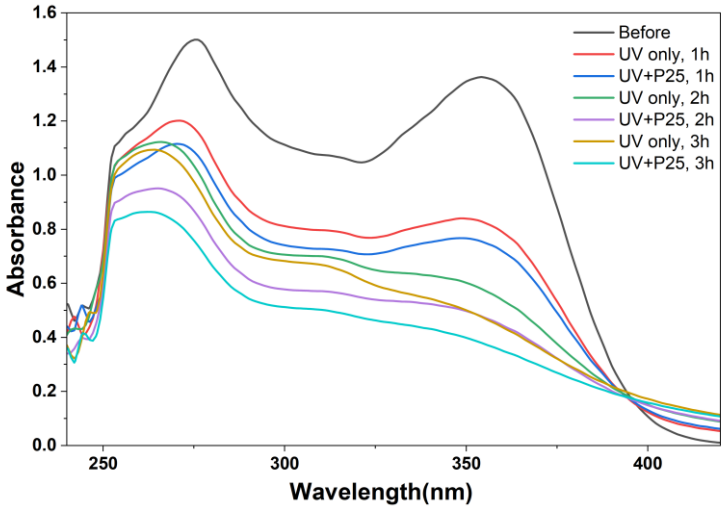

Figure 41. UV-vis spectra of OTC degradation with P25 coating

The Figure 41 showed that the initial absorbance of OTC at 355 nm was 1.361, which decreased after 3 hours of UVC irradiation, indicating the degradation of OTC.

Under UVC irradiation alone, the absorbance decreased to 0.472 while in the presence of P25, it further decreased to 0.376. This difference suggests that P25 improves photocatalytic activity effectively compared to direct photolysis.

Table 21. OTC degradation efficiency in the P25 system

	UV-vis (355)					
Sample ID	**UV intensity (mW/cm^2)**	**OTC (mM) Before**	**OTC (mM) 3h**	**Degraded OTC (mM)**	**Efficiency (%)**	**Catalyst contribution (%)**
UVC only	4.05	0.1059	0.0369	0.069	65.15	0
UVC+P25	4.05	0.1059	0.0295	0.0764	72.14	7

The Table 21 illustrates the decrease in OTC concentration over 3 hours under UVC irradiation alone and in the presence of the catalyst. The efficiency of OTC degradation without and with catalyst is 65.15% and 72.14%, respectively, corresponding to an efficiency improvement of about 7% from catalyst.

Table 22. TOC degradation efficiency in the P25 system

	TOC				
Sample ID	**TOC First (mgC/L)**	**TOC Final (mgC/L)**	**Degraded TOC (mgC/L)**	**Efficiency (%)**	**Catalyst contribution (%)**
UVC only	23.98	22.34	1.64	6.84	0
UVC+P25	23.98	20.35	3.63	15.14	8.3

The TOC results from the Table 22 show that after 3 hours of UVC irradiation, the TOC decreased from 23.98 to 22.34 mgC/L (6.84%) for UVC alone and to 20.35 mgC/L (15.14%) for the system with P25. The addition of the catalyst to the photolysis process enhanced mineralization by about 1.99 mgC/L, corresponding to an activity improvement of approximately 8.3%.

The UV-Vis and TOC analysis reveals that the intrinsic photocatalytic properties of P25 powder were effectively preserved in the coating form. Even without doping or PEG, the immobilized P25 nanoparticles remained well exhibited significant photoactivity, contributing to enhanced degradation performance.

Table 23. Summary of degradation efficiency and catalyst contribution

Catalytic coating	Method	Catalyst contribution in degradation efficiency of OTC (%)	Catalyst contribution in degradation efficiency of TOC (%)
TSA	Sol-gel	2.97	5
TSAP25		3.5	5.26
TSAP25P		3.99	6.83
TSAP		8.46	9.88
P25	Colloid	7	8.3

The Table 23 summarizes the contribution of different catalysts to the degradation of oxytetracycline (OTC) and total organic carbon (TOC). It is observed that, for most systems, the catalyst contribution to TOC removal is higher than that for OTC degradation. This trend is well aligned with photocatalysis literature, where direct photolysis under UVC light can already effectively degrade OTC molecules, while photocatalysts mainly enhance the subsequent mineralization of intermediate products [78].

From the Table 23, the TSAP exhibits the highest catalytic activity contribution, while P25 shows the second-highest catalytic activity contribution, with only a minor difference between these two samples. However, as shown in Table 11 and 12, the coating mass of TSAP on the substrate (around 0.938 mg) is approximately 2.2 times higher than that of P25 (around 0.426 mg). Therefore, P25 coating is more efficient per milligram of material than TSAP coating, it means:

- A specific activity of OTC and TOC degradation of TSAP coating estimated at about 9.02 %/mg and 10.53 %/mg, respectively.
- A specific activity of OTC and TOC degradation of P25 coating estimated at roughly 16.43 %/mg and 19.48 %/mg, respectively.

Therefore, P25 coating was selected as the most suitable catalyst due to its high activity, good adherence and economic viability.

3.2 Results of the Optimization of Photocatalytic Coatings for Enhanced OTC Degradation

3.2.1 Result of the effect of TiO_2 powder types on the particle deposition

Under identical synthesis conditions in the protocol 5, two suspensions: P25-4HBA and TiO_2-4-HBA were prepared. Both samples were left undisturbed for 2 days to evaluate the extent of particle sedimentation. The results are presented in the Figure 42 and Table 24 below.

Figure 42. Sedimentation behaviour of different TiO_2 powders: left-P25, right-pure TiO_2

Table 24. Deposition of colloidal solution

	Initial solid mass in solution (g)	Solid mass settles down after 2 days (g)	Deposition (%)
P25-4-HBA	0.9	0.015	1.66
TiO_2-4-HBA	0.9	0.84	93.33

The results from the Table 24 indicate a significant difference in suspension stability between the two samples. In the case of P25-4-HBA, only 1.66% of the particles settled after 2 days, demonstrating excellent dispersion stability. In contrast, the TiO_2-4-HBA sample showed substantial sedimentation, with 93.33% of particles settling over the same period.

This behaviour can be attributed to the physicochemical properties of P25. This P25 is a commercially available TiO_2 nano-powder (primarily composed of anatase and rutile phases) with a small particle size and high surface area, which enhances colloidal stability and prevents rapid aggregation and sedimentation. As a result, particles remain well-dispersed in the solution.

This observation is consistent with a patent mentioned before [63], which describe colloidal solutions derived from functionalized nano-powders as homogeneous dispersions of particles within specific size ranges:

- Broad range: 2–1000 nm
- Preferred range: 2–500 nm

- Optimal range: 2–200 nm

In fact, the P25-4-HBA solution was still stable during several weeks without a lot of sedimentations.

3.2.2 Results of the effect of substrate surface nature on colloidal coating loading

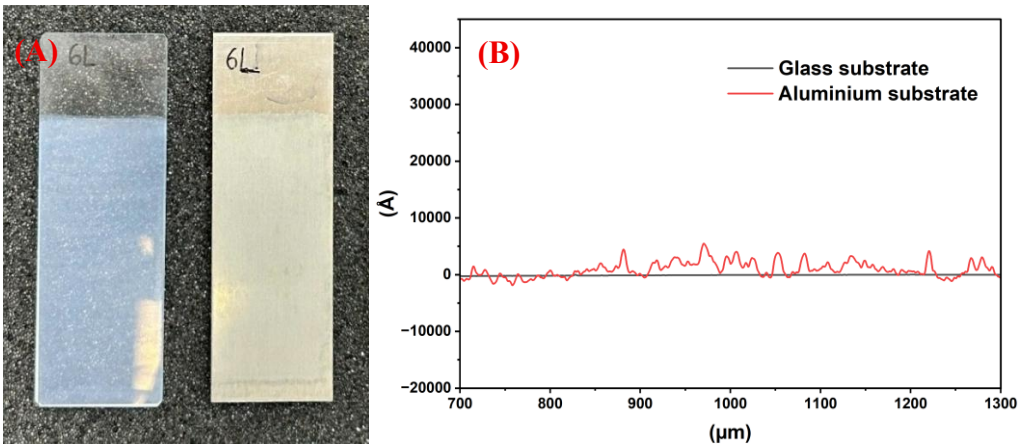

Figure 43. (A) Reference substrates: glass and aluminium, (B) Roughness level

Figure 43 (B) shows the surface characteristics of the glass and aluminium substrates obtained using profilometer analysis. The glass substrate exhibited a smooth and relatively flat surface profile, whereas the aluminium substrate showed a noticeably rougher surface morphology.

Table 25. The colloid based coating mass on Al substrate

6 layers of colloid-based coating on Al substrate		
Repeated	**Before coating (g)**	**After coating (g)**
1	3.77294	3.77338
2	3.77295	3.77338
3	3.77293	3.77334
4	3.77298	3.77343
5	3.77295	3.77335
Average	3.77295	3.773376
Coating mass (mg)	**0.426**	

Table 26. The colloid based coating mass on glass substrate

6 layers of colloid-based coating on glass substrate		
Repeated	**Before coating (g)**	**After coating (g)**
1	5.18594	5.18668
2	5.18604	5.18669
3	5.18606	5.1867
4	5.18595	5.18672
5	5.18602	5.18672
Average	5.186002	5.186702
Coating mass (mg)	**0.7**	

After direct measurement of coating mass, the results from the Table 25 and 26 indicate that surface roughness alone does not directly determine coating loading in the colloidal system. Although higher roughness is commonly expected to enhance coating deposition through increased surface area and mechanical interlocking, this trend was not observed in the present study. Despite exhibiting a higher roughness level, the aluminium substrate showed lower coating loading (0.426 mg) than glass (0.7 mg), suggesting that other interfacial factors play a more dominant role in governing colloidal deposition behaviour.

This observation is consistent with previously reported studies on patterned wettability substrates [68], where colloidal deposition was found to depend strongly on the ability of the substrate surface to sustain a stable liquid film during dip-coating withdrawal. In colloidal systems, deposition behaviour is influenced not only by surface morphology, but also by surface wettability, surface energy, and electrostatic interactions between the substrate and colloidal particles.

Hydrophilic surfaces with high surface energy promote effective liquid spreading and film retention, resulting in the formation of a more continuous and stable wet layer during withdrawal. This enhances the amount of colloidal suspension retained on the substrate prior to solvent evaporation, thereby increasing nanoparticle deposition and coating loading. In contrast, insufficient wetting stability may induce partial de-wetting, reducing liquid retention and lowering deposition efficiency. Electrostatic interactions may further influence nanoparticle adhesion and early-stage deposition. The attractive electrostatic interactions can enhance particle adsorption, contact-line pinning, and nanoparticle retention during solvent evaporation

Therefore, the observed differences in coating loading are more reasonably attributed to variations in surface wettability, surface chemistry, and electrostatic affinity rather than surface roughness alone. In colloidal dip-coating systems, these interfacial properties play a dominant role in controlling liquid film stability and nanoparticle retention during deposition.

In the case of stainless-steel substrates, although their surfaces may exhibit relatively high roughness, achieving higher coating loading in colloidal synthesis systems is expected to depend more strongly on surface chemistry and wettability than on roughness alone. Therefore, surface treatment prior to dip-coating becomes particularly important, as it can significantly influence interfacial interactions, wetting behaviour, and ultimately coating deposition efficiency.

3.2.3 Results of the optimization of the number of coating layers

a) OTC degradation results

Table 27. Degraded OTC concentration with different coating layers

	UV-vis (355)					
Sample ID	**UV intensity (mW/cm^2)**	**OTC (mM) Before**	**OTC (mM) 3h**	**Degraded OTC (mM)**	**Efficiency (%)**	**Catalyst contribution (%)**
UV only	*4.05*	*0.1048*	*0.0366*	*0.0682*	*65.07*	*0*
UV+6 layers	4.05	0.1048	0.0303	0.0745	71.08	6.01
UV+9 layers	4.05	0.1048	0.0249	0.08	76.34	11.27
UV+12 layers	4.05	0.1048	0.022	0.0828	79	13.93
UV only	*4*	*0.1057*	*0.0347*	*0.071*	*67.17*	*0*
UV+15 layers	4	0.1057	0.0187	0.087	82.3	15.13
UV+18 layers	4	0.1057	0.0162	0.0895	84.67	17.5
UV+21 layers	4	0.1057	0.0185	0.0872	82.49	15.32

The degradation efficiencies of OTC after 3 hours for P25 coatings with 6, 9, 12, 15, 18, and 21 layers are presented in Table 27. A clear trend is observed: the degradation efficiency increases as the number of coating layers increases from 6 to 18 layers. This indicates that increasing the TiO_2 film thickness enhances photocatalytic activity up to an optimal point. The improvement can be attributed to the higher amount of active material and increased availability of photocatalytic sites, leading to greater generation of reactive oxygen species (ROS) under UVC irradiation [79].

However, when the number of layers is further increased to 21, the degradation efficiency decreases. This suggests that excessive film thickness negatively affects photocatalytic performance. A likely explanation is that thicker coatings reduce light penetration and increase charge carrier recombination within the TiO_2 layer. Additionally, overly thick films may limit mass transfer of reactants to active sites [79], [80]. Therefore, there exists an optimal thickness (in this case, 18 layers) that balances light absorption, charge transport, and surface reaction.

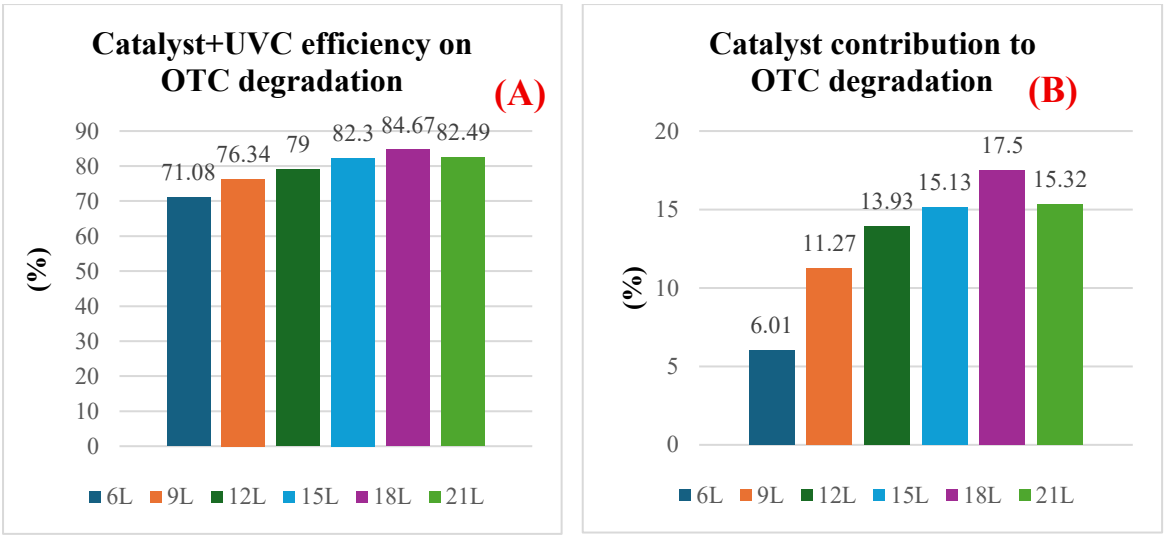

Figure 44. OTC degradation under different coating layers (A) Catalyst and UVC efficiency, (B) Catalyst contribution

Figure 44 (A) shows the total degradation efficiency under combined UVC irradiation and TiO_2 catalysis, while Figure 44 (B) represents the contribution of the catalyst. The sample with 18 layers exhibits the highest activity in both cases, confirming it as the optimal configuration.

It is also evident that UVC irradiation plays a dominant role in OTC degradation. For instance, in the 18-layer sample, the total degradation efficiency reaches 84.67%, while the additional contribution attributed to the catalyst is approximately 17.5%. This indicates that direct photolysis of OTC under UVC is significant, the presence of TiO_2 can enhance humbly degradation through photocatalytic mechanisms. Therefore, the catalyst does not degrade the OTC significantly but as a synergistic component that improves overall degradation efficiency.

b) TOC degradation results

Table 28. Degraded TOC concentration with different coating layers

	TOC				
Sample ID	**TOC First (mgC/L)**	**TOC Final (mgC/L)**	**Degraded TOC (mgC/L)**	**Efficiency (%)**	**Catalyst contribution (%)**
UV only	*24.15*	*22.48*	*1.67*	*6.92*	*0*
UV+6 layers	24.15	19.96	4.19	17.35	10.43
UV+9 layers	24.15	18.82	5.33	22.07	15.15
UV+12 layers	24.15	17.99	6.16	25.5	18.58
UV only	*24.34*	*22.25*	*2.09*	*8.59*	*0*
UV+15 layers	24.34	17.11	7.23	29.7	21.12
UV+18 layers	24.34	16.17	8.17	33.57	24.98
UV+21 layers	24.34	16.62	7.72	31.72	23.13

The degradation efficiencies of TOC after 3 hours for P25 coatings with 6, 9, 12, 15, 18, and 21 layers are presented in Table 28. The degradation efficiency also increases as the number of coating layers increases from 6 to 18 layers. However, when the number of layers is further

increased to 21, the degradation efficiency decreases. This trend aligns with the UV-vis result above. This means that the different coating layers not only affect the OTC degradation but also the TOC degradation.

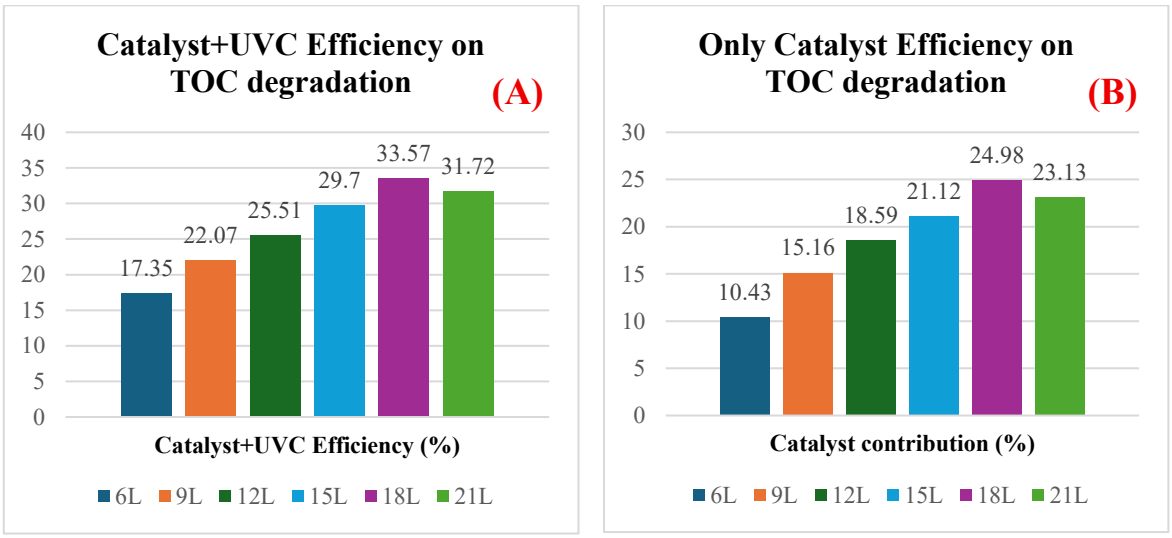

Figure 45. TOC degradation under different coating layers (A) Catalyst and UVC efficiency, (B) Catalyst contribution

Figure 45 (A) shows the total degradation efficiency of TOC under combined UVC irradiation and TiO_2 photocatalysis, while Figure 45 (B) represents the contribution of the catalyst. The sample with 18 layers again exhibits the highest performance in both cases, confirming it as the optimal coating thickness.

In contrast to the UV–Vis results for OTC degradation, the TOC removal efficiencies under UVC and catalyst are significantly lower. This is expected because TOC analysis reflects the degree of mineralization (conversion into CO_2 and H_2O), which is a more demanding process than the initial breakdown of OTC molecules into intermediate by-products. However, the contribution of the TiO_2 catalyst to TOC removal is substantial. For the optimal 18-layer sample, the total TOC removal efficiency under UVC and catalyst is 33.57%, while the catalyst alone accounts for 24.98%. This indicates that TiO_2 photocatalysis plays a dominant role in the mineralization process, whereas direct UVC photolysis contributes to a lesser extent.

These results are consistent with the earlier screening part of sol-gel and colloidal synthesis. UVC irradiation alone is effective in breaking down OTC into intermediate compounds, leading to high apparent degradation efficiency in UV–Vis measurements. However, the presence of TiO_2 is crucial for further oxidation of these intermediates into final mineralized products through the generation of reactive oxygen species like •OH radicals. Therefore, while the catalyst may appear to contribute modestly to the initial degradation stage of OTC, it is essential for achieving deeper mineralization as reflected in TOC reduction.

c) Tape test results

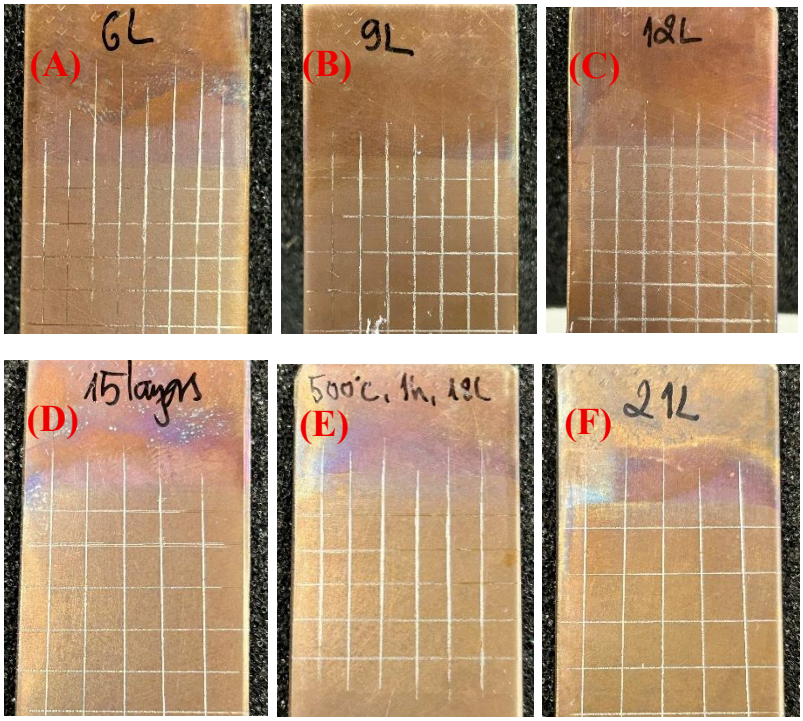

Figure 46. Tape test of coating of (A) 6 layers, (B) 9 layers, (C) 12 layers, (D) 15 layers, (E) 18 layers and (F) 21 layers

The tape test was performed on coatings with 6, 9, 12, 15, 18, and 21 dip-coating layers to evaluate their adhesion and mechanical stability. The results from Figure 46 showed that all samples exhibited good adhesion, as no significant coating removal, peeling, or delamination was observed after the tape was removed. The cross-cut areas also remained largely intact for all layer numbers, indicating strong bonding between the coating and the steel substrate, which can be classified as 4B-5B regarding ASTM D3359.

These observations suggest that increasing the number of coating layers within the investigated range did not negatively affect the adhesion performance. Therefore, all samples demonstrated satisfactory mechanical stability and adherence under the applied calcination conditions.

Table 29. Summary of results of coating layer test

Sample ID	Catalyst contribution to OTC degradation (%)	Catalyst contribution to TOC degradation (%)	Adherence
UV+6 layers	6.01	10.43	4B-5B
UV+9 layers	11.27	15.15	4B-5B
UV+12 layers	13.93	18.58	4B-5B
UV+15 layers	15.13	21.12	4B-5B
UV+18 layers	17.5	24.98	4B-5B
UV+21 layers	15.32	23.13	4B-5B

From the Table 29 for the summary, it is clear that 18 layers should be selected for next experiments due to its high activity and stable adherence.

3.2.4 Results of calcination temperature optimization

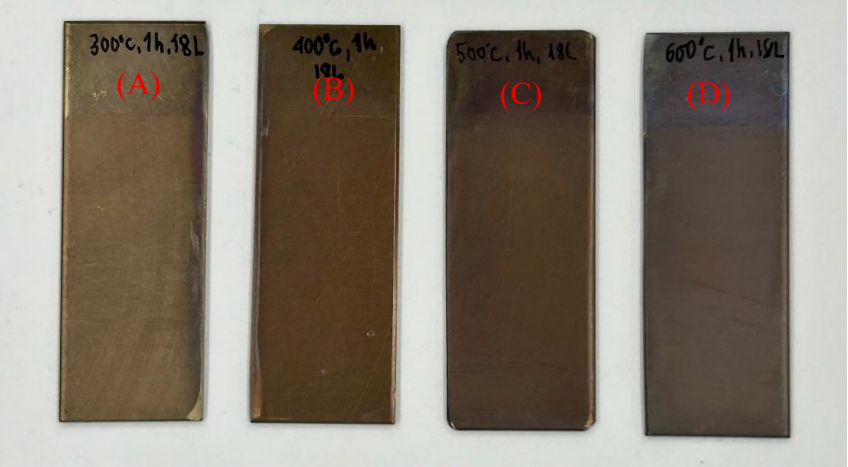

Figure 47. Substrate colours with different calcination temperatures (A) 300 °C, (B) 400 °C, (C) 500 °C and (D) 600 °C

The Figure 47 above shows the coating on steel after calcination at different temperatures. The effect of calcination temperature on the steel substrate was evaluated through observable colour changes after treatment at 300 °C, 400 °C, 500 °C, and 600 °C. A clear progression from light yellow at 300 °C to light brown at 400 °C, dark brown at 500 °C, and dark blue at 600 °C was observed. These colour variations indicate the gradual formation and thickening of oxide layers on the steel surface as temperature increases.

At lower temperatures, thin oxide films produce interference colours, while higher temperatures promote the formation of thicker iron oxide scales such as Fe_3O_4 and Fe_2O_3, resulting in darker surfaces. This confirms that oxidation of steel substrate becomes more significant with increasing calcination temperature.

a) OTC degradation results

Table 30. Degraded OTC concentration with different coating calcination temperatures

	UV-vis (355)					
Sample ID	**UV intensity (mW/cm^2)**	**OTC (mM) Before**	**OTC (mM) 3h**	**Degraded OTC (mM)**	**Efficiency (%)**	**Catalyst contribution (%)**
UV only	*4.05*	*0.1046*	*0.0419*	*0.0627*	*59.93*	*0*
UV+300 °C	4.05	0.1046	0.0133	0.0913	87.29	27.36
UV+400 °C	4.05	0.1046	0.0143	0.0903	86.32	26.39
UV+600 °C	4.05	0.1046	0.0351	0.0695	66.47	6.54
UV only	*4*	*0.1057*	*0.0347*	*0.071*	*67.17*	*0*
UV+500 °C	4	0.1057	0.0162	0.0895	84.67	17.5

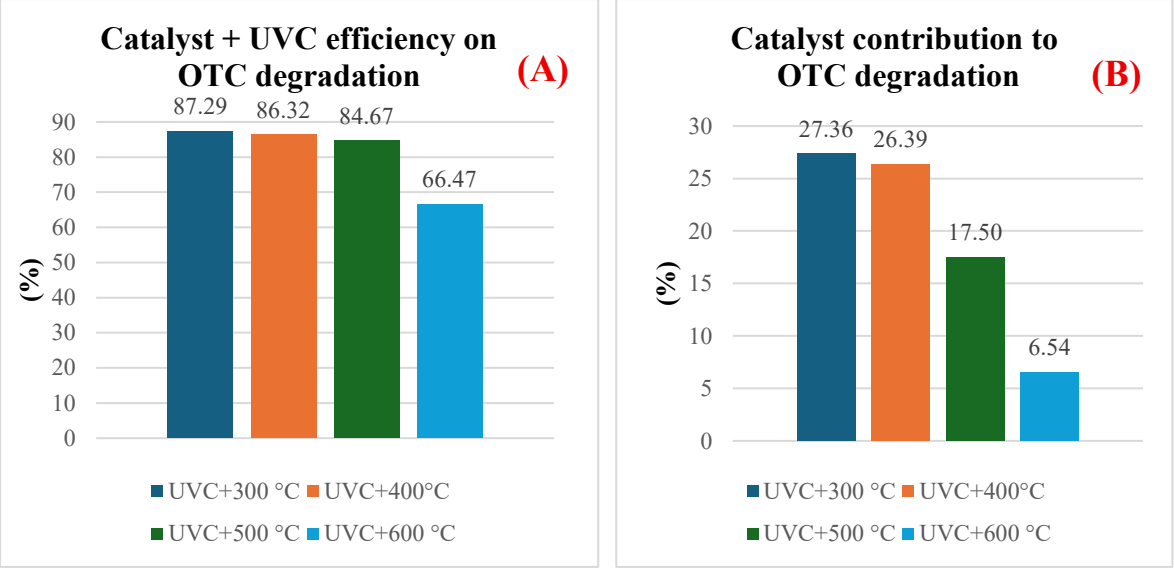

Figure 48. OTC degradation under different coating calcination temperature (A) Catalyst and UVC efficiency, (B) Catalyst contribution

The degradation efficiencies of OTC after 3 hours for P25 coatings calcined at 300 °C, 400 °C, 500 °C, and 600 °C are presented in Table 30 and Figure 48. A clear trend can be observed in which the photocatalytic degradation efficiency decreases with increasing calcination temperature. This suggests that lower calcination temperatures are more favourable for maintaining the intrinsic photocatalytic properties of commercial P25 nanoparticles after coating deposition. Commercial P25 is well known for its mixed anatase/rutile phase composition, typically around 80/20, with nanoparticle sizes in the range of 20–30 nm, which contributes to its high photocatalytic activity through efficient charge separation and high surface area [81].

As shown in Figure 48 (A), the overall OTC degradation efficiencies under UVC irradiation combined with the catalyst were relatively similar for coatings calcined at 300 °C, 400 °C, and 500 °C, with values above 84%. However, a significant decrease was observed for the coating calcined at 600 °C, where the degradation efficiency dropped to 66.47%. This indicates that excessive calcination temperature negatively affected the photocatalytic performance of the coating.

A clearer effect of calcination temperature can be observed in Figure 48 (B), which represents the contribution of the catalyst itself to OTC degradation after subtracting the effect of direct UVC photolysis. The coating calcined at 300 °C exhibited the highest catalytic contribution (27.36%). At this temperature, thermal sintering and agglomeration of nanoparticles were likely limited, allowing the particles to retain their nanoscale size and high specific surface area. In addition, the original anatase/rutile phase balance of P25 was likely preserved, maintaining efficient photocatalytic activity.

When the calcination temperature increased to 400 °C, a slight decrease in activity was observed, while more significant reductions occurred at 500 °C and especially at 600 °C. This behaviour can be explained by temperature-induced nanoparticle agglomeration and sintering, where adjacent nanoparticles fused together to form larger particles. The increase in particle

size reduces the available active surface area and limits the number of reactive sites for photocatalytic reactions [81]. Furthermore, higher calcination temperatures may promote phase transformation from anatase to rutile, altering the original phase ratio of P25. Since anatase is generally considered the more photo-catalytically active phase, excessive rutile formation can further reduce the overall photocatalytic efficiency of the coating [82].

b) TOC degradation results

Table 31. Degraded TOC concentration with different coating layers

	TOC				
Sample ID	**TOC First (mgC/L)**	**TOC Final (mgC/L)**	**Degraded TOC (mgC/L)**	**Efficiency (%)**	**Catalyst contribution (%)**
UV only	*26.74*	*25.91*	*0.83*	*3.10*	*0.00*
UV+300 °C	26.74	14.02	12.72	47.57	44.47
UV+400 °C	26.74	15.08	11.66	43.61	40.50
UV+600°C	26.74	22.26	4.48	16.75	13.65
UV only	*24.34*	*22.25*	*2.09*	*8.59*	*0.00*
UV+500°C	24.34	16.17	8.17	33.57	24.98

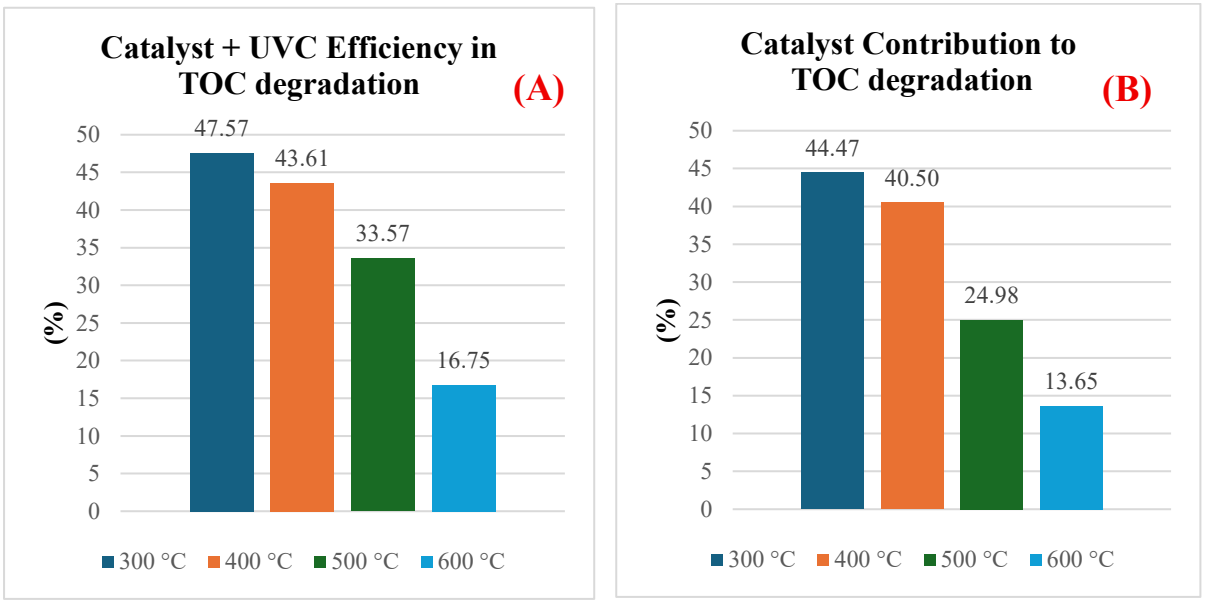

Figure 49. TOC degradation under different coating calcination temperature (A) Catalyst and UVC efficiency, (B) Catalyst contribution

The Table 31 shows the results for TOC degradation using P25 coatings calcined at different temperatures. Compared with the photocatalytic degradation results obtained from UV–Vis analysis, the TOC removal efficiencies followed a similar trend, where lower calcination temperatures resulted in better mineralization performance showed in the Figure 49. This indicates that the photocatalytic coatings calcined at lower temperatures were more effective not only in degrading OTC molecules but also in mineralizing the organic carbon content into simpler inorganic products such as CO_2 and H_2O.

The UV-only experiments from the Table 31 showed very low TOC removal efficiencies of 3.10% and 8.59%, demonstrating that direct UVC photolysis alone had limited ability to mineralize TOC. In contrast, the addition of photocatalytic coatings significantly enhanced TOC degradation as showed in the Figure 49. Among all samples, the coating calcined at 300 °C exhibited the highest TOC removal efficiency of 47.57%, with a catalyst contribution of 44.47%. This suggests that the coating retained the favourable physicochemical properties of commercial P25, including small nanoparticle size, high specific surface area, and the optimal anatase/rutile phase ratio.

When the calcination temperature increased to 400 °C, the TOC removal efficiency slightly decreased to 43.61%, although the catalytic coating still maintained relatively high contribution (40.5%). However, a more significant decrease was observed for coatings calcined at 500 °C and 600 °C, where the efficiencies dropped to 33.57% and 16.75%, respectively. The catalyst contribution also decreased correspondingly.

It was clear that the coating calcined at 300 °C exhibited the highest OTC degradation activity. However, before making the final selection, the samples were further subjected to a tape adhesion test to evaluate the strength and stability of the coating attachment on the steel substrates.

c) Tape test result

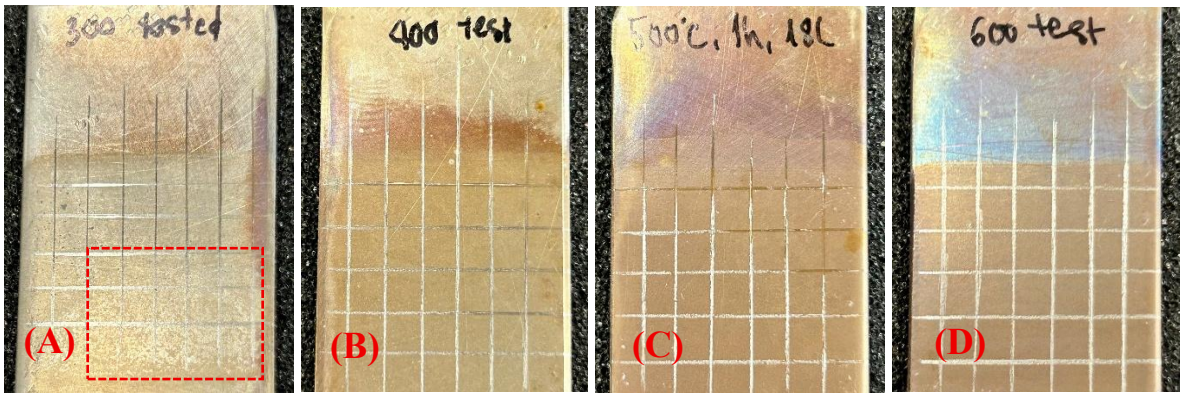

Figure 50. Tape test of coating under calcination temperature of (A) 300 °C, (B) 400 °C, (C) 500 °C and (D) 600 °C

The Figure 50 shows the adherence of P25 coatings after tape test on stainless steel substrates calcined at different temperatures. In Figure 50 (A), corresponding to the calcination temperature of 300 °C, part of the coating was removed after the tape test. According to ASTM D3359, the coating calcined at 300 °C can be classified as 1B–2B, indicating relatively poor adhesion. In contrast, the coatings calcined at 400 °C, 500 °C, and 600 °C exhibited strong adherence without noticeable peeling or delamination after the tape test, can be classified as 4B-5B.

This difference is mainly related to the thermal evolution of physically deposited P25 nanoparticles during calcination. Since the coating was prepared directly from P25 colloidal particles without sol-gel precursors or binders, the adhesion mechanism primarily depends on nanoparticle packing, particle-to-particle neck formation, and interfacial contact between TiO_2

nanoparticles and the oxide layer naturally present on the stainless-steel surface. At 300 °C, the thermal energy is relatively low for effective nanoparticle sintering. Although evaporation of residual solvent occurs, the contact between adjacent P25 nanoparticles remains weak because only limited neck growth is formed between particles. As a result, the coating structure remains loosely packed. Therefore, under mechanical stress during the tape test, parts of the coating can be easily detached [74].

When the calcination temperature increases to 400–600 °C as showed in the Figure 50 (B), (C) and (D), surface diffusion and atomic rearrangement among P25 nanoparticles become more active. This promotes partial sintering and neck formation between neighbouring nanoparticles, resulting in a denser and mechanically stronger coating network [74]. Simultaneously, higher temperature improves the physical anchoring of TiO_2 particles onto the rough oxide layer of stainless steel due to enhanced interfacial contact and particle consolidation. Consequently, the internal cohesion of the coating and the adhesion at the coating/substrate interface are significantly improved, leading to minimal peeling during the tape test.

Table 32. Summary of results of coating calcination temperature test

Sample ID	Catalyst contribution to OTC degradation (%)	Catalyst contribution to TOC degradation (%)	Adherence
UV+300 °C	27.36	44.47	1B-2B
UV+400 °C	26.39	40.5	4B-5B
UV+500 °C	17.5	24.98	4B-5B
UV+600 °C	6.54	13.65	4B-5B

The Table 32 above summarizes both the photocatalytic contribution and the adhesion performance of the coatings on the steel substrate. Although the 300 °C sample showed the highest photocatalytic activity, its adhesion performance was comparatively weaker, indicating potential instability under practical conditions.

By considering both photocatalytic efficiency and mechanical stability, the coating calcined at 400 °C was selected as the optimal condition. It offers a good balance between high catalytic activity and improved adhesion strength, making it more suitable for stable and long-term application.

3.2.5 Results of calcination time optimization

a) OTC degradation results

Table 33. Degraded OTC concentration with different coating calcination times

	UV-vis (355)					
Sample ID	**UV intensity (mW/cm^2)**	**OTC (mM) Before**	**OTC (mM) 3h**	**Degraded OTC (mM)**	**Efficiency (%)**	**Catalyst contribution (%)**
UV only	*4.05*	*0.1042*	*0.0389*	*0.0653*	*62.69*	*0*
UV+2h	4.05	0.1042	0.0124	0.0919	88.13	25.45
UV+3h	4.05	0.1042	0.0117	0.0926	88.81	26.12
UV+4h	4.05	0.1042	0.0091	0.0951	91.27	28.58
UV only	*4.05*	*0.1046*	*0.0419*	*0.0627*	*59.93*	*0*
UV+1h	4.05	0.1046	0.0143	0.0903	86.32	26.38

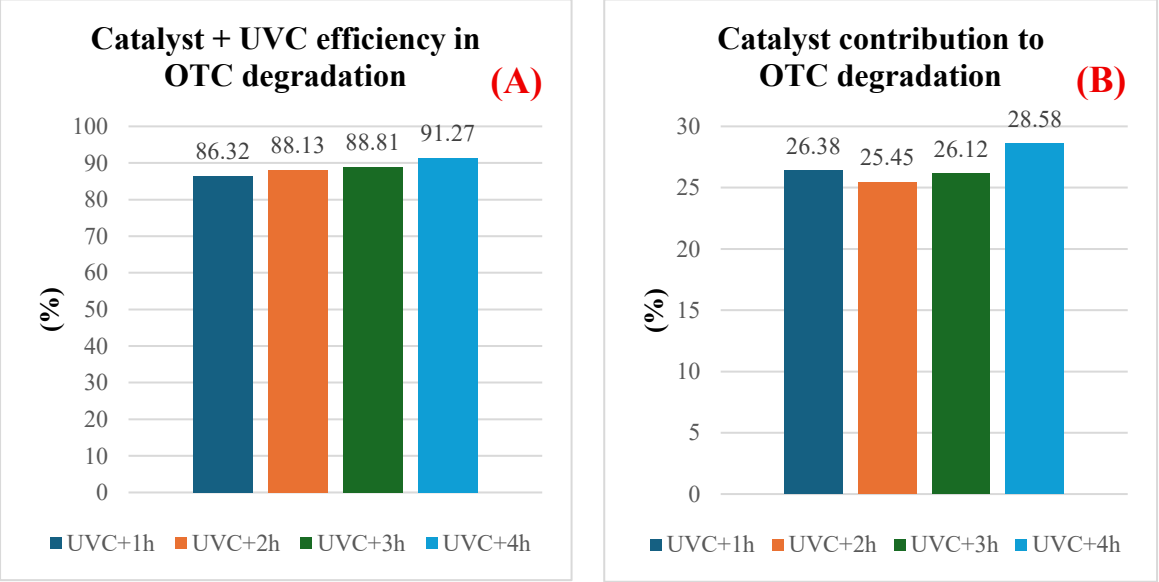

Figure 51. OTC degradation under different coating calcination time (A) Catalyst and UVC efficiency, (B) Catalyst contribution

The photocatalytic performance of P25 coatings calcined for different durations (1h, 2h, 3h and 4h) at 400 °C with 18 layers is presented in the Table 33 and Figure 51. In general, OTC degradation efficiency showed slight variations with calcination time, indicating that the duration of heat treatment also influenced the structural and surface properties of the coating.

As shown in Figure 51 (A), the overall OTC degradation efficiency gradually increased from 86.32% at 1 hour to 91.27% at 4 hours. However, this trend differs from that observed in Figure 51 (B), where the samples calcined for 1, 2, and 3 hours exhibited only minor fluctuations without a clear linear pattern. This suggests that extending the calcination duration from 1 to 3 hours did not significantly affect the photocatalytic efficiency. In contrast, the sample calcined for 4 hours demonstrated the highest photocatalytic performance among 4 samples, achieving a catalytic contribution of 28.58%. This suggests that a longer calcination time at a moderate

temperature improved the stability and crystallinity of the coating, leading to enhanced photocatalytic performance.

b) TOC degradation results

Table 34. Degraded TOC concentration with different coating calcination times

	TOC				
Sample ID	**TOC First (mgC/L)**	**TOC Final (mgC/L)**	**Degraded TOC (mgC/L)**	**Efficiency (%)**	**Catalyst contribution (%)**
UV only	*24.45*	*23.54*	*0.91*	*3.72*	*0*
UV+2h	24.45	13.36	11.09	45.36	41.64
UV+3h	24.45	14.32	10.13	41.43	37.71
UV+4h	24.45	11.89	12.56	51.37	47.65
UV only	*26.74*	*25.91*	*0.83*	*3.1*	*0*
UV+1h	26.74	15.08	11.66	43.61	40.5

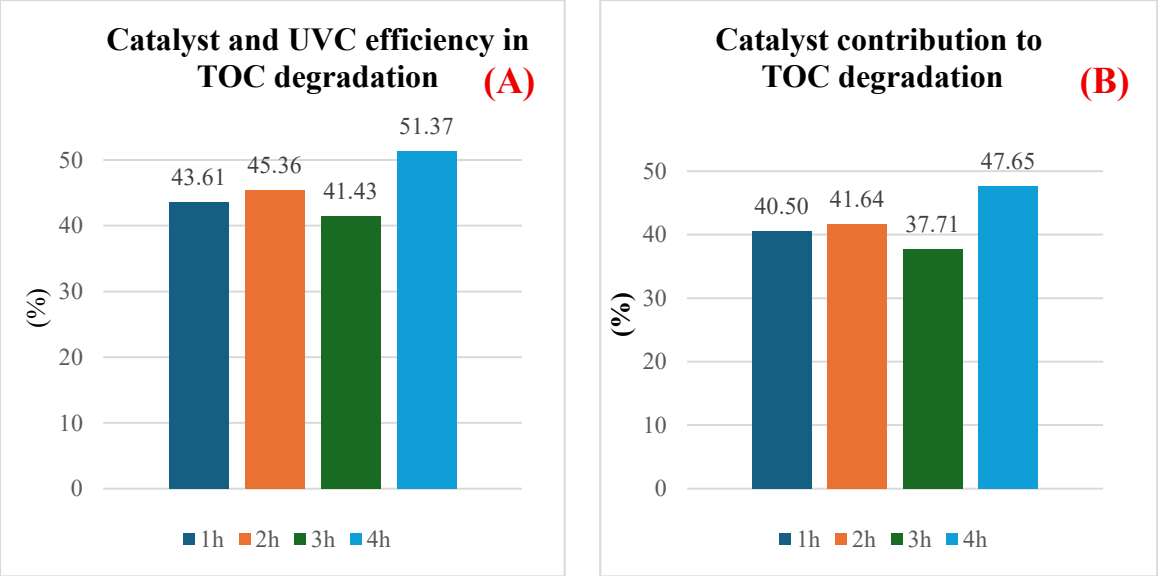

Figure 52. TOC degradation under different coating calcination time (A) Catalyst and UVC efficiency, (B) Catalyst contribution

The TOC degradation results from the Table 34 and Figure 52 also show the fluctuations among 4 samples in both total efficiency and catalyst contribution. However, the coating calcined for 4 hours achieved the highest TOC removal efficiency of 51.37%, with a catalyst contribution of 47.65%, indicating improved mineralization capability. In comparison, the coatings calcined for shorter durations showed slightly lower TOC degradation efficiencies.

The improved performance at longer calcination times may be attributed to better removal of residual organic impurities and enhanced bonding between TiO_2 particles and the substrate, reducing leaching possibility. Extended calcination can also improve crystallinity and strengthen particle connectivity, facilitating more efficient charge transfer during photocatalytic reactions.

c) Tape test result

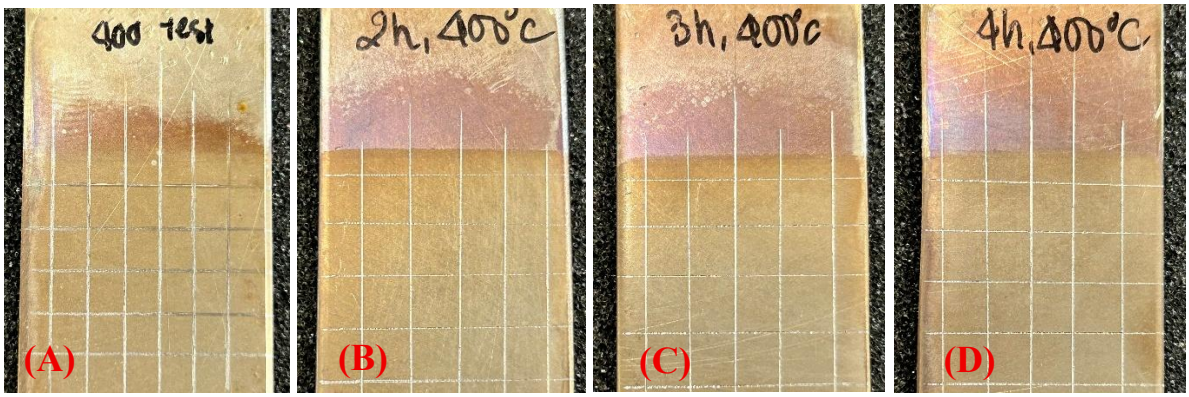

Figure 53. Tape test of coating under calcination time of (A) 1h, (B) 2h, (C) 3h and (D) 4h

The tape test was conducted on samples calcined for 1, 2, 3, and 4 hours to evaluate the adhesion and mechanical stability of the coatings at a calcination temperature of 400 °C. Based on visual observation from the Figure 53, no significant coating removal was detected on any of the four samples after the tape was peeled off. In particular, the cross-cut intersections remained intact without noticeable peeling or delamination, indicating strong adhesion between the coating and the steel substrate. Therefore, these samples could be classified as 4B-5B based on the ASTM D3359.

Table 35. Summary of results of coating calcination time test

Sample ID	Catalyst contribution to OTC degradation (%)	Catalyst contribution to TOC degradation (%)	Adherence
UV+1h	26.38	40.5	4B-5B
UV+2h	25.45	41.64	4B-5B
UV+3h	26.12	37.71	4B-5B
UV+4h	28.58	47.65	4B-5B

As shown in the Table 35, since all four samples exhibited similar adhesion performance in the tape test, the selection of the optimal calcination time was mainly based on photocatalytic activity. The differences in activity among the samples calcined for 1–3 hours were relatively small, whereas the sample calcined for 4 hours showed a more noticeable improvement in performance. Therefore, 4 hours was selected as the optimal calcination time.

3.3 Results of Characterizations of Optimal Coating

3.3.1 Coating mass via a direct measurement

Table 36. Optimal coating mass

18 layers of colloid-based coating on steel substrate		
Repeated	**Before coating (g)**	**After coating (g)**
1	11.42336	11.42486
2	11.42338	11.42488
3	11.42338	11.42485
4	11.4234	11.42484
5	11.42336	11.42485
Average	11.423376	11.424856
Coating mass (mg)	**1.48**	

The Table 36 proved that applying 18 layers significantly increased the coating mass, making direct measurement on the steel substrate feasible. Therefore, the use of a reference substrate was not necessary in this case. The results showed that the coating mass on the steel substrate with 18 layers was approximately 1.48 mg. Since the dip-coating process produced coatings on both sides of the stainless-steel substrate, the coating mass on each side was estimated to be approximately 0.74 mg.

3.3.2 Coating thickness via a profilometer method

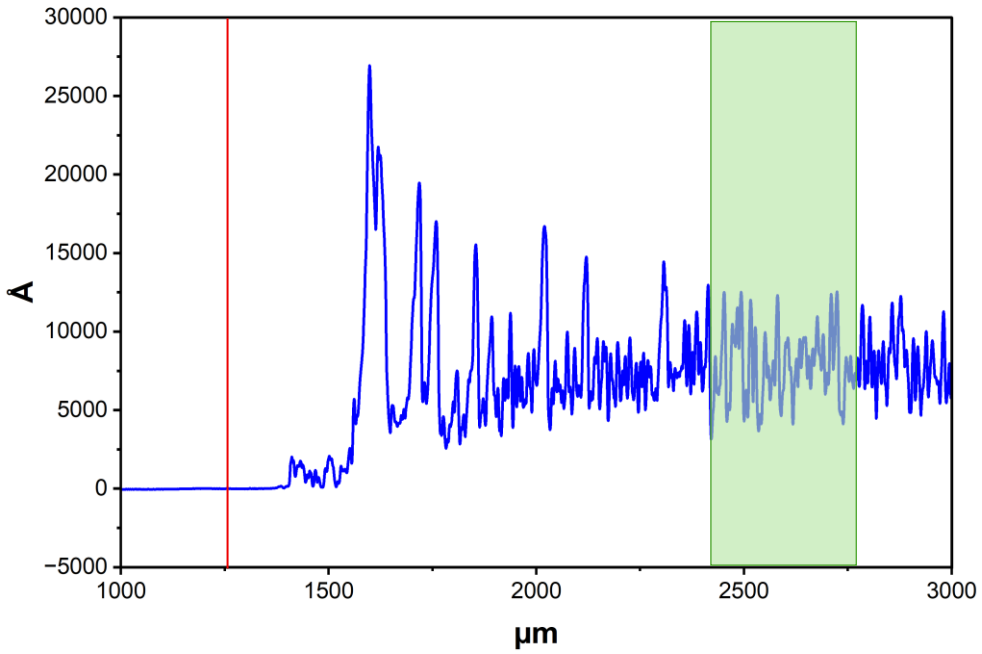

Figure 54. Optimal coating thickness on glass substrate

The profilometer analysis was conducted to determine the coating thickness of the 18-layer dip-coated film deposited on a glass (reference substrate). As shown in Figure 54, the initial

region corresponding to the bare glass substrate exhibits a relatively flat profile with minimal signal fluctuation, indicating a smooth and uniform substrate surface with low roughness.

At the interface between the glass substrate and the deposited coating, a sharp increase in the profilometer signal can be observed. This transition region is characterized by several high-intensity peaks, which are likely associated with material accumulation or agglomeration during the dip-coating process. Similar phenomena have been reported in dip-coated thin films, where non-uniform solvent evaporation and withdrawal speed can cause edge accumulation and local thickness variations [83].

The existence of a broad transition region instead of a perfectly sharp boundary suggests that the deposition process was not completely uniform at the coating edge. This behaviour is commonly observed in multilayer dip-coated films, particularly when refilling the coating solution causes slight variations in the liquid level within the container, making it difficult to maintain identical deposition conditions for each coating cycle.

Following the transition region, the profile becomes more stable, although minor fluctuations are still present due to coating inhomogeneity. In profilometry analysis, the coating thickness should generally be evaluated from the stabilized coating region rather than from isolated peak maxima, since peak values may overestimate the actual film thickness. Based on the average height difference between the substrate baseline and the stabilized coated region, the coating thickness was estimated to be approximately 650–800 nm with the roughness level of about 300-400 nm.

Although the surface properties of steel and glass substrates are different, including differences in surface roughness, surface energy, and wettability, the samples were fabricated using the same dip-coating parameters and the same number of coating layers (18 layers). Therefore, it can be reasonably suggested that the coating thickness on the steel substrate is also within a range of approximately **650–800 nm**, although slight variations may occur due to the different substrate characteristics.

3.3.3 Characterization of optimal coating by SEM-EDX

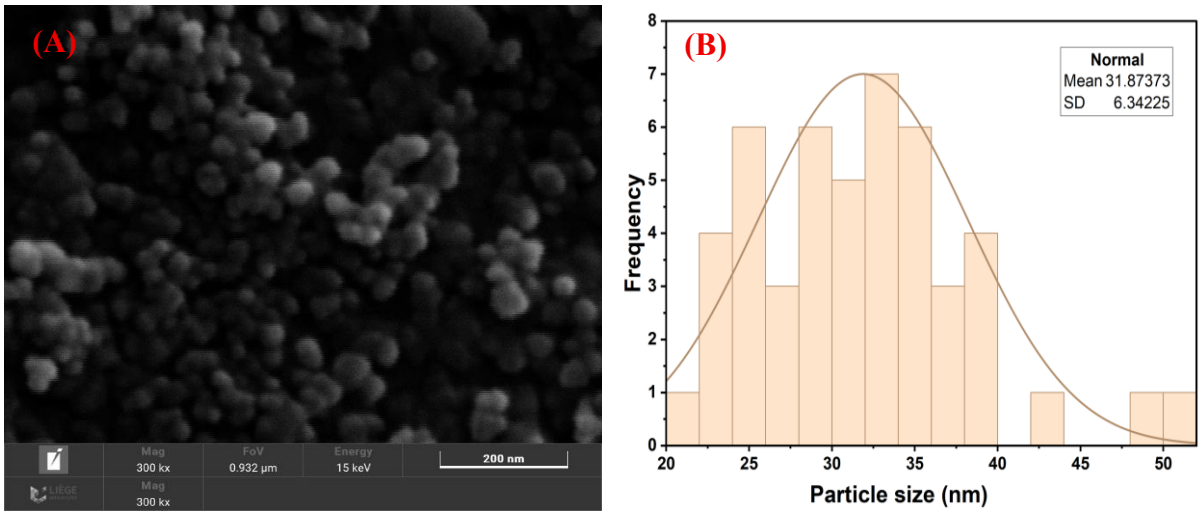

Figure 55. SEM images of (A) optimal coating at 300 kx magnitude, (B) particle size distribution

The Figure 55 (A) shows that the P25 nanoparticles of optimal coating sample exhibit a predominantly spherical morphology and appear to form agglomerated clusters while the Figure 55 (B) presents the particle size distribution obtained from ImageJ measurements. The particle size distribution is approximately described by a Gaussian function, with an average particle size of 31.87 nm and a standard deviation of 6.34 nm. Most measured particles fall within the size range of 25–40 nm, indicating that the majority of particles are concentrated around the mean size. A small number of particles with sizes exceeding 45 nm were also observed. These larger sizes may be associated with particle agglomeration or partial particle fusion occurring during the calcination process which was explained before.

To confirm the elemental composition of the deposited layer, the EDX spectrum is introduced below.

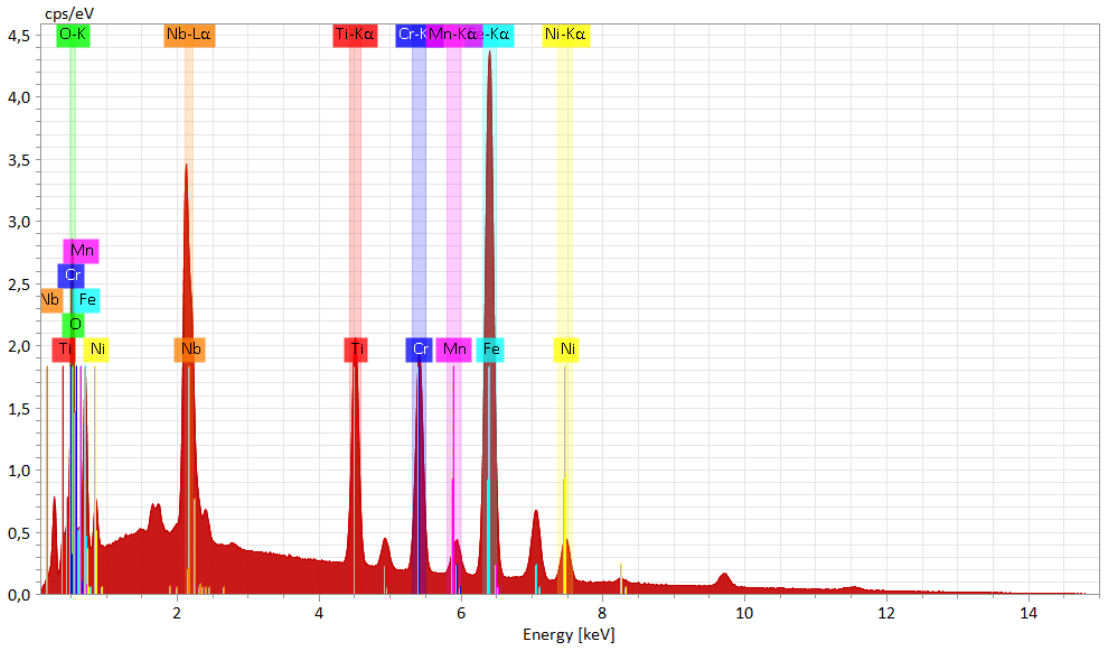

Figure 56. EDX spectrum of the optimal coating

Figure 56 presents the EDX spectrum of the TiO_2-coated stainless-steel substrate acquired at an accelerating voltage of 15 kV. The spectrum shows the characteristic peaks of Ti and O, confirming the presence of the TiO_2 coating on the substrate surface. In addition to Ti and O, peaks corresponding to Fe, Cr, Ni, and Mn were also detected. These elements originate from the stainless-steel substrate, and their appearance can be attributed to the relatively large interaction volume of the electron beam at 15 kV, which allows X-rays to be generated from both the coating and the underlying substrate. This suggests that the detected signal contains contributions from the substrate in addition to the TiO_2 coating. A Nb peak was also observed in the spectrum. Since Nb was not intentionally introduced during the coating preparation, its presence may be associated with trace contamination, or impurities originating from the precursor materials or processing equipment. Overall, the EDX analysis confirms the successful deposition of TiO_2 on the stainless-steel substrate while also indicating contributions from the substrate elements during measurement.

3.3.4 Characterization of optimal coating by XRD patterns

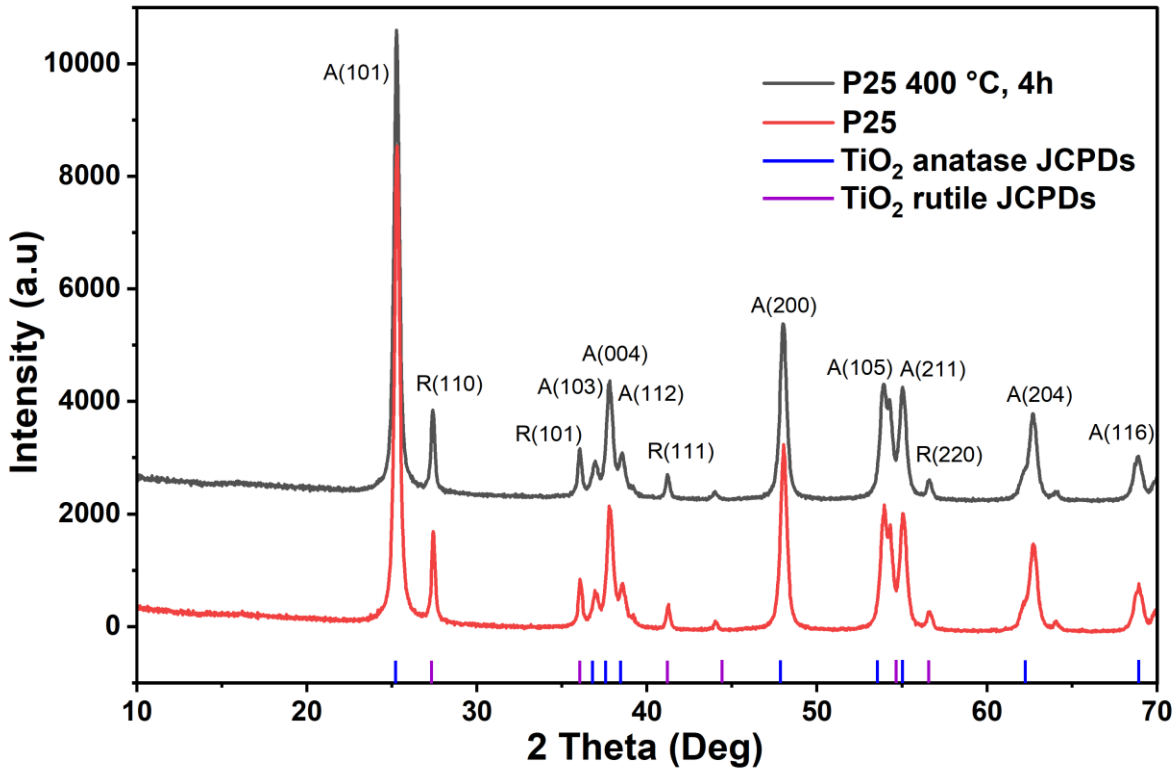

Figure 57. XRD patterns of the optimal P25 (400 °C, 4h) and pristine P25

The Figure 57 illustrates that the XRD patterns of pristine P25 and optimal P25 (calcined at 400 °C for 4 h) under the powder form exhibited identical diffraction peak positions corresponding to the anatase and rutile phases, which were in good agreement with the standard diffraction data of TiO_2. No additional diffraction peaks were detected after calcination, indicating that the thermal treatment did not induce the formation of any new crystalline phases.

A slight reduction in the intensity of the characteristic anatase A (101) peak at approximately 25.3° was observed, decreasing from 8717 counts for pristine P25 to 8459 counts after calcination. Similarly, the intensity of the rutile R (110) peak at approximately 27.5° decreased from 1873 to 1708 counts. However, the decrease in peak intensity was relatively small and is insufficient to indicate a significant change in crystallinity. Such minor variations may arise from differences in sample packing, preferred orientation, or measurement conditions rather than from substantial structural changes.

The phase composition was estimated using the Spurr–Myers equation based on the intensities of the anatase (101) and rutile (110) reflections. The pristine P25 sample contained approximately 78.8 wt.% anatase and 21.2 wt.% rutile, whereas the calcined sample contained approximately 79.8 wt.% anatase and 20.2 wt.% rutile. The difference in phase composition was less than 1 wt.%, indicating that calcination at 400 °C for 4 h did not promote a noticeable anatase-to-rutile phase transformation [84].

Overall, the XRD results demonstrate that calcination at 400 °C for 4 h had a negligible effect on both the crystallinity and phase composition of P25, aligned with the observation from previous studies [85]. The characteristic mixed anatase–rutile structure of the commercial P25 powder was preserved after thermal treatment, confirming the structural stability of the material under the applied calcination conditions.

3.4 Results of reusability test

a) OTC degradation results

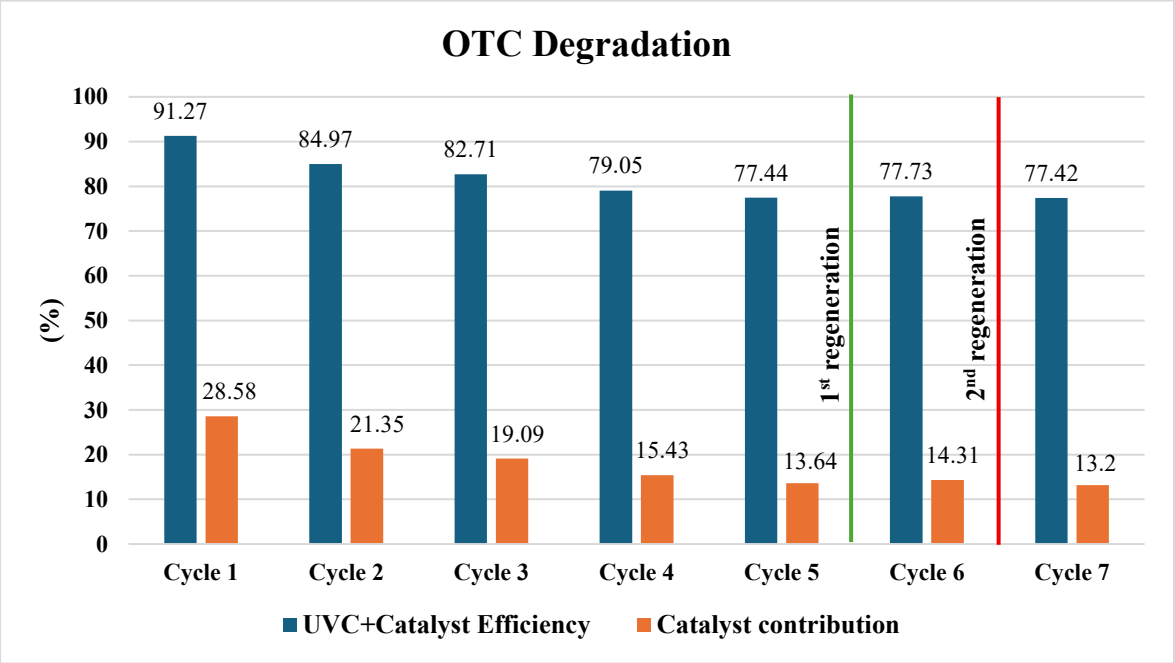

Figure 58. OTC degradation on reusability test

The UV–Vis results demonstrated that repeated use of the catalyst led to a gradual decline in photocatalytic activity. As shown in the Figure 58, the total removal efficiency achieved by the combined effect of UVC irradiation and the catalyst decreased from 91.27% to 77.44% after 5 cycles. Similarly, the contribution of the catalyst itself declined from 28.58% to 13.64% over the same period. This decrease indicates that, during repeated cycles, degradation by-products may accumulate on the catalyst surface and block active sites, thereby reducing photocatalytic performance. In addition, possible TiO_2 leaching over time may also contribute to the activity loss.

However, after applying the regeneration procedure, the catalyst exhibited improved activity in cycle 6, as the efficiency increased a bit compared to cycle 5. Although the improvement was very small, the regeneration process helped stabilize the catalyst performance and prevented further significant decline. This suggests that regeneration was effective in removing surface by-products, partially restoring the self-cleaning ability of the catalyst.

Nevertheless, the 3-hour regeneration period may not have been sufficient to completely remove organic molecules such as OTC and its degradation by-products, which possess relatively large and complex structures. Therefore, a second regeneration process was carried

out overnight (approximately 16 hours) to investigate whether a longer treatment could remove more pollutants from the coating surface and further enhance the photocatalytic activity.

However, the results of cycle 7 showed a slight decrease in OTC degradation efficiency. This indicates that extending the regeneration duration did not significantly improve the catalyst activity. Overall, considering the results from cycles 5 to 7, the regeneration process mainly helped maintain the photocatalytic activity and prevent further decline, but it was difficult to fully restore the catalyst to its original performance.

b) TOC degradation results

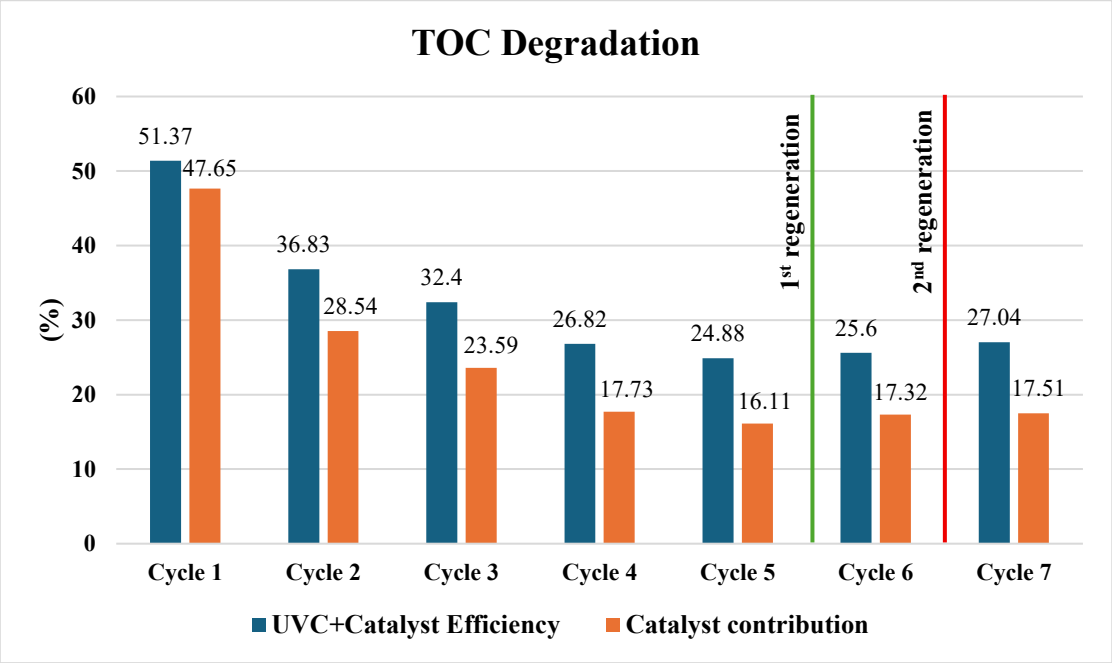

Figure 59. TOC degradation on reusability test

The TOC analysis from the Figure 59 showed a similar trend to the UV–Vis results before regeneration processes, where the total TOC removal efficiency decreased from 51.37% to 24.88%, while the catalyst contribution declined from 47.65% to 16.11% after 5 cycles. This reduction confirms that the blockage of active sites affected not only the degradation of OTC in subsequent cycles but also the degradation of its intermediate products.

After the first regeneration process, cycle 6 exhibited an increase in photocatalytic activity. Notably, the improvement observed in the TOC analysis was more pronounced than that observed in the UV–Vis results for OTC degradation. Following the second regeneration process, cycle 7 continued to show improvements in both the total efficiency and the catalyst contribution toward TOC degradation, although the catalyst activity was still not fully restored to its original performance.

These results suggest that the regeneration process helped recover a greater number of active sites responsible for deep oxidation and mineralization reactions. Therefore, regeneration was more effective in restoring the catalyst's mineralization capability than its ability to degrade the parent OTC molecules alone.

Based on these findings, regular regeneration after each cycle appears to be important for maintaining catalyst performance, as the continuous accumulation of by-products over multiple cycles may lead to irreversible aging of the photocatalytic coating.

3.5 Results of adsorption test of P25 coating and powder

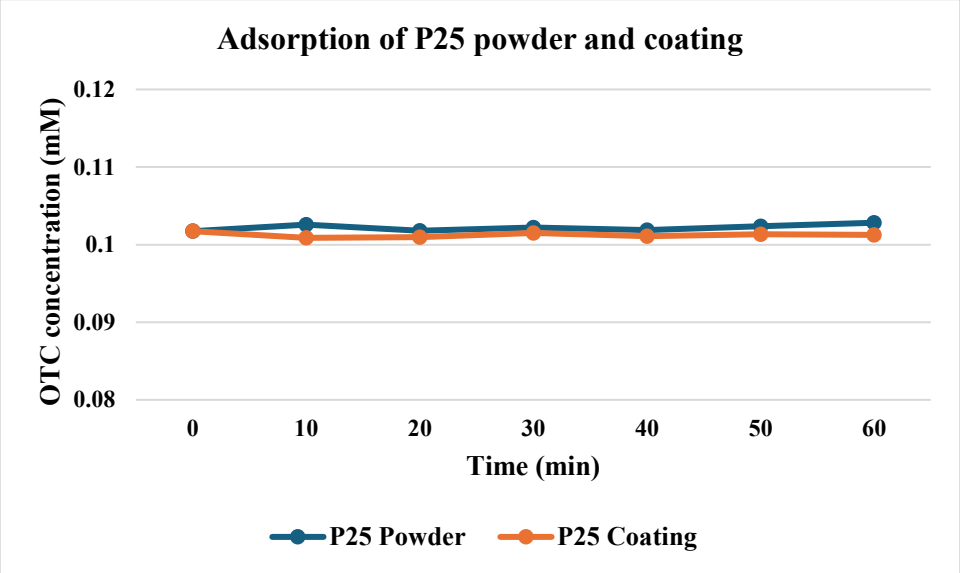

Figure 60. Adsorption test of P25 coating and powder

As shown in the Figure 60, the adsorption behaviour of OTC on both P25 powder and P25 coating systems was negligible over the 60-minute dark equilibrium period. The OTC concentration remained almost constant at approximately 0.10 mM for both systems, with only minor fluctuations observed throughout the experiment. This indicates that neither system exhibited significant adsorption capacity toward OTC prior to irradiation.

3.6 Results of photocatalytic activity comparison of P25 coating and powder

3.6.1 Photocatalytic efficiency

a) OTC degradation results

The Figure 61 below shows that at the end of the 3-hour reaction period, the P25 powder system achieved complete degradation (approximately 100% total efficiency), while the P25 coating system exhibited a highly competitive total degradation efficiency of approximately 92.5%. The catalyst contributions for the P25 powder and coating systems were 36.89% and 28.01%, respectively.

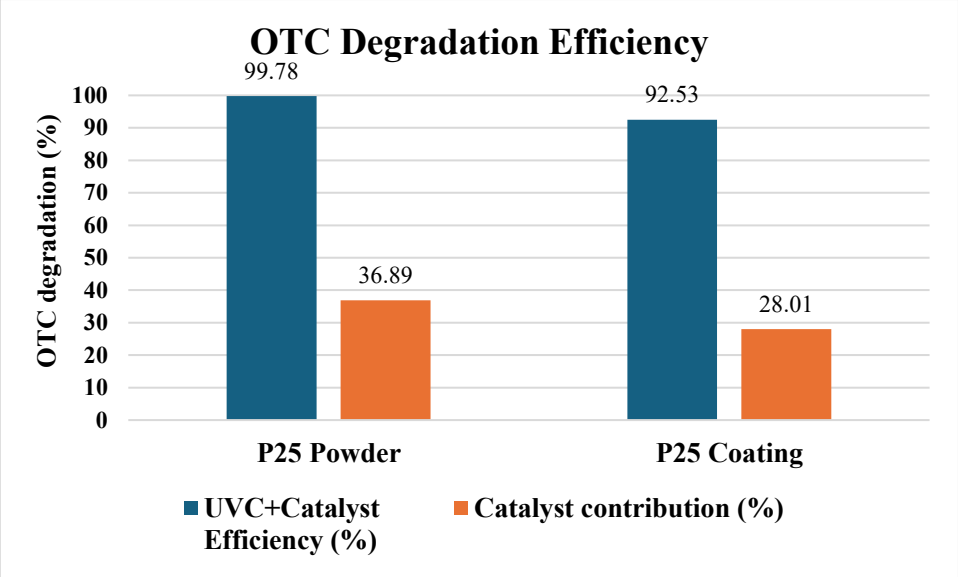

Figure 61. OTC degradation efficiency of P25 coating and powder

The higher degradation efficiency observed for the P25 powder can be attributed primarily to its larger effective surface area and better contact with OTC molecules. In the suspended powder system, TiO_2 particles are freely dispersed throughout the solution, allowing a greater number of active sites to be exposed to both the incident light and the pollutant molecules. This enhances the generation of reactive oxygen species (ROS), such as hydroxyl radicals (•OH) and superoxide radicals ($O_2•^-$), which are responsible for OTC degradation. Furthermore, continuous mixing promotes uniform particle distribution and minimizes mass transfer limitations, facilitating efficient pollutant transport to the catalyst surface.

In contrast, the P25 coating system exhibited a slightly lower degradation efficiency (92.5%), which can be explained by the immobilization of the catalyst on the substrate. Immobilization typically reduces the accessible surface area because a fraction of the TiO_2 particles is embedded within the coating layer or remains in direct contact with the substrate. Moreover, coating system required the calcination step, which promotes the coalescence of adjacent TiO_2 nanoparticles, resulting in particle growth and a corresponding decrease in specific surface area. The reduction in surface area decreases the number of accessible photocatalytic active sites and adsorption sites for OTC molecules, thereby limiting photocatalytic degradation efficiency.

In addition, the transport of OTC molecules from the bulk solution to the catalyst surface is governed by diffusion, leading to greater mass transfer resistance compared with the suspended powder system. The fixed catalyst layer may also experience partial light shielding and reduced light penetration through the coating thickness, which can decrease the number of photo-generated electron–hole pairs. These results are consistent with previous studies comparing TiO_2 powder and immobilized TiO_2 coatings [86].

b) TOC degradation results

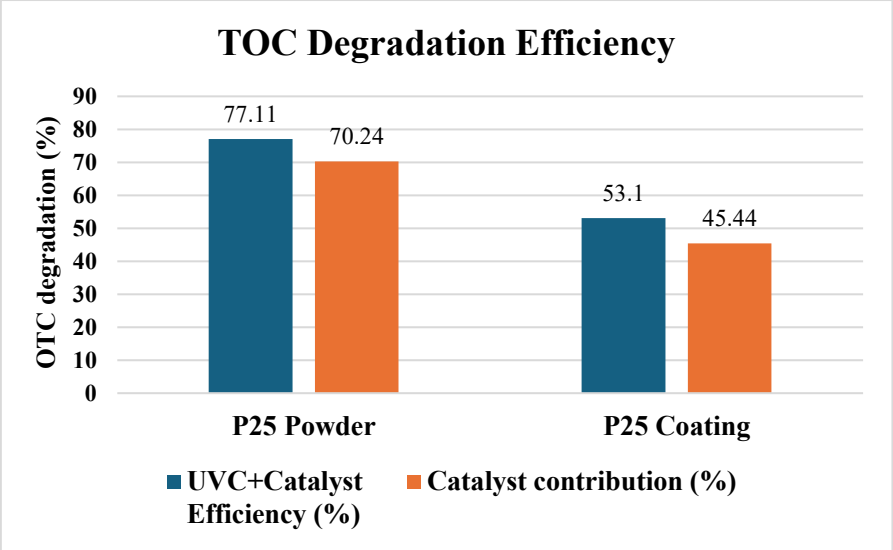

Figure 62. TOC degradation efficiency of P25 coating and powder

As shown in Figure 62, the overall TOC degradation efficiency (UVC and catalyst) was substantially higher for the P25 powder system (77.11%) than for the P25 coating system (53.10%). Similarly, the catalyst contribution was greater in the powder system, reaching 70.24%, compared to 45.44% for the coating system. This trend is consistent with the OTC degradation results discussed previously. The findings indicate that the factors influencing OTC degradation also affected the mineralization of its intermediate by-products, suggesting that nanoparticle size, active site availability, light penetration, and mass transfer characteristics played important roles in determining the overall TOC removal efficiency.

3.6.2 Kinetics analysis of OTC degradation

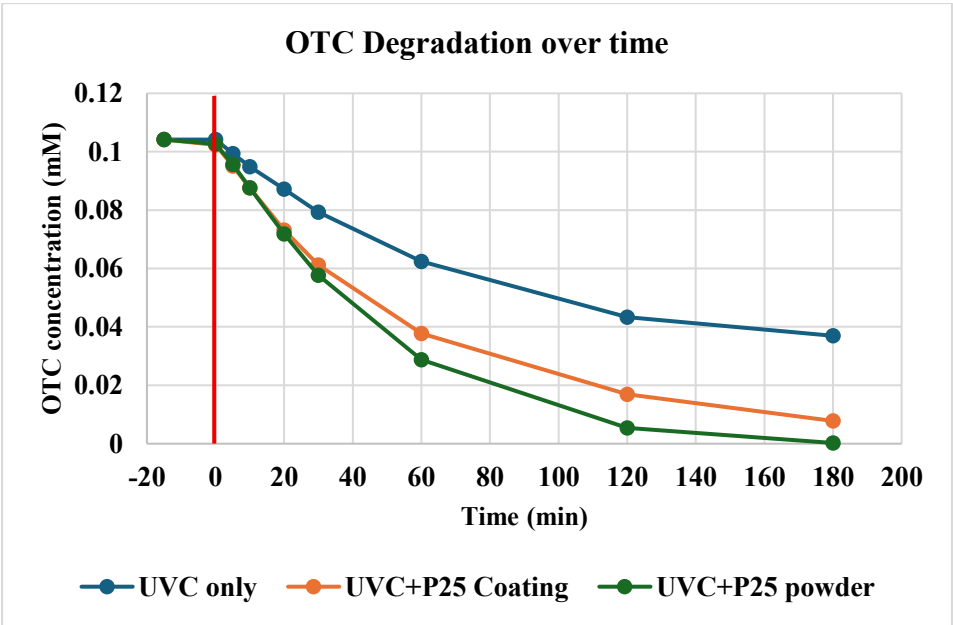

Figure 63. Kinetics of OTC degradation

Table 37. OTC concentration in P25 coating and P25 powder system over time

	-15 mins	0 min	5 mins	10 mins	20 mins	30 mins	60 mins	120 mins	180 mins
UVC only	0.1041	0.1041	0.0993	0.0949	0.0872	0.0793	0.0625	0.0433	0.0369
P25 Powder	0.1041	0.1027	0.0957	0.0877	0.0719	0.0577	0.0288	0.0054	0.0002
P25 Coating	0.1041	0.1023	0.0951	0.0877	0.0732	0.0612	0.0378	0.0169	0.0078

From the Figure 63 and Table 37, prior to UVC illumination, these samples were kept in the dark for 15 minutes to create the adsorption-desorption equilibrium of OTC on the catalyst surfaces. In the presence of both P25 powder and P25 coating, a minor decrease in OTC concentration was recorded, dropping from an initial value of 0.1041 to approximately 0.1027 and 0.1023, respectively. After 30 minutes under UVC illumination, the P25 powder started degrading OTC much more than P25 coating. Based on the results obtained for both P25 coating and P25 powder, the photocatalytic degradation kinetics of OTC were evaluated using three kinetic models, namely zero-order, pseudo-first-order, and pseudo-second-order models. The corresponding coefficients of determination (R^2) are summarized in the Table 38 below:

Table 38. Corresponding coefficients of determination (R^2)

	R^2 zero-order	R^2 first-order	R^2 second-order
OTC degradation based on P25 coating	0.8803	0.997	0.9336
OTC degradation based on P25 powder	0.8618	0.9669	0.6636

For both P25 coating and powder system, the pseudo-first-order model exhibited the highest R^2 value (0.997 and 0.9669), significantly higher than those obtained from the zero-order and pseudo-second-order models. This indicates that the degradation of OTC under UVC irradiation follows pseudo-first-order kinetics more closely than the other models. This observation is consistent with previous studies, which have likewise reported that the photocatalytic degradation of OTC generally follows a pseudo-first-order kinetic behaviour [87].

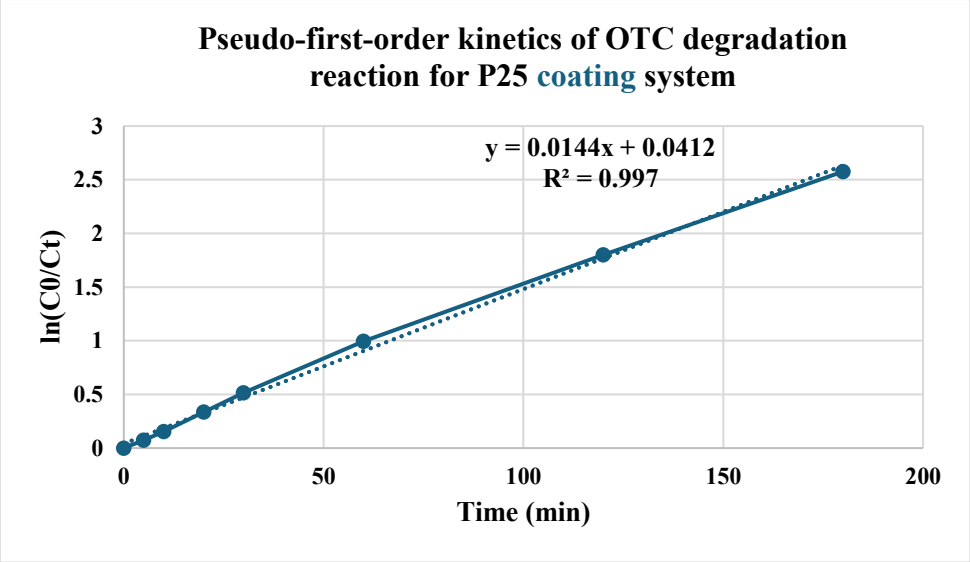

Figure 64. Pseudo-first-order kinetics: P25 Coating

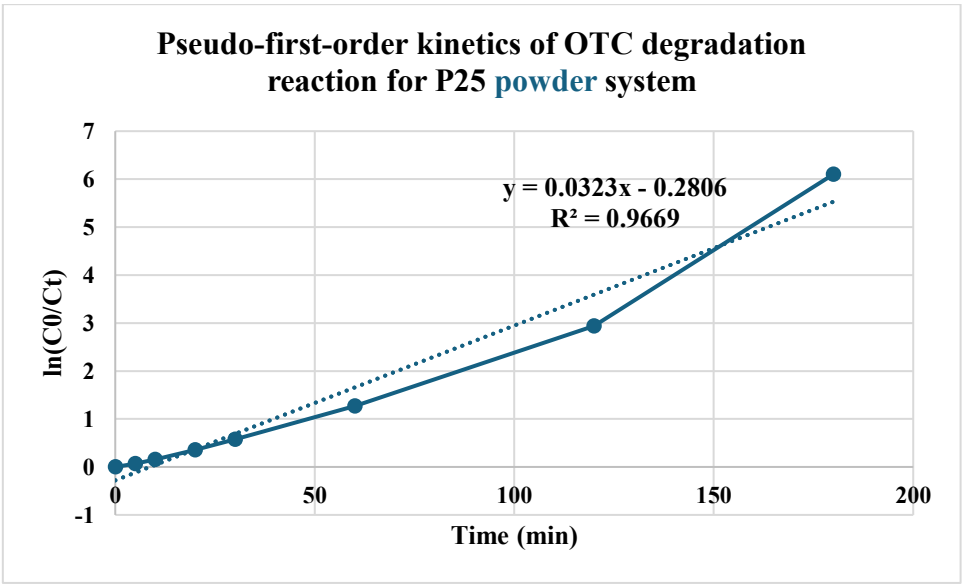

Figure 65. Pseudo-first-order kinetics: P25 Powder

The Figure 64 and Figure 65 showed that the P25 powder system shows a significantly higher rate constant (k_1 = 0.0323) compared to the coating system (k_2 = 0.0144). This indicates that P25 powder degrades OTC more efficiently and faster than P25 coating.

4 Conclusions and Recommendations

4.1 Conclusions

The widespread use of antibiotics in shrimp aquaculture in Vietnam has raised increasing concerns regarding the discharge of antibiotic-contaminated wastewater into aquatic environments. Excessive antibiotic residues can contribute to the development of antimicrobial resistance, negatively affect aquatic ecosystems, and compromise water quality. Therefore, developing effective, reusable, and environmentally friendly technologies for antibiotic removal is essential for sustainable aquaculture practices. In this context, photocatalytic coatings based on TiO_2 offer a promising solution due to their ability to degrade organic pollutants without requiring additional chemicals and their potential for repeated use.

The primary objective of this study was to develop a TiO_2 photocatalytic coating with high photocatalytic activity and strong adhesion to a stainless-steel substrate. To achieve this goal, the research was divided into two main phases: (i) screening different catalyst preparation methods and (ii) optimizing and characterizing the most promising photocatalytic coating.

In the screening phase, four photocatalysts prepared by the sol-gel method and one photocatalyst prepared by the colloidal synthesis method were investigated. The experimental procedure included catalyst preparation, dip-coating deposition, drying, calcination, photocatalytic degradation under UVC irradiation, adhesion testing, material characterization, and photocatalytic performance evaluation. The results demonstrated that both sol-gel and colloidal coatings exhibited satisfactory adhesion to stainless steel substrates. However, the photocatalytic activity of the colloidal coating was significantly higher than that of the sol-gel coatings. This difference was attributed to the superior crystalline structure and phase composition of the colloidal coating. After calcination, the sol-gel coatings exhibited relatively low crystallinity and lacked the beneficial anatase-rutile mixed-phase structure. In contrast, the colloidal coating preserved the intrinsic properties of commercial P25 TiO_2, including its high crystallinity and favourable anatase-rutile phase composition, which are known to enhance charge separation and photocatalytic performance. From an economic perspective, the colloidal coating was also more attractive because commercially available P25 powder is relatively affordable and eliminates the need for precursor synthesis and additional processing steps associated with the sol-gel method.

Based on the screening results, the colloidal P25 coating was selected for further optimization. Several parameters were systematically investigated, including the number of coating layers, calcination temperature, calcination duration, coating stability, reusability, and performance comparison with suspended P25 powder. The results indicated that the optimal coating was obtained using 18 coating layers, corresponding to an estimated thickness of approximately 650–800 nm, followed by calcination at 400 °C for 4 hours. Under these conditions, the coating achieved the highest photocatalytic performance while maintaining good adhesion and structural stability.

The reusability study revealed a gradual decline in photocatalytic activity over multiple operating cycles. This reduction was mainly attributed to the accumulation of degradation intermediates and residual pollutants on the coating surface, which blocked active sites and hindered photocatalytic reactions. Regeneration treatments were able to slow down further activity loss and partially maintain coating performance; however, they were not sufficient to fully restore the original photocatalytic activity. In addition, a small amount of TiO_2 could gradually detach from the coating during long-term operation, contributing to the decrease in activity over time.

A comparison between immobilized P25 coating and suspended P25 powder demonstrated that the powder system achieved superior photocatalytic performance, reaching 99.78% OTC degradation and 77.11% TOC removal. Nevertheless, the P25 coating also exhibited high photocatalytic efficiency, achieving 92.53% OTC degradation and 53.10% TOC removal. Although the immobilized coating showed somewhat lower degradation efficiency, it offers several practical advantages, including easy recovery, elimination of post-treatment catalyst separation, improved reusability, and reduced risk of nanoparticle release into the environment. Considering these operational and environmental benefits, the P25 coating represents a promising alternative for practical wastewater treatment applications.

Despite the positive results obtained in this study, several limitations were encountered. The coating thickness could not be directly measured on the stainless-steel substrate and was instead estimated using coated glass substrates as references. Therefore, the exact coating thickness on stainless-steel could not be accurately determined, and only a range of thickness values could be provided. Accurate coating mass measurements were only possible for relatively thick coatings. If the coating is excessively thin, the mass gain after deposition may be too small to be measured reliably. Therefore, a reference substrate may be required for coating mass determination. Furthermore, direct XRD characterization of the coating layer was not feasible because of the unavailability of equipment; therefore, the coating material had to be collected and analysed in powder form to infer the crystallinity and phase composition of the deposited layer. Additionally, the gradual decrease in photocatalytic activity caused by fouling and TiO_2 leaching remains a challenge for long-term operation.

4.2 Recommendations

Future studies should focus on improving the long-term stability and reusability of the photocatalytic coating. Since surface fouling was identified as a major cause of activity loss, regeneration procedures should be applied immediately after each operating cycle to prevent the accumulation of contaminants on the coating surface. Early-stage regeneration is expected to be more effective than attempting to remove heavily accumulated deposits after prolonged operation.

Further research should also investigate strategies to minimize TiO_2 leaching and improve coating durability. Possible approaches include the incorporation of suitable binders, surface modification techniques, or elemental doping to strengthen the interaction between TiO_2 particles and the substrate.

Although the optimized P25 coating exhibited high photocatalytic activity, its performance remained lower than that of suspended P25 powder. Therefore, future work should explore methods to further enhance photocatalytic efficiency, such as metal or non-metal doping, heterojunction formation, surface modification, or the incorporation of co-catalysts. These approaches may improve charge separation efficiency, increase light utilization, and ultimately bridge the performance gap between immobilized coatings and suspended photocatalyst systems.

Overall, the findings of this study demonstrate that immobilized P25 TiO_2 coatings can achieve high photocatalytic activity, good adhesion, and practical operational advantages, making them a promising candidate for the treatment of antibiotic-contaminated aquaculture wastewater.

References

[1] T. Tran *et al.*, "Promoting sustainable shrimp farming: balancing environmental goals, awareness, and socio-cultural factors in the Mekong Delta aquaculture," *Aquaculture International*, vol. 33, Jan. 2025, doi: 10.1007/s10499-024-01802-y.

[2] L. T. That and H. Y. Hoang, "Utilizing a settling pond-based constructed wetland for the treatment of shrimp aquaculture wastewater – From laboratory to field scale: A case study in Ben Tre Province, Vietnam," *Ecol. Eng.*, vol. 199, Feb. 2024, doi: 10.1016/j.ecoleng.2023.107172.

[3] G. H. Ström *et al.*, "Antibiotic Use by Small-Scale Farmers for Freshwater Aquaculture in the Upper Mekong Delta, Vietnam," *J. Aquat. Anim. Health*, vol. 31, pp. 290–298, Sep. 2019, doi: 10.1002/aah.10084.

[4] Q. H. Luu, T. B. T. Nguyen, T. L. A. Nguyen, T. T. T. Do, T. H. T. Dao, and P. Padungtod, "Antibiotics use in fish and shrimp farms in Vietnam," *Aquac. Rep.*, vol. 20, Jul. 2021, doi: 10.1016/j.aqrep.2021.100711.

[5] F. Li, J. Huang, M. Wang, L. Chen, and Y. Xiao, "Sources, distribution and dynamics of antibiotics in Litopenaeus vannamei farming environment," *Aquaculture*, vol. 545, Dec. 2021, doi: 10.1016/j.aquaculture.2021.737200.

[6] P. Grenni, V. Ancona, and A. Barra Caracciolo, "Ecological effects of antibiotics on natural ecosystems: A review," *Microchemical Journal*, vol. 136, pp. 25–39, Jan. 2018, doi: 10.1016/j.microc.2017.02.006.

[7] L. Zhu, X. Lin, Z. Di, F. Cheng, and J. Xu, "Occurrence, Risks, and Removal Methods of Antibiotics in Urban Wastewater Treatment Systems: A Review," Dec. 2024, *Multidisciplinary Digital Publishing Institute (MDPI)*. doi: 10.3390/w16233428.

[8] C. J. Murray *et al.*, "Global burden of bacterial antimicrobial resistance in 2019: a systematic analysis," *The Lancet*, vol. 399, pp. 629–655, Feb. 2022, doi: 10.1016/S0140-6736(21)02724-0.

[9] A. Singh, S. G. Pratap, and A. Raj, "Occurrence and dissemination of antibiotics and antibiotic resistance in aquatic environment and its ecological implications: a review," Jul. 2024, *Springer*. doi: 10.1007/s11356-024-34355-x.

[10] D. K. Pham *et al.*, "Monitoring Antibiotic Use and Residue in Freshwater Aquaculture for Domestic Use in Vietnam," *Ecohealth*, vol. 12, pp. 480–489, Sep. 2015, doi: 10.1007/s10393-014-1006-z.

[11] H. Dong, X. Yuan, W. Wang, and Z. Qiang, "Occurrence and removal of antibiotics in ecological and conventional wastewater treatment processes: A field study," *J. Environ. Manage.*, vol. 178, pp. 11–19, Aug. 2016, doi: 10.1016/j.jenvman.2016.04.037.

[12] G. Crini and E. Lichtfouse, “Advantages and disadvantages of techniques used for wastewater treatment,” Mar. 2019, *Springer Verlag*. doi: 10.1007/s10311-018-0785-9.

[13] D. B. Miklos, C. Remy, M. Jekel, K. G. Linden, J. E. Drewes, and U. Hübner, “Evaluation of advanced oxidation processes for water and wastewater treatment – A critical review,” Aug. 2018, *Elsevier Ltd*. doi: 10.1016/j.watres.2018.03.042.

[14] T. H. Zheng, Z. Z. Zhang, Y. Liu, and L. H. Zou, “Recent Progress in Catalytically Driven Advanced Oxidation Processes for Wastewater Treatment,” Aug. 2025, *Multidisciplinary Digital Publishing Institute (MDPI)*. doi: 10.3390/catal15080761.

[15] G. Ren *et al.*, “Recent advances of photocatalytic application in water treatment: A review,” Jul. 2021, *MDPI AG*. doi: 10.3390/nano11071804.

[16] S. Shurbaji, P. T. Huong, and T. M. Altahtamouni, “Review on the visible light photocatalysis for the decomposition of ciprofloxacin, norfloxacin, tetracyclines, and sulfonamides antibiotics in wastewater,” Apr. 2021, *MDPI*. doi: 10.3390/catal11040437.

[17] P. Chalatsi-Diamanti, E. A. Isari, E. Grilla, P. Kokkinos, and I. K. Kalavrouziotis, “Recent prospects, challenges and advancements of photocatalysis as a wastewater treatment method,” 2025, *OAE Publishing Inc.* doi: 10.20517/wecn.2025.03.

[18] N. Khan *et al.*, “Immobilization of TiO2 on Various Substrates,” in *Nanostructured TiO*, wiley, 2025, pp. 87–114. doi: 10.1002/9783527848348.ch05.

[19] A. H. Navidpour, A. Hosseinzadeh, J. L. Zhou, and Z. Huang, “Progress in the application of surface engineering methods in immobilizing TiO2 and ZnO coatings for environmental photocatalysis,” *Catal. Rev. Sci. Eng.*, vol. 65, pp. 822–873, 2023, doi: 10.1080/01614940.2021.1983066.

[20] C. Nguyen Dang Giang, Z. Sebesvari, F. Renaud, I. Rosendahl, Q. Hoang Minh, and W. Amelung, “Occurrence and dissipation of the antibiotics sulfamethoxazole, sulfadiazine, trimethoprim, and enrofloxacin in the Mekong Delta, Vietnam,” *PLoS One*, vol. 10, Jul. 2015, doi: 10.1371/journal.pone.0131855.

[21] G. Braun *et al.*, “Pesticides and antibiotics in permanent rice, alternating rice-shrimp and permanent shrimp systems of the coastal Mekong Delta, Vietnam,” *Environ. Int.*, vol. 127, pp. 442–451, Jun. 2019, doi: 10.1016/j.envint.2019.03.038.

[22] G. H. Ström *et al.*, “Antibiotic Use by Small-Scale Farmers for Freshwater Aquaculture in the Upper Mekong Delta, Vietnam,” *J. Aquat. Anim. Health*, vol. 31, pp. 290–298, Sep. 2019, doi: 10.1002/aah.10084.

[23] J. Antos, M. Piosik, D. Ginter-Kramarczyk, J. Zembrzuska, and I. Kruszelnicka, “Tetracyclines contamination in European aquatic environments: A comprehensive review of occurrence, fate, and removal techniques,” Apr. 2024, *Elsevier Ltd*. doi: 10.1016/j.chemosphere.2024.141519.

[24] D. Tempfli *et al.*, “Revisit of solubility of oxytetracycline polymorphs. An old story in the light of new results,” *European Journal of Pharmaceutical Sciences*, vol. 149, Jun. 2020, doi: 10.1016/j.ejps.2020.105328.

[25] M. S. Bueno *et al.*, “Exploring solid forms of oxytetracycline hydrochloride,” *Int. J. Pharm.*, vol. 585, Jul. 2020, doi: 10.1016/j.ijpharm.2020.119496.

[26] Z. jun LI, W. ning QI, Y. FENG, Y. wang LIU, S. Ebrahim, and J. LONG, “Degradation mechanisms of oxytetracycline in the environment,” Sep. 2019, *Chinese Academy of Agricultural Sciences*. doi: 10.1016/S2095-3119(18)62121-5.

[27] R. A. Sversut, A. A. da Silva, T. F. M. Cardoso, N. M. Kassab, M. S. do Amaral, and H. R. N. Salgado, “A Critical Review of Properties and Analytical Methods for the Determination of Oxytetracyline in Biological and Pharmaceutical Matrices,” Mar. 2017, *Taylor and Francis Ltd.* doi: 10.1080/10408347.2016.1236673.

[28] J. F. Leal, E. B. H. Santos, and V. I. Esteves, “Oxytetracycline in intensive aquaculture: water quality during and after its administration, environmental fate, toxicity and bacterial resistance,” Nov. 2019, *Wiley-Blackwell*. doi: 10.1111/raq.12286.

[29] A. Balapure, J. Ray Dutta, and R. Ganesan, “Recent advances in semiconductor heterojunctions: a detailed review of the fundamentals of photocatalysis, charge transfer mechanism and materials,” Jan. 2024, *Royal Society of Chemistry*. doi: 10.1039/d3lf00126a.

[30] S. J. Armaković, M. M. Savanović, and S. Armaković, “Titanium Dioxide as the Most Used Photocatalyst for Water Purification: An Overview,” Jan. 2023, *MDPI*. doi: 10.3390/catal13010026.

[31] M. A. Hassaan, M. A. El-Nemr, M. R. Elkatory, S. Ragab, V. C. Niculescu, and A. El Nemr, “Principles of Photocatalysts and Their Different Applications: A Review,” Dec. 2023, *Springer Science and Business Media Deutschland GmbH*. doi: 10.1007/s41061-023-00444-7.

[32] K. A. Sanoja-López, N. S. Loor-Molina, and R. Luque, “An overview of photocatalyst eco-design and development for green hydrogen production,” *Catal. Commun.*, vol. 187, Feb. 2024, doi: 10.1016/j.catcom.2024.106859.

[33] Q. Rafiq, S. Azam, S. S. Hayat, U. Javed, A. Mahmood, and S. A. Khan, “Investigating the chemical and physical aspects: optical and electrical properties of TiO2, TiO2: Fe, and Fe/ TiO2 (111) through DFT analysis,” *Chemical Papers*, vol. 78, pp. 283–294, Jan. 2024, doi: 10.1007/s11696-023-03078-7.

[34] B. Dong, T. Liu, C. Li, and F. Zhang, “Species, engineering and characterizations of defects in TiO2-based photocatalyst,” *Chinese Chemical Letters*, vol. 29, pp. 671–680, May 2018, doi: 10.1016/j.cclet.2017.12.002.

[35] M. H. Samat *et al.*, “Exploring changes in structural, electronic and elastic properties of TiO2 under pressure: A DFT investigation,” *Chem. Phys.*, vol. 588, Jan. 2025, doi: 10.1016/j.chemphys.2024.112459.

[36] M. Nasirian, Y. P. Lin, C. F. Bustillo-Lecompte, and M. Mehrvar, “Enhancement of photocatalytic activity of titanium dioxide using non-metal doping methods under visible light: a review,” Sep. 2018, *Center for Environmental and Energy Research and Studies*. doi: 10.1007/s13762-017-1618-2.

[37] R. Rescigno *et al.*, “Photocatalytic activity of P-doped TiO2 photocatalyst,” *Photochemical and Photobiological Sciences*, vol. 22, pp. 1223–1231, Jun. 2023, doi: 10.1007/s43630-023-00363-y.

[38] H. M. Yadav, J. S. Kim, and S. H. Pawar, “Developments in photocatalytic antibacterial activity of nano TiO2: A review,” Jul. 2016, *Springer New York LLC*. doi: 10.1007/s11814-016-0118-2.

[39] “Dye Removal from the Fabric Dyeing Process Wastewater by Municipal Solid Waste Fly Ash blended with Nano-TiO 2,” https://www.researchgate.net/publication/367384356_Dye_Removal_from_the_Fabric_Dyeing_Process_Wastewater_by_Municipal_Solid_Waste_Fly_Ash_blended_with_Nano-TiO_2.

[40] V. Porley and N. Robertson, “Substrate and support materials for photocatalysis,” in *Nanostructured Photocatalysts: From Materials to Applications in Solar Fuels and Environmental Remediation*, Elsevier, 2020, pp. 129–171. doi: 10.1016/B978-0-12-817836-2.00006-5.

[41] A. Alhazaa and N. Haneklaus, “Diffusion bonding and transient liquid phase (TLP) bonding of type 304 and 316 austenitic stainless steel—A review of similar and dissimilar material joints,” May 2020, *MDPI AG*. doi: 10.3390/met10050613.

[42] M. Wongaree, A. Bootwong, S. Choo-in, and S. Sato, “Photocatalytic reactor design and its application in real wastewater treatment using TiO2 coated on the stainless-steel mesh,” *Environmental Science and Pollution Research*, vol. 29, pp. 46293–46305, Jun. 2022, doi: 10.1007/s11356-022-19181-3.

[43] A. Unt, H. Piili, M. Hirvimäki, M. Manninen, and A. Salminen, “Laser scribing of stainless steel with and without work media,” in *29th International Congress on Applications of Lasers and Electro-Optics, ICALEO 2010 - Congress Proceedings*, Laser Institute of America, 2010, pp. 1012–1021. doi: 10.2351/1.5061932.

[44] L. Gardner, A. Insausti, K. T. Ng, and M. Ashraf, “Elevated temperature material properties of stainless steel alloys,” *J. Constr. Steel Res.*, vol. 66, pp. 634–647, May 2010, doi: 10.1016/j.jcsr.2009.12.016.

[45] G. Ureiro-Cueto, S. E. Rodil, J. O. Flores-Flores, L. Hoz-Rodríguez, H. Arzate, and G. Montoya-Ayala, “Assessing the impact of CAP-p15 functionalization on the bioactivity

of rough TiO2-coated 316L stainless steel surfaces," *Biomater. Sci.*, vol. 13, pp. 5122–5133, Sep. 2025, doi: 10.1039/d5bm00294j.

[46] B. L. Pereira *et al.*, "Surface modification of stainless steel via TMS and PEO for biomedical applications," *Surf. Coat. Technol.*, vol. 513, Oct. 2025, doi: 10.1016/j.surfcoat.2025.132533.

[47] J. Liu, S. Rad, J. Dai, L. Gan, and C. Chang, "Review of recent nano TiO2 film coating methods, assessment techniques, and key problems for scaleup," Jan. 2025, *Walter de Gruyter GmbH*. doi: 10.1515/ntrev-2025-0206.

[48] S. W. Kim, Y. long Hou, K. Madhan, K. Senthilkumar, H. S. Kim, and W. J. Kim, "Sol-Gel nano TiO2 synthesis using TTIP: Latest trends, a comprehensive review of attribute optimization and various applications," Sep. 2025, *Elsevier B.V.* doi: 10.1016/j.mattod.2025.05.009.

[49] O. Sadek *et al.*, "Synthesis by sol-gel method and characterization of nano-TiO2 powders," in *Materials Today: Proceedings*, Elsevier Ltd, Jan. 2022, pp. 456–458. doi: 10.1016/j.matpr.2022.06.385.

[50] C. Chang, S. Rad, L. Gan, Z. Li, J. Dai, and A. Shahab, "Review of the sol-gel method in preparing nano TiO2for advanced oxidation process," Jan. 2023, *Walter de Gruyter GmbH*. doi: 10.1515/ntrev-2023-0150.

[51] N. 'Aliaa Razali and S. Amira Othman, "Sol-gel technique in study of titanium dioxide (TiO2) photocatalytic activity- a short review," in *Materials Today: Proceedings*, Elsevier Ltd, Jan. 2022, pp. 4077–4083. doi: 10.1016/j.matpr.2022.07.150.

[52] Z. Abbas *et al.*, "Synthesis, characterization and particle size distribution of TiO2 colloidal nanoparticles," *Colloids Surf. A Physicochem. Eng. Asp.*, vol. 384, pp. 254–261, Jul. 2011, doi: 10.1016/j.colsurfa.2011.03.064.

[53] D. Ma, J. Schneider, W. I. Lee, and J. H. Pan, "Controllable synthesis and self-template phase transition of hydrous TiO2 colloidal spheres for photo/electrochemical applications," Sep. 2021, *Elsevier B.V.* doi: 10.1016/j.cis.2021.102493.

[54] S. Obregón and V. Rodríguez-González, "Photocatalytic TiO2 thin films and coatings prepared by sol–gel processing: a brief review," Apr. 2022, *Springer*. doi: 10.1007/s10971-021-05628-5.

[55] A. Sunil, M. S. Gopika, S. Jayasudha, and P. B. Nair, "Multifunctional applications of TiO2 thin films synthesized by sol–gel dip coating technique," *J. Solgel Sci. Technol.*, vol. 110, pp. 346–362, May 2024, doi: 10.1007/s10971-024-06358-0.

[56] E. Albert *et al.*, "Experimental and Computational Synthesis of TiO2 Sol-Gel Coatings," *Langmuir*, vol. 41, pp. 704–718, Jan. 2025, doi: 10.1021/acs.langmuir.4c03959.

[57] D. Dastan, S. L. Panahi, and N. B. Chaure, "Characterization of titania thin films grown by dip-coating technique," *Journal of Materials Science: Materials in Electronics*, vol. 27, pp. 12291–12296, Dec. 2016, doi: 10.1007/s10854-016-4985-4.

[58] Y. Wang *et al.*, "Investigation on effects of TiO2 on cucumber seedlings using ICP-OES and LA-ICP-MS," *Anal. Chim. Acta*, vol. 1352, May 2025, doi: 10.1016/j.aca.2025.343917.

[59] R. dos Santos *et al.*, "Au-TiO2 Catalysts for Enhanced Visible Light Photocatalysis for Sustainable Treatment of Textile Effluents," *Water Air Soil Pollut.*, vol. 236, May 2025, doi: 10.1007/s11270-025-07920-4.

[60] J. G. Mahy *et al.*, "Advanced photocatalytic oxidation processes for micropollutant elimination from municipal and industrial water," *J. Environ. Manage.*, vol. 250, Nov. 2019, doi: 10.1016/j.jenvman.2019.109561.

[61] D. L. Cunha, A. Kuznetsov, C. A. Achete, A. E. da H. Machado, and M. Marques, "Immobilized TiO2 on glass spheres applied to heterogeneous photocatalysis: Photoactivity, leaching and regeneration process," *PeerJ*, vol. 2018, 2018, doi: 10.7717/peerj.4464.

[62] J. G. Mahy *et al.*, "Easy stabilization of Evonik Aeroxide P25 colloidal suspension by 4-hydroxybenzoic acid functionalization," *Surfaces and Interfaces*, vol. 27, Dec. 2021, doi: 10.1016/j.surfin.2021.101501.

[63] "Process for manufacturing a composite material," 2015

[64] S. Aldwais, A. A. Al-Muntaser, C. Chen, J. Robles, A. Pal, and J. T. Abiade, "Enhancing the Adhesion of Polyaniline on Steel Substrates Without a Binding Agent: Evaluated by ASTM D 3359 Tape Test and Sodium Chloride (NaCl) Exposure," *Polymers (Basel).*, vol. 17, Apr. 2025, doi: 10.3390/polym17081082.

[65] "Cross Hatch Adhesion Tape | ASTM D3359-22 | Elcometer 99," https://www.elcometerusa.com/99-Adhesive-ASTM-Tape-K0001539M001.html.

[66] G. L. M. Léonard *et al.*, "Doped sol-gel films vs. powders TiO2: On the positive effect induced by the presence of a substrate," *J. Environ. Chem. Eng.*, vol. 4, pp. 449–459, Mar. 2016, doi: 10.1016/j.jece.2015.11.040.

[67] M. Iesalnieks, R. Eglītis, T. Juhna, K. Šmits, and A. Šutka, "Photocatalytic Activity of TiO2 Coatings Obtained at Room Temperature on a Polymethyl Methacrylate Substrate," *Int. J. Mol. Sci.*, vol. 23, Nov. 2022, doi: 10.3390/ijms232112936.

[68] T. D. Reynolds, S. K. Kalpathy, S. Kumar, and L. F. Francis, "Dip coating of charged colloidal suspensions onto substrates with patterned wettability: Coating regime maps," *J. Colloid Interface Sci.*, vol. 352, pp. 202–210, Dec. 2010, doi: 10.1016/j.jcis.2010.08.028.

[69] B. Łosiewicz, P. Osak, K. Górka-Kulikowska, and J. Maszybrocka, "Effect of Artificial Saliva Modification on Corrosion Resistance of Metal Oxide Coatings on Co-Cr-Mo Dental Alloy," *Materials*, vol. 17, Nov. 2024, doi: 10.3390/ma17215166.

[70] K. Leelaruedee, P. Visuttipitukul, and N. Yongvanich, "Effect of the added polyethylene glycol molecular weight and calcination heating rate on the morphology of TiO2 films formed by sol-gel," in *Materials Transactions*, Japan Institute of Metals (JIM), 2017, pp. 465–470. doi: 10.2320/matertrans.M2016274.

[71] B. Guo, Z. Liu, L. Hong, and H. Jiang, "Sol gel derived photocatalytic porous TiO2 thin films," *Surf. Coat. Technol.*, vol. 198, pp. 24–29, Aug. 2005, doi: 10.1016/j.surfcoat.2004.10.055.

[72] M. A. Musa, J. M. Juoi, Z. M. Rosli, and N. D. Johari, "Effect of degussa P25 on the morphology, thickness and crystallinity of sol-gel TiO2 coating," in *Solid State Phenomena*, Trans Tech Publications Ltd, 2017, pp. 224–228. doi: 10.4028/www.scientific.net/SSP.268.224.

[73] C. Liu, D. Yang, Y. Jiao, and Y. Tian, "Biomimetic Synthesis of TiO2−SiO2−Ag Nanocomposites with Enhanced Visible-Light Photocatalytic Activity," https://pubs.acs.org/doi/pdf/10.1021/am4004733?ref=article_openPDF.

[74] Y. Chen and D. D. Dionysiou, "Effect of calcination temperature on the photocatalytic activity and adhesion of TiO2 films prepared by the P-25 powder-modified sol-gel method," *J. Mol. Catal. A Chem.*, vol. 244, pp. 73–82, Feb. 2006, doi: 10.1016/j.molcata.2005.08.056.

[75] Y. Zhang *et al.*, "Study on the electrochemical removal mechanism of oxytetracycline by a Ti/IrO2-Ta2O5 plate," *Int. J. Environ. Res. Public Health*, vol. 18, pp. 1–16, Feb. 2021, doi: 10.3390/ijerph18041708.

[76] D. Ivanova, E. Mladenova, and N. Kaneva, "Influence of Non-Ionic Surfactant and Silver on the Photocatalytic Activity of TiO2 Films for Degradation of Dyes in Distilled and Tap Water," *Applied Sciences (Switzerland)*, vol. 14, Jun. 2024, doi: 10.3390/app14114571.

[77] J. Dostanić, B. Grbić, N. Radić, S. Stojadinović, R. Vasilić, and Z. Vuković, "Preparation and photocatalyic properties of TiO 2 -P25 film prepared by spray pyrolysis method," *Appl. Surf. Sci.*, vol. 274, pp. 321–327, Jun. 2013, doi: 10.1016/j.apsusc.2013.03.052.

[78] V. Stankov *et al.*, "Environmental aspects of UV-C-based processes for the treatment of oxytetracycline in water," *Environmental Pollution*, vol. 277, May 2021, doi: 10.1016/j.envpol.2021.116797.

[79] I. Dundar, A. Mere, V. Mikli, M. Krunks, and I. O. Acik, "Thickness effect on photocatalytic activity of tio2 thin films fabricated by ultrasonic spray pyrolysis," *Catalysts*, vol. 10, pp. 1–13, Sep. 2020, doi: 10.3390/catal10091058.

[80] C. Y. Wu, Y. L. Lee, Y. S. Lo, C. J. Lin, and C. H. Wu, "Thickness-dependent photocatalytic performance of nanocrystalline TiO 2 thin films prepared by sol-gel spin coating," *Appl. Surf. Sci.*, vol. 280, pp. 737–744, Sep. 2013, doi: 10.1016/j.apsusc.2013.05.053.

[81] N. R. C. Fernandes MacHado and V. S. Santana, "Influence of thermal treatment on the structure and photocatalytic activity of TiO2 P25," in *Catalysis Today*, Oct. 2005, pp. 595–601. doi: 10.1016/j.cattod.2005.07.022.

[82] P. V. Laxma Reddy, B. Kavitha, P. A. Kumar Reddy, and K. H. Kim, "TiO2-based photocatalytic disinfection of microbes in aqueous media: A review," 2017, *Academic Press Inc.* doi: 10.1016/j.envres.2017.01.018.

[83] E. Bindini, G. Naudin, M. Faustini, D. Grosso, and C. Boissière, "Critical Role of the Atmosphere in Dip-Coating Process," *Journal of Physical Chemistry C*, vol. 121, pp. 14572–14580, Jul. 2017, doi: 10.1021/acs.jpcc.7b02530.

[84] D. M. Tobaldi, R. C. Pullar, M. P. Seabra, and J. A. Labrincha, "Fully quantitative X-ray characterisation of Evonik Aeroxide TiO 2 P25®," *Mater. Lett.*, vol. 122, pp. 345–347, May 2014, doi: 10.1016/j.matlet.2014.02.055.

[85] N. R. C. Fernandes MacHado and V. S. Santana, "Influence of thermal treatment on the structure and photocatalytic activity of TiO2 P25," in *Catalysis Today*, Oct. 2005, pp. 595–601. doi: 10.1016/j.cattod.2005.07.022.

[86] A. Rachel, M. Subrahmanyam, and P. Boule, "Comparison of photocatalytic efficiencies of TiO2 in suspended and immobilised form for the photocatalytic degradation of nitrobenzenesulfonic acids," *Appl. Catal. B*, vol. 37, pp. 301–308, Jul. 2002, doi: 10.1016/S0926-3373(02)00007-3.

[87] X. Cheng, R. Guan, Y. Chen, Y. Qian, Q. Shang, and Y. Sun, "Adsorption and photocatalytic degradation process of oxytetracycline using mesoporous Fe-TiO2 based on high-resolution mass spectrometry," *Chemical Engineering Journal*, vol. 460, Mar. 2023, doi: 10.1016/j.cej.2023.141618.

5 Appendices

5.1 Procedure of tape test in lab

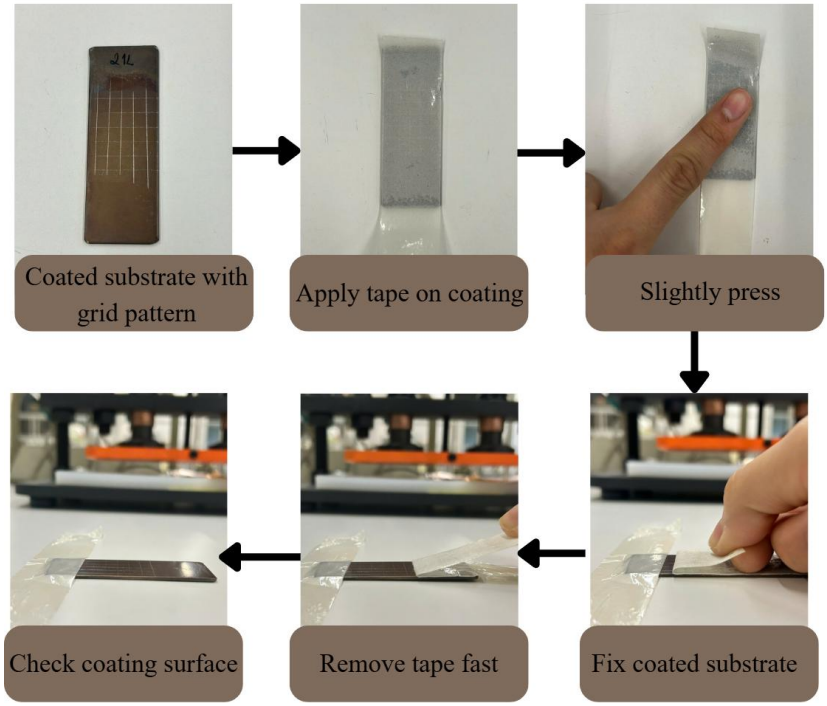

Figure 66. Lab procedure of tape test

5.2 XRD pattern

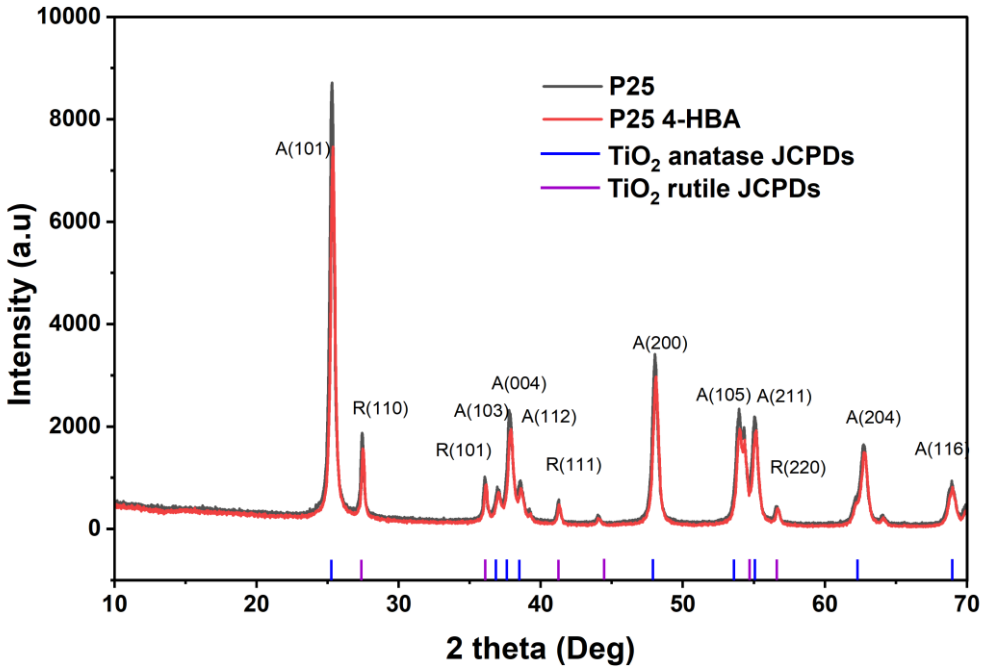

Figure 67. XRD patterns of P25 powder and functionalized P25 powder

The Figure 67 shows the post-functionalization structural integrity, the XRD profile for the functionalized sample (P25 4-HBA, red line) perfectly overlaps with that of the pristine P25 (black line), showing no changes in diffraction peak positions or line width, but with a small decrease in intensities. This excellent alignment demonstrates that the functionalization of P25 with 4-HBA did not distort the underlying crystal lattice or alter the native anatase-to-rutile phase ratio. Consequently, these findings indicate that the modification is restricted purely to a surface-level interaction or chemical grafting, successfully preserving both the bulk crystallinity and the structural integrity of the original photocatalyst.

5.3 Effects of substrate surface nature on sol-gel based coating mass

Table 39. The sol-gel based coating mass on Al substrate

1 layer of sol-gel-based coating on Al substrate		
Repeated	**Before coating (g)**	**After coating (g)**
1	3.75130	3.75226
2	3.75130	3.75224
3	3.75128	3.75223
4	3.75135	3.75224
5	3.75131	3.75226
Average	3.751308	3.752246
Coating mass (mg)	**0.938**	

Table 40. The sol-gel based coating mass on glass substrate

1 layer of sol-gel-based coating on glass substrate		
Repeated	**Before coating (g)**	**After coating (g)**
1	5.16971	5.17049
2	5.16983	5.17043
3	5.16975	5.17042
4	5.16977	5.1704
5	5.16982	5.17042
Average	5.169776	5.170432
Coating mass (mg)	**0.656**	

Table 39 and Table 40 indicate that the deposition behaviour of sol-gel-based coatings is strongly influenced by the surface roughness of the substrate. The coating mass deposited on the aluminium substrate was approximately 0.938 mg, whereas only 0.656 mg was deposited on the glass substrate. This difference suggests that rougher surfaces provide more anchoring sites and surface irregularities that can retain a larger amount of sol-gel material during the dip-coating process.

The observed trend can be attributed to the relatively high viscosity of the sol-gel solution. During coating deposition, the viscous sol-gel is more easily trapped within the microscopic valleys and asperities of a rough surface, resulting in a higher coating mass. In contrast,

smoother substrates such as glass offer fewer surface features for mechanical retention, leading to a lower amount of deposited material.

These findings highlight the importance of substrate surface characteristics when applying sol-gel coatings. For applications requiring higher coating loading or thicker films, moderate surface roughening may be beneficial, as it can enhance coating retention and improve the amount of photocatalyst immobilized on the substrate. However, excessive roughness should be carefully controlled, as it may lead to non-uniform coating thickness, localized stress concentrations, and an increased risk of coating cracking during drying and calcination.

5.4 EDX Mapping

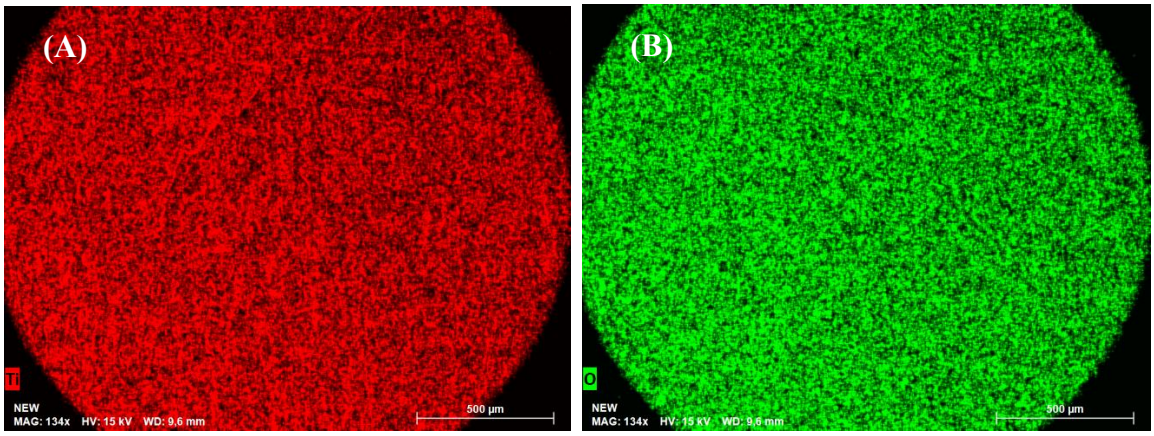

Figure 68. EDX mapping of Ti and O elements

The Figure 68 illustrates the elemental distribution maps (EDX mapping) obtained from the sample surface. The mapping results confirm the distinct presence of two primary elements: Titanium (Ti), represented in red, Figure 68 (A), and Oxygen (O), represented in green, Figure 68 (B). Both Ti and O elements exhibit a highly homogeneous and fine distribution across the entire analysed area. The spatial correlation and overlapping density between the Ti and O signals strongly indicate the uniform formation of titanium oxide throughout the material matrix. This visual evidence successfully corroborates the quantitative EDX spectrum data, confirming that the fabrication process achieved optimal phase dispersion and chemical homogeneity at the microstructure scale.